Resolving Ganglioside Heterogeneity within Murine *Staphylococcus aureus* Abscesses using MALDI TIMS IMS

By

Katerina Vassileva Djambazova

Dissertation

Submitted to the Faculty of the

Graduate School of Vanderbilt University

in partial fulfillment of the requirements for

the degree of

DOCTOR OF PHILOSOPHY

in

Chemistry

August 12th, 2022

Nashville, Tennessee

Approved:

Richard M. Caprioli, Ph.D.

Jeffrey M. Spraggins, Ph.D.

Kevin L. Schey, Ph.D.

Renã A. S. Robinson, Ph.D.

John A. McLean, Ph.D.

ACKNOWLEDGEMENTS

I am incredibly grateful to the many people who have helped me and guided me along this journey. First and foremost, I would like to thank my mentors, Dr. Richard Caprioli and Dr. Jeff Spraggins. Richard, you have pushed me to work hard and with intention. I'm grateful to have worked under your guidance and to have been a part of you research laboratory. Jeff, thank you for your incredible mentorship. You lead by example with kindness and compassion – I am very fortunate to have you in my corner. To my entire committee, Dr. Kevin Schey, Dr. John McLean, and Dr. Renã Robinson, I am thankful for your continuous support.

To my fellow Caprioli Lab members – Josiah, Emilio, Emma, Kavya, and Chris, thank you for your friendship and for making graduate school so memorable. I will always treasure our impromptu Trivia Nights, Happy Hours, Costco hotdog trips, and endless conversations about absurd "what if" hypotheticals. Emma, thank you for being a kind and warm-hearted friend, for watching hours of terrible TV with me, and for waiting in line to get coffee at 4 am. Emilio, I am so incredibly grateful for our friendship. Thank you for your limitless generosity, loyalty, and empathy. Thank you for our tradition of afternoon Sodies, and for making sure I never get lost in the tunnels. Chris, you are a gem, and I am so happy to have gotten to know you over the last couple of years. Jackie and Ally, you joined the Spraggins Lab when I was in the thick of writing my dissertation and your contagious scientific curiosity and positivity often brightened my days. To our postdocs, both past and present – Dustin, Jarod, Martin, Angela, and Maddie, thank you for your sharing your scientific expertise, providing mentorship, and offering words of encouragement. Amanda and Angie, thank you for taking care of us all - we would be lost without you! To all members of the Mass Spectrometry Research Center and the Van de Plas Lab, thank you for embracing me as part of your team(s) and for years of fruitful collaborations.

Lastly, thank you to my friends and family – your love and support are my constant motivators. Words cannot express my gratitude to my parents, thank you for always believing in me and being by my side, even when you are an ocean away. Alex, thank you for sharing your love of science with me and persuading me to give Chemistry a shot in college. Thank you for guiding me, being an incredible role model and an even better friend. Pragun, you are my rock. You are patient, loving, and understanding; I am beyond lucky to have you in my life.

TABLE OF CONTENTS

LIST OF FIGURES

LIST OF TABLES

ABBREVIATIONS

$1/K_0$: Reduced Mobility
9-AA: 9-Aminoacrinine
ACA: 4-Acinaminic Acid
AmF: Ammonium Formate
AmS: Ammonium Sulfate
AUC: Area Under the Curve
BMP: Bis(monoacylglycerol)phosphate
CCS: Collision Cross Section
Cer: Ceramide
CFU: Colony Forming Units
CID: Collision Induced Dissociation
CMBT: 5-Chloro-2-mercaptobenzothiazole
Cy5: Cyanine 5
Da: Daltons
DAN: 1,5-Diaminonapthalene
DAPI: 4',6-Diamino-2-phenylindole
DESI: Desorption Electrospray Ionization
DHA: 2,5-Dihydroxyacetophenone
DHB: 2,5-Dihydroxybenzoic Acid
DMF: Dimethylformamide
dpi: days post infection
DTIMS: Drift Tube Ion Mobility
E: trans
EFG: Electric Field Gradient
EGFP: Enhanced Green Fluorescent Protein
ESI: Electrospray Ionization
FAIMS: Field Asymmetric Ion Mobility Spectrometry
FT-ICR: Fourier Transform Ion Cyclotron Resonance
Gal: Galactose
GalNAc: N-Acetylgalactosamine
GD: Disialylated Ganglioside
GM: Monosialylated Ganglioside
GQ: Quatrasialylated Ganglioside
GT: Trisialylated Ganglioside
Glc: Glucose
H&E: Hematoxylin and Eosin
HexCer: Hexosylceramide
HPLC: High Performance Liquid Chromatography
IHC: Immunohistochemistry
IF: Immunofluorescence
IMS: Imaging Mass Spectrometry
ITO: Indium Tin Oxide
LC: Liquid Chromatography
M: Monoisotopic Peak
m_{gas}: Mass of the Gas (in kg)
m_{ion}: Mass of an Ion
m_{FWHM}: Full Width at Half Maximum (Mass Spectrometry)
MALDI: Matrix-Assisted Laser Desorption Ionization
m/z: Mass-to-Charge Ratio
MS: Mass Spectrometry
MS/MS (MS^n): Tandem Mass Spectrometry
Nd: YAG: Neodymium-doped Yttrium Aluminum Garnet
Neu5Ac: N-acetylneuraminic acid
Neu5Gc: N-glycolylneuraminic acid
OCT: Optimal Cutting Temperature
p: Pressure
PBS: Phosphate Buffered Saline
PC: Phosphatidylcholine
PE: Phosphatidylethanolamine
PG: Phosphatidylglycerols
PI: Phosphatidylinositol
ppm: part per million
PS: Phosphatidylserine
r: Resolution
R: Resolving Power
RF: Radio Frequency
ROI: Region of Interest
SAC: Staphylococcal Abscess Community
S. aureus: Staphylococcus aureus
SEM: Scanning Electron Microscopy
SIMS: Secondary Ionization Mass Spectrometry
SLIM: Structures for Lossless Ion Manipulation
SM: Sphingomyelin
S_r: Scan Rate
S/N: Signal-to-Noise Ratio
t: Temperature

THF: Tetrahydrofuran
TIMS: Trapped Ion Mobility
timsTOF: Trapped Ion Mobility Time of Flight
TOF: Time of Flight
t_{ramp}: Ramp Time (ms)
TWIMS: Travelling Wave Ion Mobility
V_{ramp}: Ramp Voltage Change
w: Full Width at Half Maximum (Ion Mobility)
Z: cis

CHAPTER I

INTRODUCTION: MOLECULAR IMAGING WITH MALDI TRAPPED ION MOBILITY TIME OF FLIGHT MASS SPECTROMETRY

This chapter was in part adapted from *Multimodal Imaging Mass Spectrometry for Thoroughly Probing the Chemistry within Biological System*, *High Performance Molecular Imaging with MALDI Trapped Ion Mobility Time-of-Flight (timsTOF) Mass Spectrometry*[1] and *Integrating Ion mobility and Imaging Mass Spectrometry for Comprehensive Analysis of Biological Tissue: A Brief Review and Perspective*[2] with permissions from the publishers and co-authors.

OVERVIEW

Biological imaging of intact tissue sections can reveal the spatial relationships of molecules in their native environement.[3] Such analyses are essential for providing new insight into the numerous biological processes in healthy and diseased samples, demonstrating their worth in clinical and hospital settings. Imaging mass spectrometry (IMS) can achieve this by combining the molecular sensitivity and specificity of mass spectrometry (MS) with tissue sampling technologies that enable rapid, high spatial resolution data acquisition.[4–6] IMS enables untargeted analysis and visualization biomolecules within biological systems, providing ion maps that are easily correlated to tissue histology for a diverse array of biological specimens. IMS has been used to investigate diverse chemical classes ranging from small metabolites[7], lipids[8], and drugs[9] to peptides[10], glycans[11,12], and proteins[13]. In a typical IMS experiment, ions are generated at discrete locations (pixels) across a defined tissue region. Each pixel is composed of an individual mass spectrum, where molecular images can be generated for each mass-to-charge ratio (*m/z*) by plotting the ion intensity of that signal throughout the entire array of pixels of the imaged sample.[14] While there are numerous IMS technologies reported in literature, the three most common include matrix-assisted laser desorption/ionization (MALDI)[15], secondary ion mass spectrometry (SIMS)[16,17], and desorption electrospray ionization (DESI).[18,19]

Matrix-assisted Laser Desorption/Ionization Imaging Mass Spectrometry (MALDI IMS)

MALDI is a common "soft" ionization technique for direct tissue analysis used to visualize molecular species ranging from small metabolites to intact proteins.[20] The first step of MALDI IMS, as highlighted in **Figure 1.1A**, typically involves sectioning tissues into thin sections and thaw-mounting them onto a conductive glass slide.[3] An organic chemical compound (matrix) is subsequently applied to the tissue to co-crystalize with the analytes, aiding in their desorption and ionization in the MALDI process. Common matrices include 2,5-dihydroxybenzoic acid (DHB)[21] - for positive-ion mode analysis of metabolites, lipids, and peptides; 9-aminoacridine (9-AA)[22] - for negative-ion mode analysis of metabolites, lipids, and proteins; and 1,5-diaminonaphthalene (DAN)[23] - for analysis of lipids in both ion polarities (**Figure 1.1B**). Matrix deposition is often performed robotically to best achieve reproducibility, analyte extraction, small crystal size, and coating homogeneity. Alternatively, sublimation, sieving, and airbrushing are also used in the field.[6,19]

Once the sample is loaded into the mass spectrometer, ions are generated by laser ablation at each pixel.[6] Most modern MALDI IMS platforms utilize either a frequency-tripled Neodymium-doped Yttrium Aluminum Garnet laser (Nd:YAG, 355 nm) or nitrogen gas laser (337.7 nm). Both

can achieve spatial resolutions of 5 – 20 µm using traditional front-side laser optics.[24–26] In a MALDI IMS experiment, spatial resolution is defined by the ablation area of the laser and the distance between pixels known as "pitch" or "step size" (**Figure 1.1C**). Modern commercially available lasers may also include internal galvo mirrors that enable beam steering (or scanning) during acquisition. Instead of a circular footprint, approximated "square pixels" can be obtained by rastering the laser to ablate material closer to the entire pixel area maximizing the sampled area during an imaging experiment. As demonstrated by Spraggins et. al.[1], square pixels increased the number of sampled molecules by ~27% for a 10 × 10 µm target pixel dimension resulting in improved sensitivity. Efficient sampling is of particular importance for high-spatial-resolution experiments, because as pixels become smaller, the number of molecules sampled decreases, and the measurement approaches the limit of detection of the instrument.[27] Ultimately, spatial

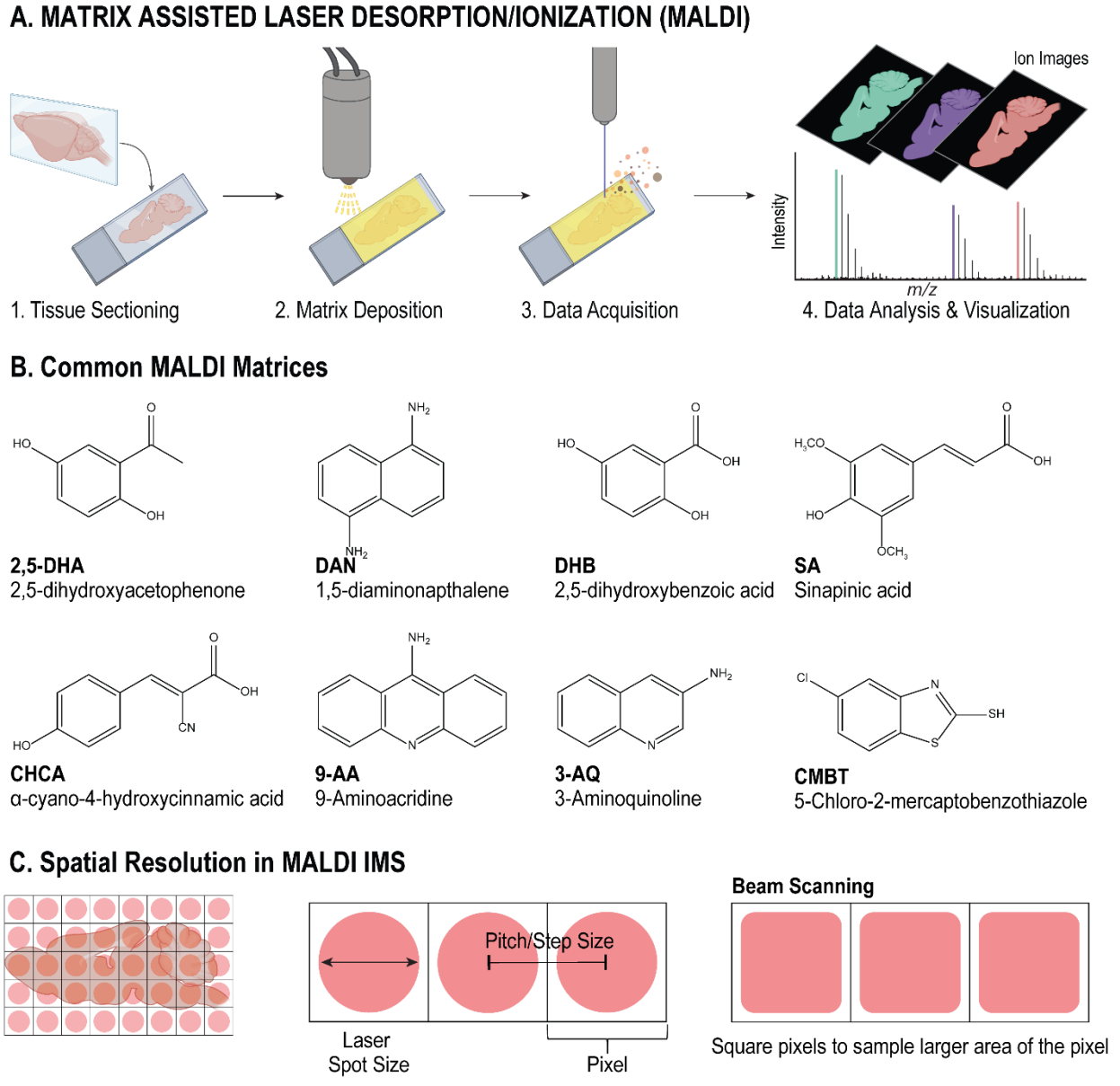

Figure 1.1. Overview of the MALDI workflow including tissue sectioning, matrix deposition, data acquisition, as well as data analysis and visualization (**A**); Common MALDI matrices and their chemical structures **(B)**; Considerations for determining spatial resolution in MALDI imaging **(C)**.

resolution is dependent upon multiple factors such as matrix crystal size, laser focus, and stage motor step precision.[26,28]

Mass Analyzers

After ions are generated, ion optics guide them through the mass spectrometer to the mass analyzer, and subsequently to the detector.[29] Mass analyzers separate ions based on their mass-to-charge ratios (*m/z*). Although there are many different mass analyzers, based on application needs, all analyzers should ideally be able to distinguish minute mass differences while allowing for the passage of sufficient number of ions to be readily detected. Figures of merit for mass analyzer performance include mass accuracy and resolving power, as described in **Figure 1.2**, and **Equations (1) & (2)**.

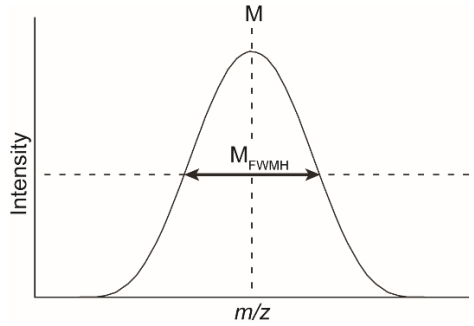

Figure 1.2. Figures of Merit for MS Analyzers

(1) Mass Accuracy

$$\frac{|M_{exp} - M_{theo}|}{M_{theo}} \times 10^6 \text{ ppm}$$

M_{exp} – experimental mass
M_{theo} – theoretical mass

(2) Resolving Power (R)

$$R = \frac{M}{M_{FWHM}}$$

M – observed mass
M_{FWHM} – peak width at half maximum

Time-of-Flight (TOF) analyzers are most commonly used for MALDI IMS experiments.[19] TOF analyzers separate ions based on differences in ion velocity in a high-vacuum flight tube.[29] In linear TOF analyzers, ions entering the drift tube are accelerated with the same kinetic energy where lighter ions of the same charge will travel faster than heavier ones. Thus, lighter ions reach the detector faster. As ions vary in their initial position and velocity, there is a significant spread of signal in arrival times at the detector. To minimize spread and thus increase resolution and sensitivity, ion introduction can be delayed – termed delayed extraction[30]; alternatively, reflectron TOF analyzers can be utilized. Such analyzers increase the sensitivity and mass resolution by lengthening the analyte ion path and by reducing the kinetic energy spread by ions with the same *m/z*.[31]

TOF platforms are simplistic and offer analysis over a wide mass range, however they have limited mass accuracy and resolving power.[5,19] By contrast, Fourier Transform ion cyclotron resonance (FT-ICR) cell analyzers have demonstrated unsurpassed resolving power.[32] In FT-ICR platforms, generated ions are transmitted to an ICR cell that is enclosed in a magnet. The cell is composed of three distinct sets of plates – trapping, transmitter, and receiving plates.[32] In the cell, ions move in circular orbits held in place by electric potential applied to the trapping plates, which is perpendicular to the magnetic field. A sequence of RF pulses is applied and the ions are thus excited to larger orbits. As ions pass by the receiver plates, the frequency of their passage is detected as an induced "image" current. The frequency is inversely proportional to the *m/z* of an ion, which can be obtained by a Fourier transformation. This type of ion detection is non-destructive allowing for longer storage and repeated cycles of ion detection resulting in high resolving powers. Thus, FT-ICR platforms are ideal for separating ions with similar *m/z* values

such as closely isobaric species. However, two ions with the same exact *m/z* (isomers) cannot be resolved by the mass analyzer alone regardless of its resolving power.[32] In such cases, tandem MS (MS/MS, MS^n) can be used to fragment ions, where the resulting spectra can provide unique profiles of product ions aiding in their identification.[33]Alternatively, separation techniques, such as liquid chromatography (LC) and ion mobility, can be integrated to resolve and detect isomeric species having the same *m/z* value.[34,35]

Ion Mobility Mass Spectrometry

Imaging mass spectrometry can be coupled to a variety of analytical approaches to enhance the gained information and probe the molecular complexity of biological systems in a single mass spectrometric experiment.[2,36] Ion mobility enables gas-phase separation of ions according to their shape, size, and charge on a millisecond timescale before their detection in the mass spectrometer.[37–41] Separation is achieved by introducing analytes to an electric field that provides space separation.[40] Each ion is affected differently, where molecular size-to-charge ratio determines their mobility (*K*) in the system, causing ions to exit from the ion mobility cell at differing times.[38,40] Ions mobility is defined as the ratio of ion-gas relative velocity (v_d) to the electric field (*E*) (**Equation 3**). Reduced ion mobility (K_0) is commonly used as it incorporates a correction factor for pressure (p) and temperature (T) (**Equation 4**).[40] However, it is customary to report an ion's $1/K_0$ value instead, as it is proportional to its three-dimensional surface area, known as its collision cross section (CCS).[40] The CCS values can be derived from the Mason-Schamp Equation (**Equation 5**).[38]

(3) Ion Mobility (*K*)

$$K = \frac{v_d}{E}$$

Relative velocity (v_d)
Electric Field (E)

(4) Reduced ion mobility (K_0)

$$K_0 = K \times \frac{N}{N_0}$$

Number of gas molecules per unit volume (N): $N = \frac{p}{T}$

Loschmidt's number (N_0): $N_0 = \frac{p_0}{k_B T_0}$

(5) Collision Cross Section (CCS)

$$CCS = \frac{3}{16} \times \sqrt{\frac{2\pi}{\mu k_B T}} \times \frac{q}{N_0 K_0}$$

Reduced mass (μ): $\mu = \left(\frac{1}{m_{ion}} + \frac{1}{m_{gas}}\right)^{-1}$

Boltzmann constant (k_B): $1.38 \times 10^{-23}\ m^2\ kgs^{-2}\ K^{-1}$

Ion mobility separation techniques include drift tube ion mobility spectrometry (DTIMS)[42,43], traveling wave ion mobility spectrometry (TWIMS)[38,44], field asymmetric ion mobility spectrometry (FAIMS)[45–47], and trapped ion mobility spectrometry (TIMS)[48–50].[38] Figures of merit for ion mobility experiments include ion mobility resolving power (R) and resolution (r) calculated using **Equation (6)** and **(7)**, respectively.[40,51]

(6) Resolving power (R)

$$R = \frac{{}^{1}/_{K_0}}{w}$$

$1/K_0$ = inverse reduced mobility
w = peak width at half-maximum

(7) Resolution (r)

$$r = 1.18 \times \frac{\left({}^{1}/_{K_0}\right)_2 - \left({}^{1}/_{K_0}\right)_1}{w_1 + w_2}$$

DTIMS is the simplest ion mobility system, in which ions traverse through a drift tube directed by a uniform electric field in the presence of inert gas molecules.[37] In TWIMS, ions are directed through the device by symmetric potential waves. The ions are radially confined using radio-frequency (RF) voltage on adjacent stacked-ring electrodes and a direct current (DC) voltage is applied to create a "travelling wave".[44] Structures for lossless ion manipulation (SLIM) devices also operate under TWIMS principles, however, they incorporate long serpentine paths to enhance ion mobility resolving power.[52,53] FAIMS uses an alternating electric field, applied perpendicular to the ion path, such that the ions experience both high and low field environments.[38,45] Lastly, TIMS is the most recently developed ion mobility technology in which ion are trapped, separated and released from the TIMS device by a gradually reduced electric field gradient.[54] All of the highlighted ion mobility techniques, with the exception of SLIM, have been previously coupled with imaging platforms to improve the performance of biological tissue imaging.[2,36]

Trapped Ion Mobility Spectrometry (TIMS)

TIMS is a high resolving power ion mobility technology introduced by Fernandez-Lima and coworkers in 2011.[48,55] TIMS separations are carried out in the first vacuum stage of a mass spectrometer in an augmented ion funnel. It is composed of an entrance funnel, TIMS tunnel, and an exit funnel.[49] Propelled by a carrier gas, ions are accumulated and trapped, and separated by an electric field. To elute trapped ions, the electric field gradient (EFG) is gradually reduced, releasing ions with ascending mobilities. The voltage range (ΔV_{ramp}) and ramp time (t_{ramp}) dictate the scan rate (S_r) as shown in **Equation (8)**.[55] Scan rates dictate the separation resolution, with slower scan rates resulting in higher resolutions. To date, TIMS platforms are capable of resolving powers of > 200 in 50-500 ms.[49,50]

(8) Scan rate (Sr)

$$S_r = \frac{\Delta V_{ramp}}{t_{ramp}}$$

t_{ramp} = ramp time
ΔV_{ramp} = voltage range

In 2019 Spraggins and coworkers developed a prototype MALDI TIMS imaging platform from an electrospray ionization (ESI) timsTOF Pro instrument as depicted in **Figure 1.3**.[1] With

respect to the original ESI-based instrument, the source housing was modified to accommodate a MALDI stage, a sample loading chamber, and laser optics. It was designed to load and unload a MALDI sample carrier through a vacuum isolated lock chamber similar to other MALDI platforms. The MALDI source uses a Bruker SmartBeam 3-D laser system consisting of a frequency-tripled solid-state Nd:YAG laser (wavelength: 355 nm) with repetition rates ≤ 10 kHz and internal galvo mirrors that enable beam steering during acquisition.[1] The beam exits the laser as parallel light and is focused by an aspherical lens stack before it enters the vacuum chamber through a window. Inside the vacuum chamber, a single flat mirror directs the beam to the sample surface for ion generation. Initial MALDI TIMS IMS experiments by Spraggins et. al (2019)[1] demonstrated high spatial resolution (10 µm) imaging and proof-of-concept for *in situ* TIMS separations. This initial MALDI TIMS IMS study showed great promise for enhanced specificity in molecular imaging applications, particularly for metabolite and lipid analysis, where mass redundancy and structural isomers are prevalent.[1,2]

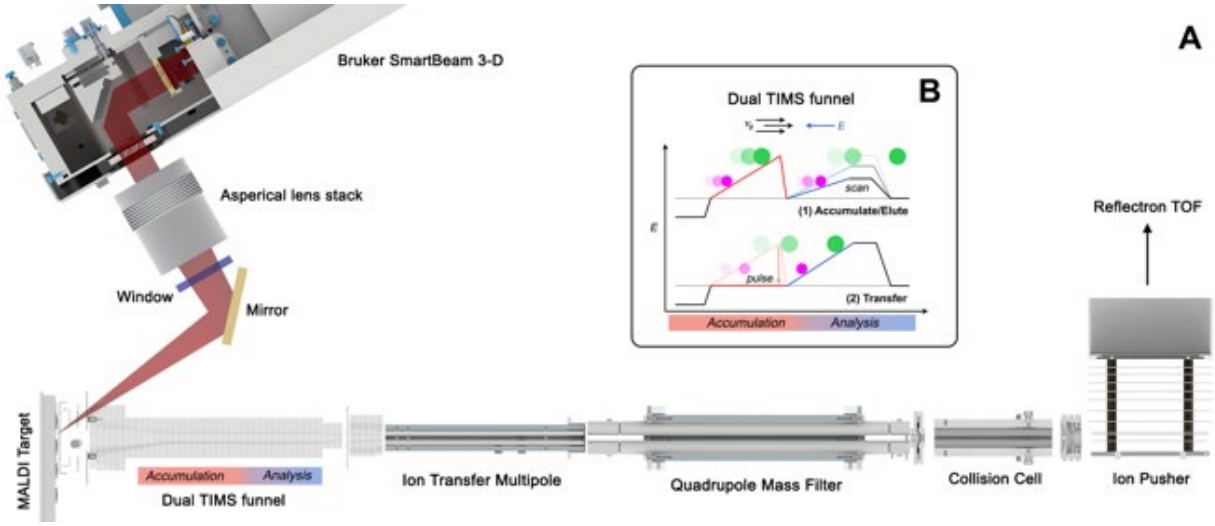

Figure 1.3. Prototype MALDI timsTOF mass spectrometer. **(A)** The developed imaging platform couples a MALDI source capable of high-spatial-resolution and throughput imaging with an ESI timsTOF Pro mass spectrometer. **(B)** Ion-mobility separations are performed in a dual TIMS funnel in the first vacuum stage of the instrument. TIMS resolution is tunable by adjusting the electric field gradient scan time and throughput is maximized by performing accumulation and analysis in parallel on sequential pixels. Reprinted with permission from Spraggins et. al., *Analytical Chemistry* (2019). Copyright 2019 © American Chemical Society.

Lipids and Spatial Lipidomics

Lipids are essential components of the cell membrane with functions in cellular structure, signaling, and energy storage.[56–58] Lipid profiles are known to vary throughout tissues and as a function of disease progression.[59] Visualizing alterations in lipid compositions/distributions can provide insight into different biological systems. MALDI IMS can retain analyte spatial information, however, the structural diversity of lipids within biological systems can often be underrepresented.[60,61] The high abundance and structural diversity of lipids results in many isobaric and isomeric structures, which poses a challenge for their analysis, as even subtle structural differences can have significant biological implications.[62] Developing more comprehensive ways of *in situ* lipid characterization is essential for elucidating biological roles. [63]

The structural features of a glycerophospholipid molecule, where a phosphatidylcholine (PC) is used as an example, are highlighted in **Figure 1.4**. The PC headgroup highlighted in yellow is attached to the *sn*-3 position of the glycerol backbone (blue).[58,62] Fatty acyls of varying carbon lengths (12 – 22) and double bonds (0 – 6) are attached to the glycerol backbone at the *sn*-1 and *sn*-2 positions. Numerous isomers are possible in these structures, including *sn*-positional isomers – differing in the position of the fatty acyls along the glycerol backbone (*sn*-1 vs *sn*-2); double-bond positional isomers differing in the position of a double bond along the fatty acid chain, and double bond stereochemistry isomers - differing in the cis/trans orientation of the double bond.[64] Isomers have identical *m/z* values, therefore direct MS analysis cannot be used to distinguished the structures.[65] In an imaging context, ion images of single *m/z* values may depict composites of multiple lipid species leading to misrepresentation of spatial distributions.[66]

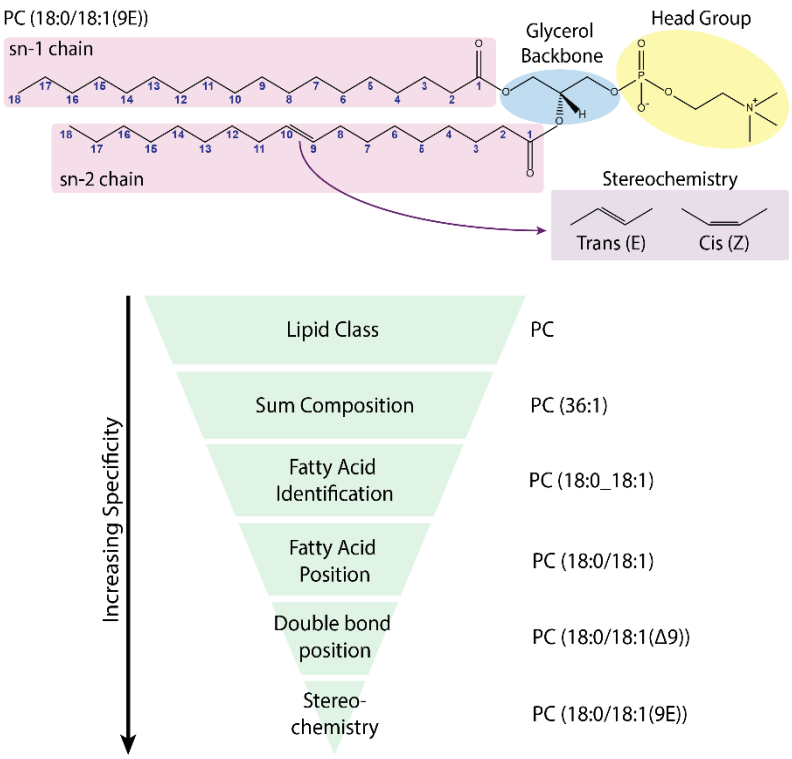

Figure 1.4. Lipid Structural diversity highlighted with an example of PC (18:0/18:1(9E))

To aid in structural analysis, tandem MS has been used to reveal distributions of isomeric lipids *in situ*. Novel MS^n techniques, including low-energy collision-induced dissociation (CID)[66] with Paternò–Büchi derivatization[67], ozone-induced dissociation[68], and ultraviolet photodissociation[69], have revealed differential localization of double-bond positional and *sn* positional isomers. While MS^n techniques provide a higher degree of structural characterization, they are highly targeted and often require additional derivatization steps. Integration of an online chromatographic separation with direct tissue sampling can increase the specificity of an IMS experiment, however, this setup typically requires lengthy acquisition times.

Ion mobility has also been crucial for structural analysis of lipids, particularly in resolving overlapping lipid signals in complex biological mixtures.[39,70] Mobility trendlines generated during DTIMS and TWIMS separations have been beneficial for identifying classes and subclasses of lipids and have also enabled increases in signal-to-noise (S/N) ratios.[43,71] DTIMS and TWIMS have both been used to separate ESI-generated lipid isomers, including *sn* positional, double-bond positional, and stereochemical isomers (R versus S).[72] Both techniques have previously been utilized on instruments capable of imaging mass spectrometry. However, higher ion mobility resolving power necessary to address isomeric signal *in situ* can diminish throughput significantly. MALDI TIMS IMS shows great promise for high throughput and resolving power separations of isomeric lipids in high spatial resolution tissue imaging applications.

Gangliosides

Gangliosides are acidic glycosphingolipids, highly abundant in the mammalian nervous system.[73–75] They are critical components of neuronal and glial cells and play an essential role in neuronal development and maturation. Although gangliosides are well studied in the context of neurological diseases, they are also involved in immune system regulation.[76,77] They have been linked to infectious diseases, including *Staphylococcus aureus* (*S. aureus*), however their functions in the immune system are not well understood.[78]

Gangliosides consist of a hydrophobic ceramide lipid backbone and an oligosaccharide chain with one or multiple sialic acid residues.[79,80] They share the same ceramide and saccharide "building blocks" leading to a highly diverse class of molecules **(Figure 1.5)**.[81,82] This structural heterogeneity also results in a high number of biologically relevant isomers and presents a challenge for their comprehensive analysis.[79] MS has been a critical tool for the detection and characterization of gangliosides, where soft ionization techniques, such as ESI and MALDI have been preferred to avoid extensive precursor ion fragmentation.[83] MALDI IMS has previously been employed to map ganglioside distributions within biological tissues, including murine and human central nervous system tissues.[84–86]

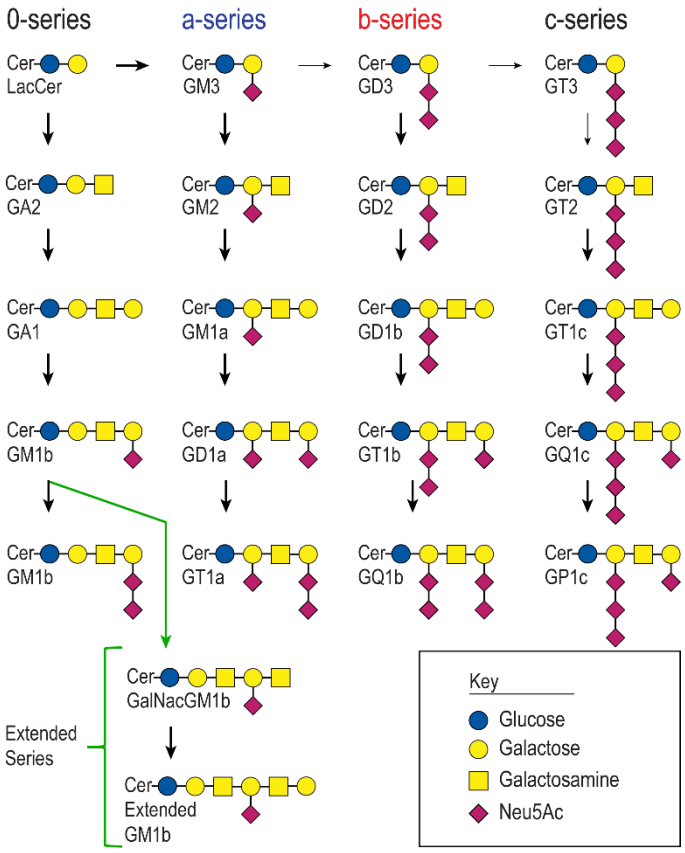

Figure 1.5. Ganglioside synthesis pathway highlighting major key gangliosides found in mammalian cells, including extended series gangliosides known to be involved in the immune system.

Detailed structural characterization of ganglioside isomers is important in an imaging context, as isomeric gangliosides are typically synthesized by different pathways, and therefore have different distributions, biological roles, and are differentially impacted by disease.[87–90] A notable example are the a- and b-series disialogangliosides (GD1a and GD1b), which differ in the position of a single sialic acid, where GD1a has a sialic acid on the internal and terminal galactose units whereas GD1b has both sialic acid units in a chain attached to the internal galactose unit.[80] These two gangliosides make up over 80% of the entire mammalian ganglioside content, have different spatial distributions, and are affected differently by neurological diseases, Alzheimer's disease.[90–92] Being able to separate the two gangliosides would increase the specificity of the analysis and is essential for linking structure and function. Significant strides in ganglioside isomer separation have recently been made by Ekroos and coworkers, who recently demonstrated the separation of GD1a(d36:1) and GD1b(d36:1) in mouse hemi-brain extracts using a prototype SLIM-MS instrument.[93] Furthermore, Jackson *et. al*. demonstrated the combination of ion mobility

and MALDI for the analysis of GD1a and GD1b, where they show higher drift times for the GD1a isomer.[94] However, the spatial distributions of ganglioside isomers have not been directly demonstrated in a MALDI imaging context thus far.

Gangliosides and *Staphylococcus aureus*

Staphylococcus aureus (S. aureus) is a widespread commensal bacterium and pathogen. It is among the most prominent causes of bacterial infections, resulting in high rates of pathogen-associated morbidity and mortality in the US.[95] In addition to its high prevalence, *S. aureus* is known for acquiring antibiotic resistance, which poses a challenge for current treatment strategies.[96]

A hallmark of *S. aureus* infections is the formation of soft tissue abscesses.[97] Past studies of the staphylococcal abscess architecture and its cellular contributors led to the development of a robust model of abscess formation shown in **Figure 1.6.**[97,98] Infiltrating bacteria organize into staphylococcal abscess communities (SAC) and recruited immune cells eventually form a lesion around the pathogen. The lesion is primarily a mixture of degenerate and viable innate immune, separated from the healthy host tissue via a fibrous capsule. The lesion grows with the recruitment of immune cells, and the healthy host tissue is destroyed through neutrophil necrosis. The mature abscess is a highly heterogeneous environment with a diverse subset of host- and pathogen-derived molecules. A lot remains unclear about the molecular makeup of the abscess, so spatially aware strategies that probe this environment can be useful for untangling its molecular complexity. Furthermore, understanding the molecular changes that occur during the infection process can help guide future treatments.

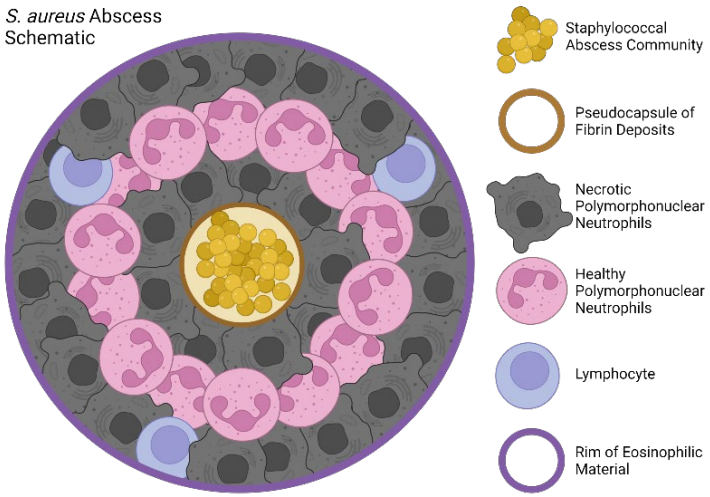

Figure 1.6. Working schematic of a mature staphylococcal abscess in host tissue showing a central accumulation of the bacteria into staphylococcal abscess communities (SAC) surrounded by a pseudocapsule of fibrin deposits, followed by zones of necrotic and healthy neutrophils (gray and purple cells), and a rim of eosinic

Gangliosides aid in immune system modulation in both innate and acquired immunity – processes that are not completely understood. The high degree of structural heterogeneity results in significant variability in their expression patterns and complicates linking structure and function. Structural characterization at the site of infection is essential in elucidating host ganglioside function in response to invading pathogens such as *Staphylococcus aureus* (*S. aureus*). MALDI TIMS IMS shows great promise for in-depth structural investigation of the molecular heterogeneity in the infection lesion. Here, we aim to investigate the complexity of ganglioside heterogeneity and isomerism at the host-pathogen interface of an *S. aureus* abscess using MALDI TIMS IMS.

SUMMARY AND RESEARCH OBJECTIVES

MALDI IMS allows for untargeted spatial investigation of complex biological systems such as tissue sections. Confident lipid identification and data interpretation are challenging due to the high degree of mass redundancy, owing to the presence of isobaric and isomeric species. Separation techniques, such as ion mobility spectrometry, can be integrated in MALDI IMS workflows to help deconvolute the complexity of spatial lipidomics. The recently developed MALDI timsTOF prototype instrument incorporates a high throughput, high spatial resolution MALDI source with a TIMS separation dimension. The increase of specificity in a MALDI experiment, provided by the TIMS dimension was quantified for the lipidomic range. For this purpose, peak capacity, the ability of the system to resolve common mass spectral ambiguities *in situ* was determined. A threefold increase in detected species was observed when incorporating the TIMS separation dimension. Common mass spectral ambiguities, such as the double-bond ambiguity, were readily resolved in an imaging MS experiment. Following this analysis, a systematic analysis of common isomeric lipids standards, including *sn*-backbone isomers, acyl chain isomers, and double-bond position and stereoisomers was demonstrated. As a proof of concept, *in situ* separation and imaging of lipid isomers with distinct spatial distributions were performed using tissue sections from a whole-body mouse pup. These data provide the foundation for maximizing the sensitivity and specificity of lipid imaging experiments on TIMS-based MALDI platforms.

The *m/z* range was expanded to include high-mass analytes such as gangliosides. In-tact ganglioside analysis is challenging due to their high structural diversity as well as their predisposition to significant in-source fragmentation. Here, sample preparation strategies were optimized for *in situ* MALDI IMS of ganglioside species. Furthermore, we demonstrate the use of MALDI TIMS IMS to distinguish GD1a and GD1b using a 1:1 mixture, a total porcine brain ganglioside extract, and directly within thin tissue sections. With this, the unique spatial distributions of GD1a/b(d36:1) and GD1a/b(d38:1) isomers were revealed in both rat brain and spinal cord samples at 20 µm spatial resolution.

The developed methods provided enhanced specificity of ganglioside analysis, necessary to evaluate the structural complexity of ganglioside species within an *S. aureus* abscessed region. The structural diversity of ganglioside species, present in the host-pathogen interface, were characterized in terms of glycan headgroup, ceramide, and sialic acid diversity. Isomeric gangliosides, including a- and o- series GM1 (both Neu5Ac and Neu5Gc) species were detected. Spatial investigation revealed new molecular signatures that were not revealed by traditional microscopy. Lastly, spatial investigation of molecular distributions within infected tissues over 4, 6, and 10 days post infection (dpi) revealed alteration in relative GM1b/GM1a isomer abundances throughout the course of the infection. Through these studies MALDI TIMS IMS is shown to be an optimal technology for providing thorough characterization of complex lipid structures within infected tissues.

CHAPTER II

INCREASING THE SPECIFICITY OF SPATIAL LIPIDOMICS WITH MALDI TIMS IMS

This chapter was in part adapted from *High Performance Molecular Imaging with MALDI Trapped Ion Mobility Time-of-Flight (timsTOF) Mass Spectrometry*[1] and *Resolving the Complexity of Spatial Lipidomics Using MALDI TIMS Imaging Mass Spectrometry*[99] with permissions from the publishers and co-authors.

OVERVIEW

MALDI IMS allows for direct mapping of biomolecules in tissues. Fully characterizing the structural diversity of lipids remains a challenge due to the presence of isobaric and isomeric species, which greatly complicates data interpretation when only *m/z* information is available. Integrating ion mobility separations aids in deconvoluting these complex mixtures and addressing the challenges of lipid IMS. Here, we demonstrate that a MALDI quadrupole TOF mass spectrometer with TIMS enables a > 250% increase in peak capacity during IMS experiments. MALDI TIMS IMS separation of common isobaric interferences, including the double bond ambiguity, was demonstrated. Lipid isomer standards, including *sn* backbone isomers, acyl chain isomers, double-bond positional isomers, and stereoisomers, were also analyzed. Finally, the utility of MALDI TIMS IMS for lipidomic analysis was shown by *in situ* separation and imaging of lipid isomers with distinct spatial distributions in tissue sections from a whole-body mouse pup.

INTRODUCTION

Lipids are crucial components of cellular membranes with essential functions in cellular structure, signaling, energy storage, and homeostasis.[56,100] They are structurally diverse molecules, with many having the same nominal mass and some having the same exact mass.[56] Developing more comprehensive ways of characterizing these complex mixtures in tissues is important, as even subtle structural differences can have significant biological implications. Mass spectrometry is a powerful tool for lipid analysis with common *ex vivo* approaches utilizing electrospray ionization and either direct infusion of lipid extracts or separations via liquid chromatography, neither of which retains the spatial information of analytes in tissues. In contrast, MALDI IMS, which analyzes biomolecules *in situ*, enables highly specific mass analysis while retaining analyte spatial information.[101]

The structural diversity of lipids in tissues can often be under-represented during MALDI IMS experiments owing to the presence of isobars and isomers that cannot be distinguished by their measured *m/z* alone.[59] High resolving power and high mass accuracy instrumentation, including FT-ICR and Orbitrap mass analyzers, have been critical in enabling both lipid identification at the sum composition level, as defined by Liebisch et al.[100], and isobar differentiation. However, structural isomers with identical masses cannot be separated by high mass resolving power instruments. In these cases, ion images of single *m/z* values may depict composites of multiple lipid species having the same *m/z* value. More advanced techniques, such as tandem MS (MS^s), can be used to reveal distributions of isomeric lipids *in situ*.[33] More specifically, techniques including low-energy collision-induced dissociation with Paternò–Büchi

derivatization, ozone-induced dissociation, and ultraviolet photodissociation have revealed differential localization of double-bond positional and *sn* positional isomers.[102,103] While MS^n techniques provide a higher degree of structural characterization, they are highly targeted and may provide a very narrow analytical window.[104]

Ion mobility enables gas-phase separation of molecules according to their shape, size, and charge on timescales that are compatible with typical IMS experiments.[2,36] DTIMS and TWIMS have been used to separate ESI-generated lipid isomers, including *sn* positional, double-bond positional, and stereochemical isomers.[72] The ability of TIMS to resolve isomeric lipids via liquid chromatography-TIMS-MS suggests that it has the capability to resolve isomeric lipids *in situ*.[105] Integrating TIMS with IMS has shown resolving powers > 200 in 50 – 500 ms, which has great potential for high-resolution separations. While a MALDI TIMS-MS platform has successfully been used to separate and spatially map lipid species that overlap in the *m/z* space[1,106], a full assessment of the effect of TIMS on peak capacity and isomer separation in an imaging context has not been demonstrated yet.

Here, we present the use of TIMS technology for increasing peak capacity and deconvolution of complex lipid mixtures in an imaging context. The high-resolution separation of the MALDI-generated lipid isomer standards is demonstrated followed by an *in situ* assessment of lipid peak capacity using TIMS IMS and visualization of the lipid isomers in a full-body mouse pup tissue. These data provide the foundation for maximizing the sensitivity and specificity of lipid imaging experiments on TIMS-based MALDI platforms.

RESULTS AND DISCUSSION

Enhancing Peak Capacity with TIMS

Direct sampling of lipids from tissues by IMS produces complex mass spectra. To assess the advantage of incorporating TIMS into an IMS workflow, spectral peak capacity (i.e., the number of detected features) was determined for an average spectrum of a whole-body mouse pup tissue image. Peak capacity is determined by peak picking the data to identify the number of unique mass spectral features with and without incorporating TIMS data. When the TIMS dimension is incorporated, the peak capacity is determined as the number of unique mass spectral and associated mobility features. For the mouse pup dataset, the average mass spectrum from *m/z* 680 to 880 with no ion mobility separation has a peak capacity of 247. Over the same *m/z* range, with a 650 ms TIMS separation, the peak capacity increased to 916. In this example, integrating ion mobility into the MALDI IMS workflow provided a threefold increase in the number of detected features. The increased peak capacity afforded by TIMS results from the separation of isobaric and isomeric species that otherwise overlap in the *m/z* dimension. Specific examples of such interferences are highlighted in the following sections.

Resolving Isobaric Interferences *in situ*

Unresolved lipid isotopic overlaps can lead to artificially high mass errors that preclude identification.[107,108] Ion mobility allows for gas-phase separations that help address this spectral complexity. To evaluate the utility of MALDI TIMS for resolving isobaric signals in the *m/z* dimensions, whole-body mouse pup sections were analyzed.

A well-documented example of isobaric interference that occurs with lipid analysis is the "double-bond ambiguity".[108] It arises from the overlap of an M+2 isotopologue of one species with the monoisotopic (M) peak of another lipid of the same class with one fewer double-bonds giving rise to a mass difference of 0.00895 Da. While TOF instruments generally are not able to resolve the double-bond ambiguity, the added dimension of ion mobility allows for gas-phase separations of overlapping isotopes. An *in situ* example of phenomenon can be seen for ion with *m/z* 848.55 (**Figure 2.1**). With a TIMS ramp time of 650 ms, the ion of *m/z* 848.55 resolved into two mobility peaks: $1/K_0$ 1.475 and $1/K_0$ 1.492. **Figure 2.1A** shows the composite ion image combining the mobility-separated species for *m/z* 848.55, where **Figure 2.1B and C** show the individual ion images for $1/K_0$ 1.475 and $1/K_0$ 1.492, respectively, each of which localizes to distinct regions of the tissue. For example, $1/K_0$ 1.492 is found at higher abundance in the brain and with more distinct localization to the intestinal walls as compared to $1/K_0$ 1.475, which shows unique localization in the adipose tissue. **Figure 2.1D** shows the ion image of *m/z* 846.54 for the ion with $1/K_0$ 1.475, which, by comparison, localizes to the same regions of tissues as *m/z* 848.55 with $1/K_0$ 1.492.

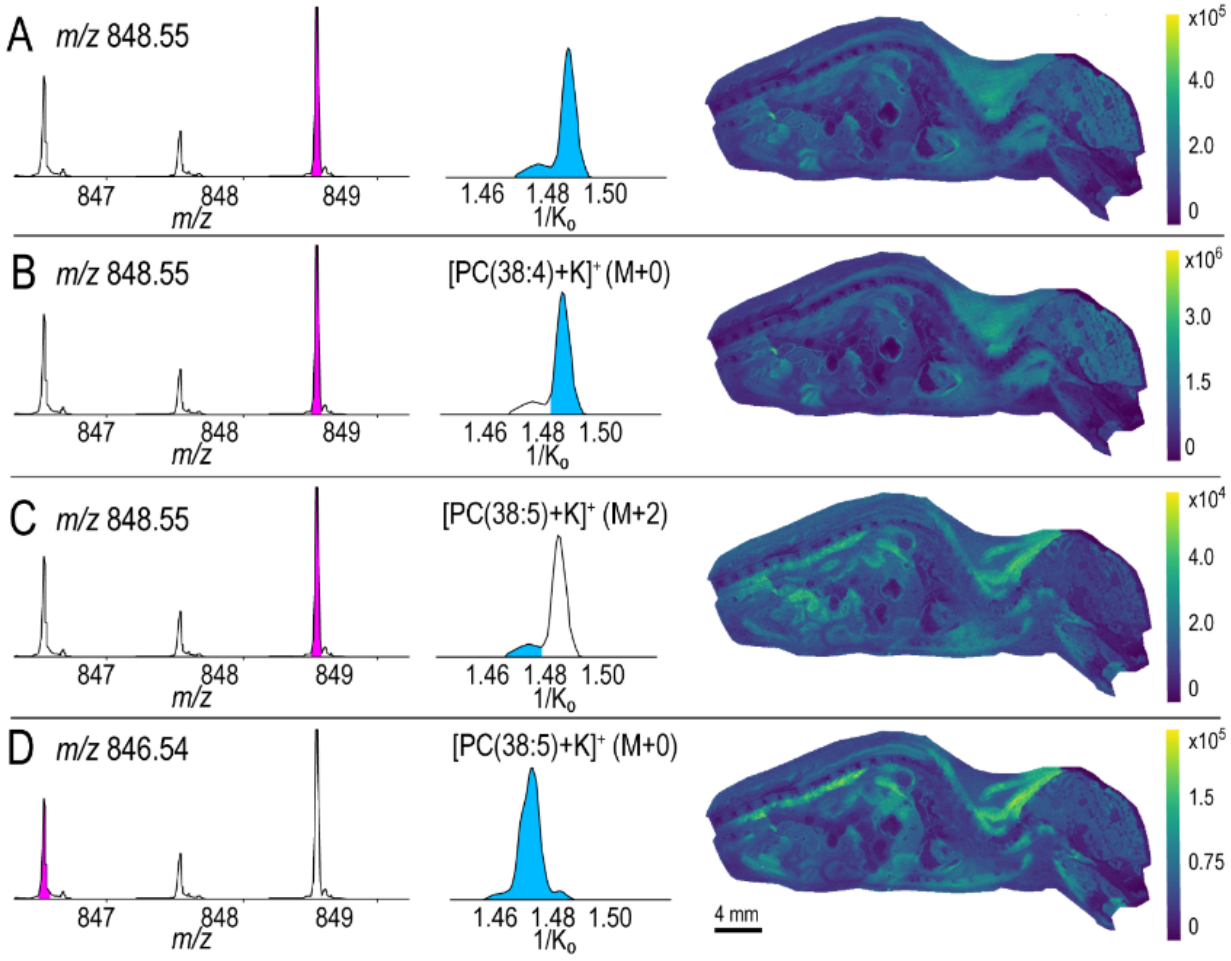

Figure 2.1. MALDI TIMS resolved the double-bond ambiguity for *m/z* 848.55 in a whole-body mouse pup tissue section. The extracted ion mobilogram of *m/z* 848.55 showed two peaks - $1/K_0$ 1.492 and $1/K_0$ 1.477 **(A)**. Composite image of the two ions **(A)** and individual ion images for $1/K_0$ 1.492 **(B)** and $1/K_0$ 1.477 **(C)** highlight differences in their spatial distributions. The ion image of *m/z* 846.54 + $1/K_0$ 1.477 **(D)** localizes to the same regions as *m/z* 868.55 for the same mobility range **(C)**. Species *m/z* 848.55 + $1/K_0$ 1.492 likely corresponds to the monoisotopic peak of $[PC(38:4) + K]^+$, while *m/z* 848.55 + $1/K_0$ 1.477 corresponds to the M + 2 peak of $[PC(38:5) + K]^+$. Reprinted with permission from Djambazova et. al., Analytical Chemistry (2020) Copyright 2020 © American Chemical Society.

Considering the intact mass measurements and differences in spatial localizations, the species at *m/z* 848.55 with a $1/K_0$ 1.492 likely corresponds to the monoisotopic peak of $[PC(38:4) + K]^+$, while the species of *m/z* 848.55 with $1/K_0$ 1.475 corresponds to the M + 2 peak of $[PC(38:5) + K]^+$. Without a mobility separation, *m/z* 848.55 would be assigned solely as the higher intensity $[PC(38:4) + K]^+$ and the generated ion image would provide a skewed representation of its distribution throughout the tissue.

Another mass spectral ambiguity, resulting in a 0.0025 Da mass difference, arises from the overlap of sodiated and protonated ions of the same lipid class, where the protonated ion has two additional carbons and three additional double bonds in the fatty acyl chain.[108] A prime example for this was observed at *m/z* 756.55 (**Figure 2.2A**). The extracted ion mobilogram of that *m/z*-value resolved individual ions with $1/K_0$ 1.465 and $1/K_0$ 1.505, (**Figure 2.2A**). Here, the ion image was dominated by the more abundant species ($1/K_0$ 1.505). However, the two species displayed drastically different spatial distributions across the imaged sample. The lower mobility ion ($1/K_0$ 1.465) identified as $[PC(34:3)+H]^+$, was detected throughout the animal but had a lower abundance within the brain and brain stem (**Figure 2.2B**). Conversely, the higher mobility isobar, identified as $[PC(32:0)+Na]^+$, was primarily found within the brain, spine, and intestines (**Figure 2.2C**). Identification of these species was done by FT-ICR MS/MS, as described in the methods section (**Appendix 6.1.1. & 6.1.2**).

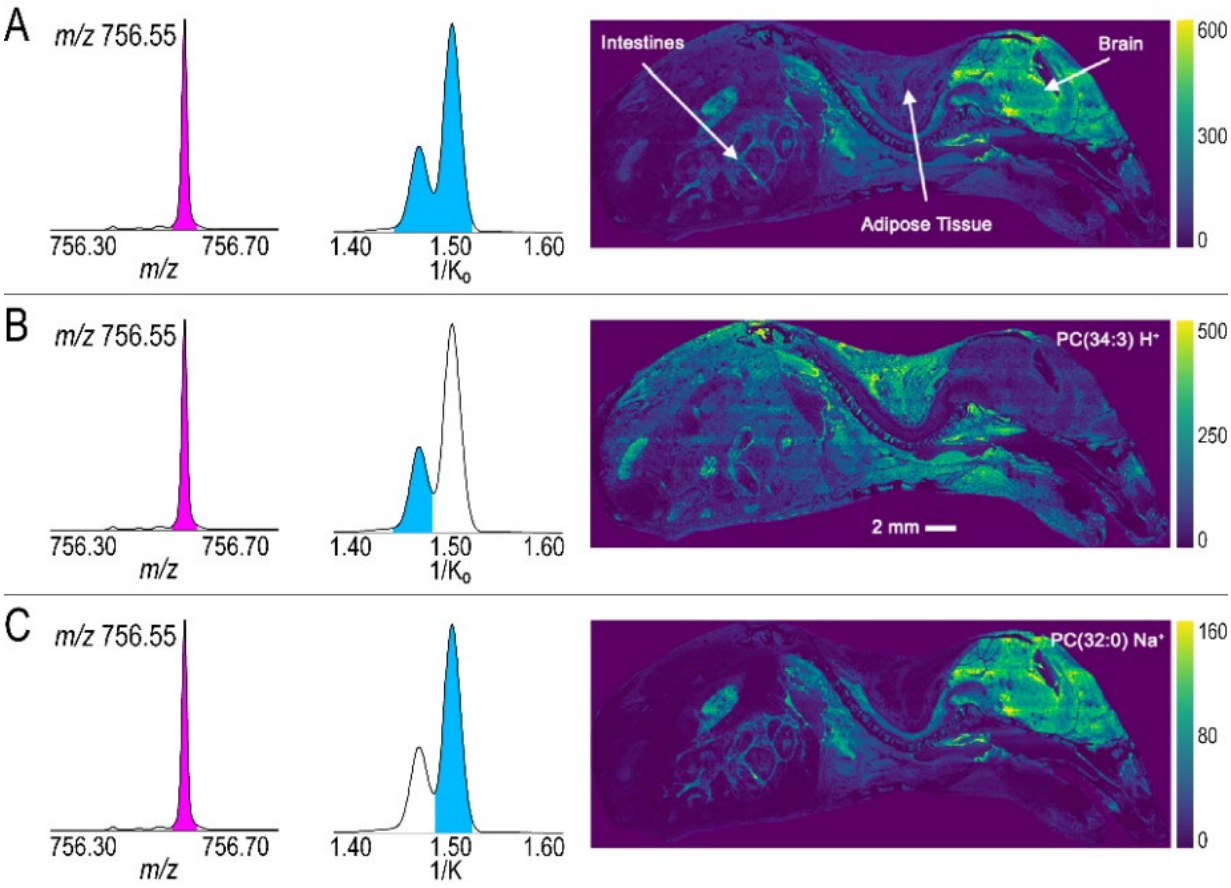

Figure 2.2. MALDI TIMS IMS can resolve ions with a 2.5 mDa mass difference *in situ* , as demonstrated in the extracted ion mobilogram of *m/z* 756.55 **(A)**. $[PC(34:3) + H]^+$ is found throughout the tissue except the brain and spinal cord. **(B);** $[PC(32:0) + Na]^+$ localizes to the brain, spine, and intestines **(C)**. Adapted with permission from Spraggins et. al., Analytical Chemistry (2019) Copyright 2019 © American Chemical Society.

These examples highlight the power of ion mobility separations in improving specificity and molecular coverage in direct tissue analysis. Resolving the aforementioned differences in mass (0.00895 Da and 0.0025 Da) requires resolving powers >300,000 at *m/z* 760, which can only be performed on FT-ICR/Orbitrap mass spectrometers. Resolution of this magnitude is challenging to achieve and requires long scan times (~1.5–3 s). For example, an FT-ICR IMS experiment would require over 200 hours to achieve baseline resolution of these two isobars at the same spatial resolution as acquired on the TIMS imaging experiment here. By contrast, MALDI TIMS IMS can separate the isobars while maintaining < 2 pixels/s throughput. Furthermore, differentiating various ionizing adducts (e.g., H^+ , Na^+ , and K^+) is important for imaging experiments, as they are regularly generated by MALDI tissue analysis and cannot be removed without additional sample preparation.[6] Unless MS/MS is performed, differences in the distributions of these species typically go unnoticed, potentially reducing the quality or accuracy of resulting IMS information.

Systematic Analysis of MALDI-Generated Lipid Isomer Standards

Isomers have the same chemical formulas (identical *m/z* values) and therefore cannot be separated in *m/z* space alone. Gas-phase separations prior to MS detection have been successful in resolving isomeric species.[109,110] Here, MALDI TIMS isomer separations were evaluated in both positive- and negative-ion mode. The instrumental performance was assessed using standards including isomers with differences in *sn*-position, acyl chain composition, double-bond position, and double-bond stereochemistry (**Figure 2.3**). These standards have previously been characterized using ESI techniques in combination with TIMS, as well as other separation techniques.[109,111] MALDI TIMS analyses, however, lay the groundwork for isomer differentiation within a molecular imaging context. Extracted ion mobilograms were generated for each standard as well as for the mixtures of isomeric standards. Both ion mobility resolving power (R) and resolution (r) (**Equations (6) & (7), Chapter I**), were calculated.

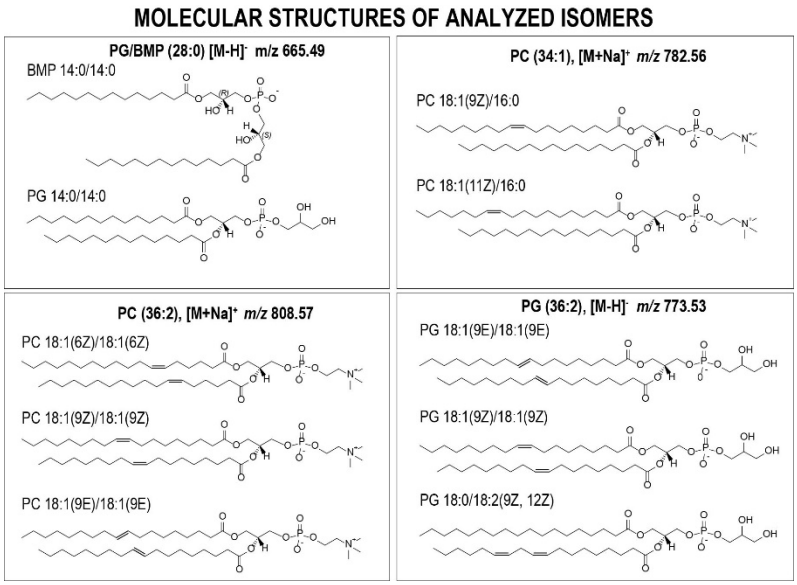

Figure 2.3. Molecular structures of *sn*-position, double-bond position, and double-bond stereochemistry isomers standards, analyzed in this chapter.

sn-Position

Subtle differences in glycerophospholipid structure, including differences in acyl chain positions, can have dramatic effects on biological functions. A unique case of the *sn* positional isomers is Bis(monoacylglycerol)phosphates (BMPs) and phosphatidylglycerols (PGs) are a unique case of *sn* positional isomers. In contrast to PGs, where both acyl chains are connected to the glycerol backbone, BMPs have one acyl chain connected at the *sn*-1 position on the glycerol

backbone, and a second acyl chain connected to the *sn*-1′position of the glycerol headgroup, resulting in an unusual *sn*-1:*sn*-1′orientation.[109,110] Differentiation of BMPs and PGs is important, as both are present in mammalian cells, but differ in their biological roles and cell locations.[112] BMP lipids have been found in the endosomal and lysosomal compartments of the cell and have been associated with Niemann−Pick disease, an endosomal/lysosomal storage disease.[112,113] PGs, on the other hand, are thought to have antiviral properties, inhibiting viral proliferation in the lungs including respiratory syncytial virus.[110,114]

Characterizing *sn*-positional isomers is particularly challenging as collision-based tandem mass spectrometry methods produce spectra with differences only in ion abundances, i.e., only non-unique identifying ions are produced.[110] To evaluate the utility of MALDI TIMS as a platform to separate PG and BMP isomers, mobility data were collected for the PG (14:0/14:0) and BMP (14:0/14:0) standards (**Figure 2.4A**). Compounds were first analyzed individually to determine mobility values. The MS1 spectrum for each standard contains a predominant ion of *m/z* 665.49 corresponding to the $[M-H]^-$ species for each lipid. The measured $1/K_0$ values were 1.268 and 1.283 for PG(14:0/14:0) and BMP (14:0/14:0), respectively. The difference in backbone orientation results in an increased distance between the acyl chains and consequently, an increased difference in collision cross section between BMP and PG.[109] A 1:1 mixture was then analyzed to evaluate the separation of the isomers. An extracted ion mobilogram was generated for the deprotonated species (*m/z* 665.49), and the two peaks could be resolved in the mobilogram (1.270 and 1.282). The mobilogram of the mixture showed separation of the two species with a resolution of 0.84. Based on the $1/K_0$ values, our results indicate that the PG has a more compact structure than the BMP, which is consistent with previous studies. [109,110]

Acyl Chain Composition, Double-Bond Position, and Double-Bond Stereochemistry

The biophysical effects of acyl chain compositions and the positions and stereochemistry (cis (Z) vs trans (E)) of double bonds in lipid acyl chains are well-documented.[64,115] The thickness and fluidity of biological membranes are affected by lipid double-bond stereochemistry, as well as acyl chain length.[109,116] Specifically, shorter acyl chains and cis double bonds result in thinner, more fluidic membranes.[117] Lipids with trans double bonds are known to cause changes in membrane function and inhibition of lipid enzymatic pathways.[116] Differences in double-bond position, on the other hand, have been linked to the development of various diseases, including cancer and type-2 diabetes[103], and have been known to influence lipid-protein binding[118]. To assess the separation capabilities of MALDI TIMS for such isomers in both negative and positive ionization mode, lipids with differences in acyl chain composition, double-bond position, double-bond stereochemistry, and combinations of composition, position, and stereochemistry were examined.

First, MALDI TIMS was performed in negative ionization mode for the deprotonated ions of PG (18:1(9E)/18:1(9E)) and PG (18:0/18:2(9Z,12Z)) standards (**Figure 2.4B**). Both lipids have two unsaturations: PG (18:0/18:2(9Z,12Z)) has two double bonds on the same acyl chain in cis stereochemistry and PG (18:1/18:1(9E)) has a single unsaturation on each chain with trans stereochemistry (these lipid standards differ in acyl chain composition, double-bond position, and double-bond stereochemistry). The mass spectrum of each standard was dominated by the $[M-H]^-$ ion at *m/z* 773.53. The measured $1/K_0$ values for PG (18:1(9E)/18:1(9E)) and PG (18:0/18:2-(9Z,12Z)) were 1.394 and 1.383, respectively. The lower $1/K_0$ value for PG (18:0/18:2(9Z,12Z)) suggests that it assumes a more compact gas-phase structure. A mixture of the two standards shows

partial separation (r 1.0) suggesting that the isomers with differences in acyl chain composition, double-bond position, and stereochemistry could be resolved *in situ*. To further test the separation capabilities for more subtle differences in structures, mobility data were collected for PG (18:1(9E)/18:1(9E)) and PG (18:1(9Z)/18:1(9Z)) standards, which only differ in double-bond stereochemistry. Extracted ion mobilograms of the deprotonated species (*m/z* 773.53) are shown in **Figure 2.4C**. The measured $1/K_0$ values for individual PG (18:1(9Z)/18:1(9Z)) and PG (18:1(9E)/18:1(9E)) were 1.381 and 1.394, respectively. The mixture of PG (18:1(9Z)/18:1(9Z)) and PG (18:1(9E)/18:1(9E)) confirms that the deprotonated species of each lipid can be well resolved (r 1.1). Based on the lower mobility value, PG (18:1(9Z)/18:1(9Z)) takes on a more compact gas-phase structure than PG (18:1(9E)/18:1(9E)). Our results from both isomer pairs suggest that the lipids with cis double bonds have more compact structures than lipids with trans double bonds. These findings are aligned with the existing literature, as cis double bonds are believed to introduce a bend or curl in otherwise linear acyl chains.[109]

MALDI TIMS separations of double-bond position and stereoisomers were also evaluated for cationic lipids. Positive ionization mode analysis was carried out on sodium-adducted PC standards. **Figure 2.4D** shows the extracted ion mobilograms of the $[M + Na]^+$ ion (*m/z* 808.57) for PC (18:1(6Z)/18:1(6Z)) and PC (18:1(9E)/18:1(9E)) that vary in both double-bond position and stereochemistry. The individual mobilograms of the sodiated species show that PC (18:1(9E)/18:1(9E)) ($1/K_0$ 1.462) has a lower mobility value than PC (18:1(6Z)/18:1(6Z)) ($1/K_0$ 1.468). The two standards are not well resolved from a mixture of the standards (r 0.52). Our results suggest that the 9E isomer results in a more compact structure than the 6Z, which is consistent with previously published data, suggesting that the trans orientation is more impacted by the sodium adduct, pulling it closer to the headgroup, resulting in a more compact conformation than the 6Z.[109] To investigate the effect of double-bond position alone, standard PC (18:1(6Z)/18:1(6Z)) was analyzed with PC (18:1(9Z)/18:1(9Z)) in a 1:1 mixture (**Figure 2.4E**). The individual extracted ion mobilograms (*m/z* 808.57) show that the 9Z isomer results in a smaller structure than the 6Z, with $1/K_0$ 1.458 and 1.468, respectively. The mobilograms of the mixture show separation of the two species with a resolution of 1.01. Our results indicate that the 9Z isomer results in a more compact structure. This finding is also supported by previous literature, stating that cis double bonds further from the carboxyl end curl the acyl chain more, causing smaller conformations.[109]

Finally, mobility separations were performed on isomers that vary only in the position of a single double bond using PC (18:1(9Z)/16:0) and PC (18:1(11Z)/16:0) standards (*m/z* 782.56, $[M+Na]^+$, **Figure 2.4F**). These lipid species are generally abundant in biological tissues and represent an interesting biological target. For instance, Paine et al. have demonstrated that although both PC (18:1(9Z)/16:0) and PC(18:1(11Z)/16:0) are found in the rat brain tissue, their relative abundances vary between white matter and gray matter.[63] The individual mobilograms suggest that the 11Z isomer has a more compact structure ($1/K_0$ 1.430) than the 9Z isomer ($1/K_0$ 1.436). Despite the difference in a single double-bond location being very subtle, slight separation in the mobilogram was still observed (r 0.59).

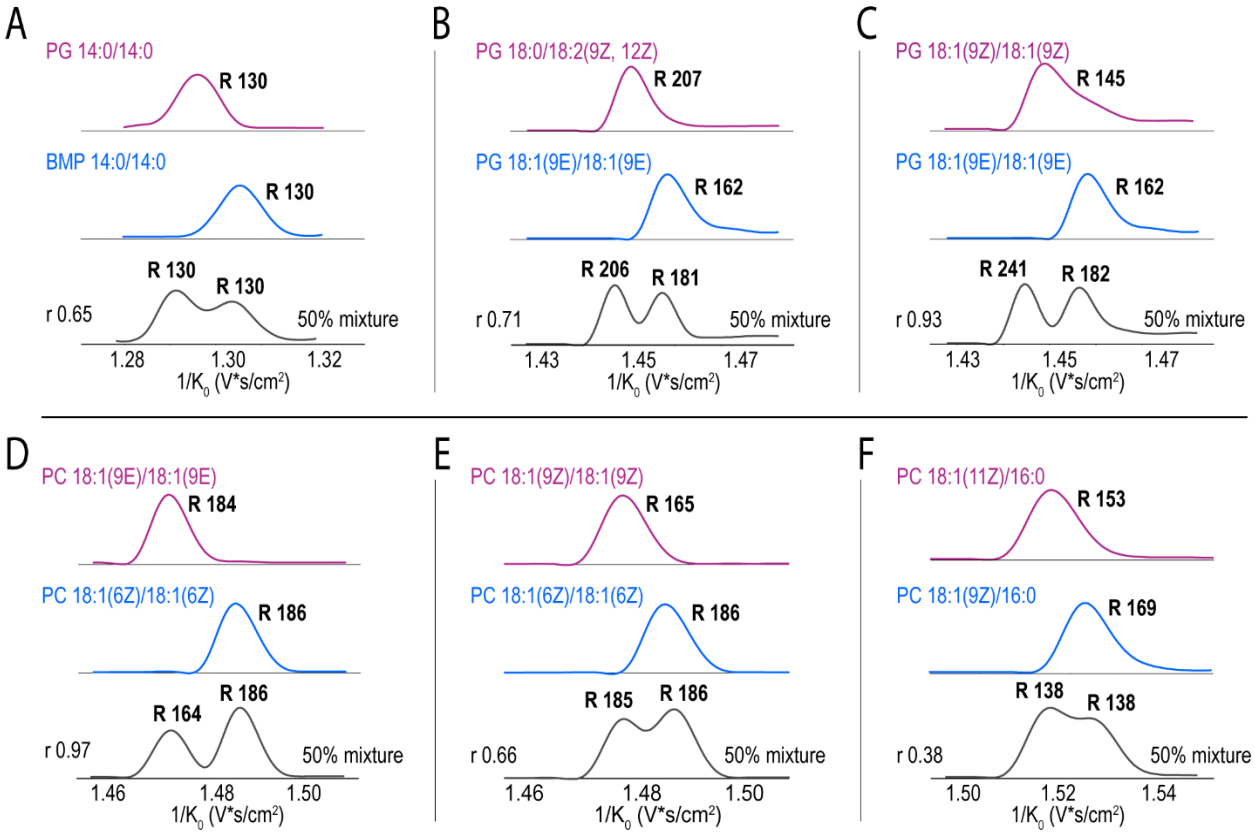

Figure 2.4. Extracted ion mobilograms of the MALDI-generated ions of isomeric lipid standards for both negative **(A – C)** and positive ionization mode **(D – F)**. Analysis of *sn* backbone isomers PG (14:0/14:0) and BMP (14:0/14:0) ($[M - H]^-$, *m/z* 665.49) **(A)**; analysis of double-bond position and stereoisomers PG (18:0/18:2 (9Z, 12Z)) and PG (18:1/18:1 (9E)) **(B)** and PG (18:1(9Z)/18:1 (9Z)) and PG ((18:1(9E)/18:1(9E)) ($[M - H]^-$, *m/z* 773.53) **(C)**. Analysis of double-bond position and stereoisomers: PC (18:1(9E)/18:1(9E)) and PC (18:1(6Z)/18:1(6Z)) **(D)** and PC (18:1(9Z)/18:1(9Z)) and PC(18:1(6Z)/18:1(6Z)) ($[M + Na]^+$, *m/z* 808.57) **(E)**, as well as PC (18:1(11Z)/16:0) and PC18:1(9Z)/16:0) ($[M + Na]^+$, *m/z* 782.56) **(F)**. Resolving power (*R*) and resolution (r) are listed where appropriate. Reprinted with permission from Djambazova et. al., Analytical Chemistry (2020) Copyright 2020 © American Chemical Society.

MALDI TIMS Separation and Localization of the Lipid Isomers *in situ*

MALDI TIMS-IMS was used to visualize the spatial distribution of the lipid isomers in whole-body mouse pup tissues. From the average mass spectrum, an example of isomeric overlap was highlighted at *m/z* 718.58, where three distinct species were resolved in the extracted ion mobilogram (**Figure 2.5A**). A composite ion image for *m/z* 718.58 including all mobility-resolved conformers ($1/K_0$ 1.410 - 1.452) (**Figure 2.5A**) was generated, followed by ion images for each ion mobility-separated species (**Figure 2.5B-D**). Each ion has a unique spatial distribution within the mouse pup tissue. The ion with $1/K_0$ 1.419 (**Figure 2.5B**) is the highest-intensity ion that localizes to the organs of the abdominal cavity, the spinal cord, and the brain with lower intensity. The ion with $1/K_0$ 1.436 (**Figure 2.5C**) localizes primarily to the liver and the connective tissue and is completely absent in the brain. Finally, the ion with mobility $1/K_0$ 1.449 (**Figure 2.5D**) localizes to the liver and has very low intensity or is below the limits of detection throughout the rest of the body. From the composite image, the highest-intensity ion ($1/K_0$ 1.419) dominates the ion image, and the spatial distributions of the other two conformers are not observed. An overlay

image of each of the ion mobility-resolved species is shown in **Figure 2.5E** highlighting the unique spatial distributions of each lipid. To determine if these ions were isobars or isomers, and to assist in identification, a serial section of the whole-body mouse pup was analyzed using MALDI FT-ICR MS, as described in the methods section. The whole-body average FT-ICR spectrum suggests that the ions separated in mobility space are, in fact, isomers, tentatively identified as $[CerP(t40:1)+ H]^+$, $[PC(O-32:1) + H]^+$, and $[PC(P-32:0) + H]^+$ (0.14 ppm error). This data further confirms that the composite ion image of *m/z* 718.58 is biased toward the most intense ion in the mass spectrum.

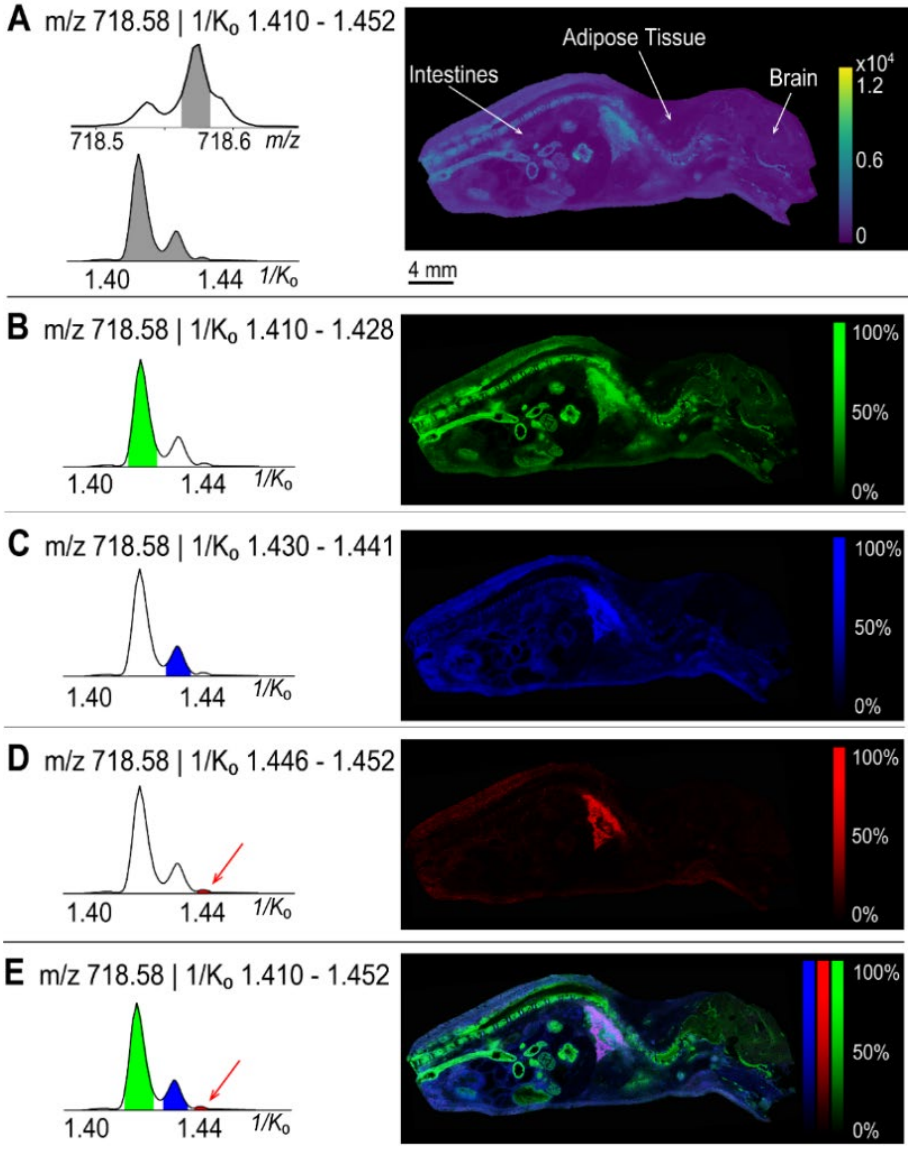

Figure 2.5. MALDI TIMS IMS separation and visualization of lipid isomers in a whole-body mouse pup. A composite image of all three peaks in the extracted ion mobilogram ($1/K_0$ 1.410–1.452) of *m/z* 718.58 is shown in panel **(A)**. Each panel highlights an ion image generated for three distinct mobility range, $1/K_0$ 1.410 – 1.428 **(B)**, 1.430 – 1.441 **(C)**, and 1.446 – 1.452 **(D)**, and an overlay of all three mobility peaks in panels **(E)**. The average ion image **(A)** is dominated by the spatial distributions of the highest-intensity ion **(B)**. Reprinted with permission from Djambazova et. al., Analytical Chemistry (2020) Copyright 2020 © American Chemical Society.

CONCLUSION

This work demonstrated the use of a MALDI timsTOF IMS for enhanced peak capacity and lipid isomer differentiation. Additional 669 features were detected by incorporating TIMS, resulting in a threefold increase in peak capacity. MALDI TIMS separation of the lipid isomer standards, including *sn*-backbone isomers, acyl chain isomers, and double-bond position and stereoisomers, was also demonstrated. Of note is the partial separation of PC (18:1(9Z)/16:0) and PC (18:1(11Z)/16:0) because the two species vary in a single double-bond location and require high resolving powers (> 250) to separate in mixtures. Resolving these standards lays important groundwork for further MALDI TIMS-IMS experiments, as both species are present in biological tissues, but may differ in relative abundances and spatial distributions.

Finally, *in situ* separation and imaging of the lipid isomers with distinct spatial distributions was performed using whole-body mouse pup section. Gas-phase isobar and isomer separations confirm TIMS as a valuable tool that can bring new dimensions to IMS experiments. Lipid identification, however, remains a challenge, and TIMS data was supplemented with MALDI FT-ICR imaging to provide tentative lipid isomer identifications. Here, we show that incorporating TIMS in a MALDI IMS workflow enhances the specificity of the experiment. Building on this, future multimodal studies that combine high-performance MALDI TIMS with advanced structural identification methods have the potential to further increase the depth of characterization of the lipids *in situ*.

METHODS

Materials

Acetic acid, ammonium formate, DAN and DHA were purchased from Sigma-Aldrich Chemical Co. (St. Louis, MO, USA). High-performance liquid chromatography (HPLC)-grade acetonitrile, methanol, ethanol, isopropanol, chloroform, and tetrahydrofuran (THF) were purchased from Fisher Scientific (Pittsburgh, PA, USA). Lipid standards were purchased from Avanti Polar Lipids (Alabaster, AL, USA).

Sample Preparation

For tissue preparation, 1 week old C57BL/6 control mouse pup was snap-frozen at −80 °C, shaved over dry ice, and cryosectioned (20 μm thickness) using a CM3050 S cryostat (Leica Biosystems, Wetzlar, Germany). The tissue was thaw-mounted onto conductive ITO-coated glass slides (Delta Technologies, Loveland, CO). The tissue section used for the Na^+/H^+ ambiguity study was prepared by sublimating DAN matrix onto the tissue surface (~1.0 mg/cm^2). For matrix deposition, slides containing tissue were taped to the bottom of the condenser in a simple sublimation apparatus. Approximately 500 mg of DAN was sublimed at 130 °C and 24 mTorr for 3.5 min. For all other mouse pup tissue analyses described in this chapter, tissue sections were placed on a heated metal block (75 °C) and coated with a 15 mg/mL solution of DAN dissolved in THF using a TM Sprayer (HTX Technologies, LLC, Chapel Hill, NC) operating with 0.05 mL/min flow rate, 5 passes, 0 s drying time, and 40 °C spray nozzle. For lipid standard analyses, the standards (in chloroform) were aliquoted in vials (5 mg/mL), dried down with nitrogen gas, and dissolved in 80% methanol for a final concentration of 1.0 mg/mL. The aliquots were then mixed

with DHA matrix and dissolved in 90% acetonitrile for a final lipid concentration of 0.2 mg/mL. The mixtures were spotted on a polished steel plate - MTP AnchorChip target (Bruker Daltonics, Bremen, Germany).

MALDI TIMS IMS

All experiments were carried out on a prototype MALDI timsTOF Pro mass spectrometer (Bruker Daltonics, Bremen, Germany). The mouse pup section used for the Na^+/H^+ ambiguity study was acquired in TIMS mode of operation with an ion transfer time of 80 µs, prepulse storage time of 10 µs, collision RF of 2000 Vpp, TIMS funnel 1 (accumulation) RF of 350 Vpp, TIMS funnel 2 RF (analysis) of 400 Vpp, multipole RF of 500 Vpp, and a collision cell entrance (in) voltage of 300 V. Imaging data were acquired at 50 µm spatial resolution with beam scan on (46 µm) using 400 shots per pixel and 60% laser power. Data were collected in positive ionization mode from *m/z* 50 to 1500. The TIMS EFG scan time was set to 400 ms, with a $1/K_0$ range of 0.900 – 1.800 $(V \cdot s)/cm^2$. All remaining mouse pup data were acquired in TIMS mode of operation with an ion transfer time of 100 µs, prepulse storage time of 8 µs, collision RF of 2000 Vpp, TIMS funnel 1 RF of 450 Vpp, TIMS funnel 2 RF of 400 Vpp, multipole RF of 400 Vpp, and collision cell entrance voltage of 300 V. Tissue imaging data (1 96 514 pixels) were collected at 50 µm spatial resolution with beam scan on (46 µm) using 200 shots per pixel and 48% laser power. Data were collected in positive ionization mode from *m/z* 50 – 1500. The TIMS EFG scan time was set to 650 ms with a $1/K_0$ range of 1.370 – 1.520 $(V \cdot s)/cm^2$ (S_r = 0.03 V/ms).

The lipid standards data were acquired in TIMS mode of operation with the specific tuning of TIMS ramp time, mobility range, and scan rate for each of the analyzed standards. Data were acquired at 20 µm spatial resolution with ~25% laser power at 10 kHz, 200 shots per pixel, and ~200 pixels per sample. Based on the laser repetition rate and the number of shots per pixel, the ion accumulation time per pixel was 20 ms. For all isomer standard experiments, t_{ramp} was kept constant (650 ms) and the mobility range was manipulated such that ΔV_{ramp}, and therefore scan rate (S_r = ~0.01 V/ms), were kept constant across all experiments. A full list of the experimental parameters is included in **Table 2.1**.

Table 2.1. TIMS Parameters Optimized for Lipid Standard Analysis

Lipid	Ion	t_{ramp} (ms)	$1/K_0$	V_{ramp} (V)	ΔV (V)	Sr ($V.ms^{-1}$)
Negative ion mode						
PG (14:0/14:0) BMP (14:0/14:0)	$[M-H]^-$	650	1.24 – 1.31	139.0 – 129.7	9.3	0.014
PG (18:0/18:2 (9Z,12Z)) PG (18:1/18:1 (9E))	$[M-H]^-$	650	1.35 – 1.42	153.5 – 144.2	9.3	0.014
PG (18:1/18:1 (9Z)) PG (18:1/18:1 (9E))	$[M-H]^-$	650	1.35 – 1.42	153.5 – 144.2	9.3	0.014
Positive Ion Mode						
PC (18:1/18:1 (6Z)) PC (18:1/18:1 (9E))	$[M+Na]^+$	650	1.44 – 1.49	164.1 – 156.9	7.2	0.011
PC (18:1/18:1 (6Z)) PC (18:1/18:1 (9Z))	$[M+Na]^+$	650	1.44 – 1.49	164.1 – 156.9	7.2	0.011
PC (18:1(9Z)/16:0) PC (18:1(11Z)/16:0)	$[M+Na]^+$	650	1.42 – 1.46	159.8 – 154.1	5.7	0.009

TIMS imaging data was visualized using custom in-house developed software and SCiLS (Bruker Daltonics, Billerica, MA, USA). Lipid identifications were determined with high mass accuracy, and LIPIDMAPS lipidomics gateway (lipidmaps.org)[119] and/or by performing MS/MS in the collision cell of the prototype MALDI timsTOF platform (40 V CID).

MALDI FT-ICR IMS & MS/MS

To assist in molecular identification, high-mass-resolution imaging mass spectrometry of whole-body mouse pup tissue was performed using a 15T MALDI FT-ICR mass spectrometer (Bruker Daltonics, Billerica, MA, USA). The instrument is equipped with an Apollo II dual MALDI/ESI ion source and a Smartbeam II 2 kHz frequency tripled Nd: YAG laser (355 nm). Images were generated using the "small" laser setting of ~50 μm with a pixel spacing of 150 μm in both the *x* and *y* dimensions. The recorded mass spectrum had a *m/z* range of 460 – 1500 with a transient length of 4.2 s resulting in a resolving power of ~600,000 at *m/z* 760.

Data Processing and Data Analysis

Imaging

The mouse pup data was exported into a custom binary format optimized for storage and speed of analysis of the ion mobility-IMS data collection. Each frame/pixel contains between 10,000 and 100,000 centroid peaks that span the acquisition range of *m/z* 50 – 1500 and $1/K_0$ 1.370 – 1.520 (Vs)/cm^2 with 400,577 and 5857 bins in the MS and ion mobility dimensions, respectively. For the Na^+/K^+ dataset, those parameters are as follows: acquisition range of *m/z* 300 – 1200 that consists of 221 888 and 4001 bins in the MS and ion mobility dimensions, respectively. The processing pipeline requires common *m/z* and $1/K_0$ axes, hence individual centroid peaks were inserted at their correct bin position along the MS and ion mobility dimensions; missing values were set to zero. Following the conversion process, a mean mass spectrum of the entire data set was generated and peak picked. A total of ~400 most intense ions were then selected and extracted to generate ion mobility-rich ion images. Each of the extracted ion mobility-ion images was peak-picked (in the ion mobility dimension) and automatically fitted with Gaussian distributions to identify single and multiconformational species. Ion mobility-selected ion images were then visualized to examine the conformational-specific localization in the spatial domain.

Peak capacity

A peak in the *m/z* domain corresponds to a spectral feature for which the area under the curve (AUC) was calculated and the full-width at half-maximum (FWHM) was determined. An in-house developed peak picker was used to create a list of spectral features found in the average mass spectrum, which were then filtered based on the minimal intensity (>0.1% of the base peak). In the TIMS dimension, a peak corresponds to a feature that was fitted with a single Gaussian curve allowing for the calculation of the AUC and FWHM. Ion mobility profiles containing multiple conformations were fitted with multiple Gaussian peaks to represent the profile, as a single *m/z* species can have several ion mobility features. For lipid standard analysis an average mass spectrum of each dataset was opened in DataAnalysis (Bruker Daltonics, Billerica, MA, USA), where the extracted ion mobilograms of each ion of interest were generated.

CHAPTER III

EXPANDING MALDI TIMS COVERAGE FOR HIGH MASS ANALYSIS: GANGLIOSIDES

This chapter was in part adapted from *MALDI TIMS IMS of Disialoganglioside Isomers – GD1a and GD1b in Murine Brain,* with permission from the co-authors.

OVERVIEW

Gangliosides are complex acidic glycosphingolipids with essential functions in the mammalian nervous system. Intact ganglioside analysis can be challenging due to their amphiphilic character and tendency toward in-source fragmentation. Thus, soft ionization sources, such as MALDI, have been preferred for MS analysis of gangliosides. Here, we demonstrate the MALDI TIMS IMS of gangliosides *in situ*. First, sample preparation considerations were optimized to enhance signal intensity, limit in-source fragmentation, and reduce analyte delocalization for high spatial resolution analysis of gangliosides. Salt deposition strategies, namely washing and spraying the tissue section prior to analysis with ammonium sulfate and ammonium formate were tested. Following salt deposition, different matrices were tested and compared, namely DAN, DHB, DHA, and ACA. The TIMS dimension was then incorporated to distinguish isomeric gangliosides - GD1a and GD1b in a 1:1 mixture, a total porcine brain ganglioside extract, and directly within thin tissue sections. Lastly, the unique spatial distributions of GD1a/b(d36:1) and GD1a/b(d38:1) in both rat brain and spinal cord samples were mapped at 20 μm spatial resolution.

INTRODUCTION

Gangliosides are acidic glycosphingolipids, highly abundant in the mammalian nervous system.[73,81] As critical components of neuronal and glial cells, they play an essential role in neuronal development and maturation, as well as cellular signaling.[120,121] These molecules have been implicated in brain injury[122], as well as in neurological diseases including Guillain-Barre syndrome[123–125], Alzheimer's[90,126], and Huntington's disease[127], and remain an active area of interest for developing therapeutics.[126]

Gangliosides consist of a hydrophobic ceramide lipid backbone and a hydrophilic oligosaccharide chain of varying length with one or many sialic acid residues.[80,81] The major mammalian brain gangliosides - GM1, GD1a, GD1b, and GT1b share the same tetrasaccharide core and make up over 80% of the entire mammalian ganglioside content.[128] Of the highlighted gangliosides, GD1a and GD1b differ in the position of a single sialic acid, where GD1a has a sialic acid on the internal and terminal galactose units, and GD1b has both sialic acids in a chain attached to the internal galactose. In addition to the sialic acid location, the diversity in ceramide/oligosaccharide chain composition also contributes to the large number of ganglioside isomers. This greatly increases structural complexity and presents a challenge for comprehensive analysis of this class of biomolecules.[81,83]

Traditionally, ganglioside distributions in murine brain tissues are characterized using immunohistochemistry (IHC) approaches.[129,130] These techniques provide carbohydrate epitope information, but have a risk of cross reaction with glycoproteins carrying similar sugar chains

causing false-positive identification and localization.[87,128,130] Furthermore, a drawback of IHC is that it provides no information on ceramide backbone composition. Since the biological function of gangliosides is dictated by both the carbohydrate chain and the ceramide moieties, analysis of gangliosides in their intact form is crucial for understanding their roles in different physiological processes.[87,128,130] MS has been a critical tool for the detection and characterization of intact gangliosides due to its high specificity and sensitivity..[79,131] However, some MS approaches cause extensive precursor ion fragmentation in gangliosides, where the sialic acid bonds are particularly labile. Soft ionization techniques, including ESI and MALDI have therefore been preferred for ganglioside analysis. [84,132,133]

MALDI IMS has previously been employed to map the localization of gangliosides within biological tissues, however, a significant difficulty of ganglioside analysis is the in-source fragmentation of polysialylated gangliosides, such as GDs, GTs, and GQs.[134–136] The most-commonly observed in-source fragmentation is the loss of sialic acid(s), which results in artificially high intensities of monosialylated GM species. This poses a challenge for both quantitation and accurate representation of analyte spatial distributions in a MALDI IMS experiment. Because of this, sample preparation strategies must be carefully considered. The MALDI IMS workflow for ganglioside analysis can include several steps, such as washing or spraying the tissue with salts, as well as choosing an appropriate matrix and deposition strategy. Common matrices for ganglioside analysis include 5-chloro-2-mercaptobenzothiazole (CMBT), DAN, DHB, and DHA. Of the mentioned, DAN and CMBT more readily induce in-source fragmentation but have high vacuum stability. DHB is also vacuum stable, however, it requires a washing step to limit the interference of other lipids and salts. Lastly, DHA can reduce in-source fragmentation, but has lower vacuum stability, and also may require a washing step prior to matrix application. Previous literature has shown that introducing ammonium formate (AmF) or ammonium sulfate (AmS) increases the intensity and coverage gangliosides.[137,138] Nonetheless, a systematic approach to investigate sample preparation is needed to further improve MALDI IMS analysis of gangliosides. In-tact analysis of gangliosides is essential for obtaining biologically relevant information. Furthermore, resolving ganglioside isomers remains a significant challenge without the use of additional techniques, such as TIMS.

Ion mobility separations can be integrated with MS to address ganglioside structural complexity and isomerism. For example, Ekroos and coworkers recently demonstrated the separation of isomeric GD1a(d36:1) and GD1b(d36:1) using a prototype SLIM-MS instrument.[93] The gangliosides were resolved both in a 1:1 mixture, as well as in a wild-type hemi-brain mouse brain extract. Jackson *et. al*. have demonstrated the combination of ion mobility and MALDI for the analysis of GD1a and GD1b, where they showed higher drift times for the GD1a isomer.[138] Woods and coworkers have reported the distributions of GD1(d36:1) after a water loss (*m/z* 1817), to provide some insight into the possible spatial localizations of GD1b.[86] This was possible, as GD1b more readily undergoes a water loss than GD1a. However, the spatial distributions of a- and b-series ganglioside isomers have not been directly demonstrated in a MALDI imaging context thus far.

Here, we demonstrate MALDI TIMS IMS of in-tact gangliosides *in situ*. First, sample preparation considerations were optimized to enhance signal intensity, limit in-source fragmentation, and reduce analyte delocalization for high spatial resolution analysis. Salt deposition strategies, namely washing and spraying the tissue section prior to analysis with ammonium sulfate and ammonium formate were tested. Following this, common matrices including DAN, DHB, DHA, and 4-acinaminic acid (ACA) were compared for ganglioside

analysis. The TIMS dimension was then incorporated to distinguish isomeric gangliosides - GD1a and GD1b in a 1:1 mixture, a total ganglioside extract, and directly within tissue sections. Lastly, the unique spatial distributions of GD1a/b(d36:1) and GD1a/b(d38:1) were mapped in both rat brain and spinal cord samples at 20 μm spatial resolution.

RESULTS AND DISCUSSION

Sample Preparation Considerations for Ganglioside Analysis

High spatial resolution imaging of gangliosides with minimal delocalization and in-source fragmentation remains a challenge for MALDI IMS. Here, common sample preparation strategies including salt deposition, matrix choice and deposition method were compared and optimized for *in situ* ganglioside analysis. For these experiments, rat brain homogenates and sagittal rat brain tissue sections were used to evaluate sample preparation conditions. Ultimately, the decoupled deposition of ammonium sulfate, followed by ACA matrix was determined to be the optimal sample preparation procedure for MALDI IMS of gangliosides.

Effects of Laser Power on in-source Fragmentation

One of the most significant difficulties of ganglioside analysis is the in-source fragmentation of polysialylated species, such as GDs, GTs, and GQs. The most-commonly observed in-source fragmentation is the loss of sialic acid(s), which results in artificially high intensities of monosialylated GM species.[79,83] This poses a challenge for both quantitation and accurate representation of analyte spatial distributions in a MALDI IMS experiment. A major impact on in-source fragmentation in a MALDI experiment is the laser energy imparted on the analytes as well as the choice of matrix. To illustrate the severity of the in-source fragmentation a total porcine brain ganglioside extract was spotted and analyzed by MALDI IMS. Here, the laser power per pixel was continuously increased in increments of 10% from 20% to 80% to illustrate the tendency toward sialic acid loss. The relative intensity of GM1-GD1-GT1-GQ1 was monitored for the two most abundant gangliosides in each class - d36:1 and d38:1 (**Figure 3.1**). **Figure 3.1** shows that with the increase of laser power, the relative intensity of polysialylated gangliosides decreased, where the intensity of the GM1s increased. This experiment shows the importance of relative laser power and matrix choice on *in situ* ganglioside analysis. Namely this analysis shows that matrices, allowing for lower laser power are preferred for intact ganglioside analysis.

Salt deposition - Tissue Washing and Spraying

First, we tested the effects of tissue washing on rat brain sections with AmF and AmS of varying concentrations (25 to 150 mM) and durations (5 – 160 sec). The effectiveness of the washes for ganglioside analysis were assessed by monitoring the relative intensities of d36:1 and d38:1 species and by assessing the degree of analyte delocalization by measuring analyte diffusion beyond the tissue boundary. For salt deposition comparisons, DHA matrix was used, as described in the Methods section. Previously, Yang et. al[137] have shown that washing and subsequently spraying tissues with AmF increases the intensity and number of detected gangliosides. Similarly, we found that even a 5 second wash with either AmF or AmS, regardless of the concentration, increased signal intensity and number of detected species in comparison to no tissue wash.

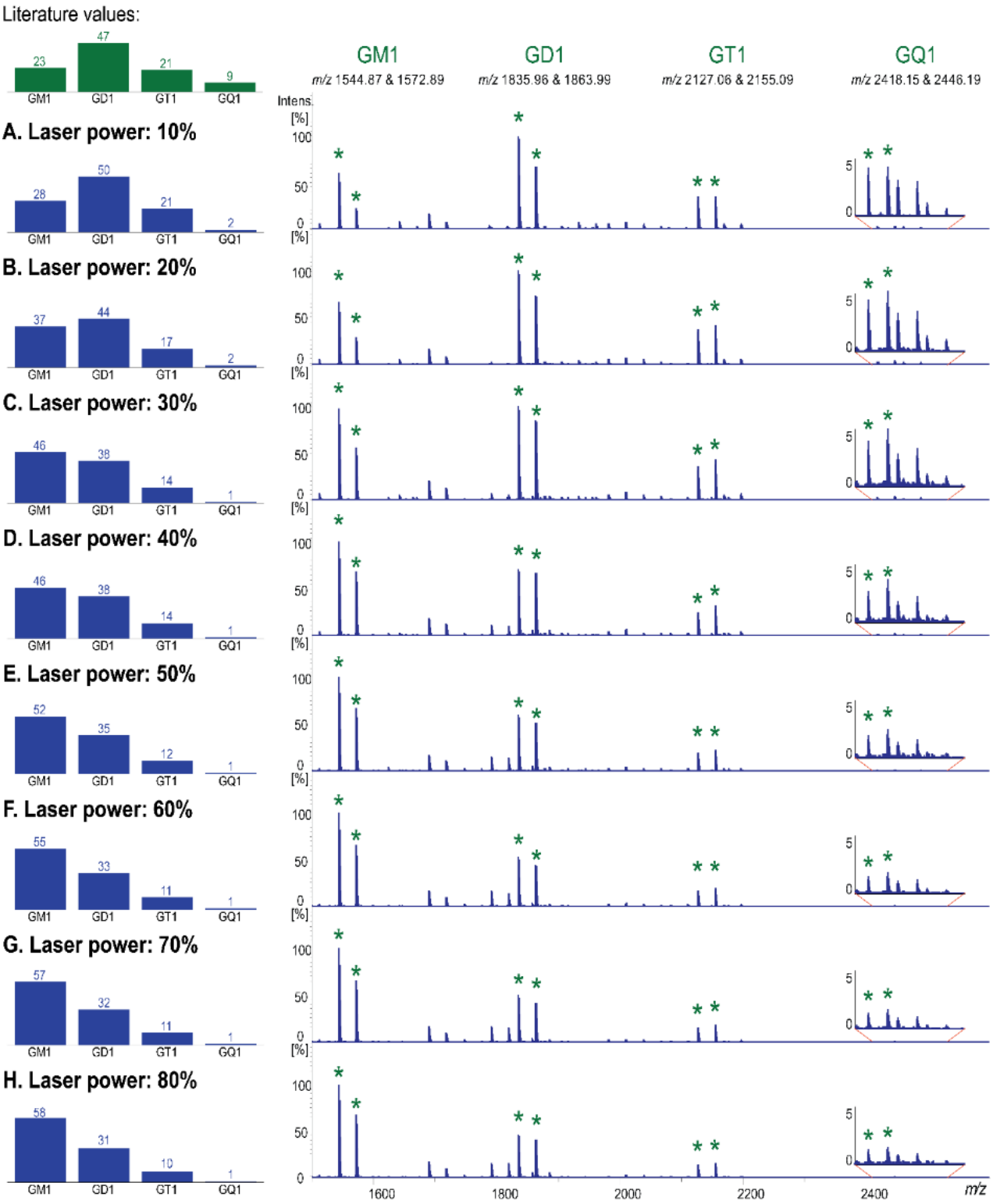

Figure 3.1 The effects of MALDI laser power on in-source fragmentation of polysialylated ganglioside species demonstrated for a total porcine ganglioside extract by tracking the relative intensities of GM1-GD1-GT1-GQ1 species with both d36:1 and d38:1 ceramide composition. Laser energy was increased from 10 % (A) to 80 % (H) and the relative intensities of each ganglioside class (in green) were compared to literature values.

However, analyte delocalization was observed for all washes, regardless of composition and duration, as gangliosides are soluble in both water and commonly used organic solvents (**Appendix 6.6**). As spatial integrity is of utmost importance to high spatial resolution IMS, we concluded that any wash prior to matrix deposition would not be suitable.

Alternatively, AmF and AmS sprays prior to (or with) matrix deposition were tested. As a starting point, a sample preparation method pioneered by Woods and coworkers[86] was used. This method includes a simultaneous spray of AmS and 2,6-DHA matrix in 60% ethanol. Here, 2,5-DHA was used instead of 2,6-DHA for enhanced vacuum stability[139] (**Methods, Table 3.1**). We found that spraying either AmS or AmF with DHA increased ganglioside signal, as compared to DHA alone. When comparing both salt sprays, we found that AmS outperformed AmF in terms of ganglioside signal and observed in-source fragmentation, regardless of concentration. To assess performance for ganglioside analysis, the mass spectral integrity, uniformity of matrix/salt deposition, and ion image integrity were assessed. Some analyte delocalization was observed; however, it was much less pronounced in comparison to tissue washing. The simultaneous salt and matrix deposition likely resulted in improper crystallization, due to high salt concentration and therefore non-uniform coverage, as seen in the scanning electron microscopy (SEM) image (**Figure 3.2A**). In terms of spatial integrity, this method was limited in spatial resolution (30 µm) and resulted in hot spots in the MALDI IMS data, as demonstrated in **Figure 3.2B**. Thus, we concluded that simultaneous salt and matrix deposition was not suitable for high spatial resolution MALDI IMS of gangliosides.

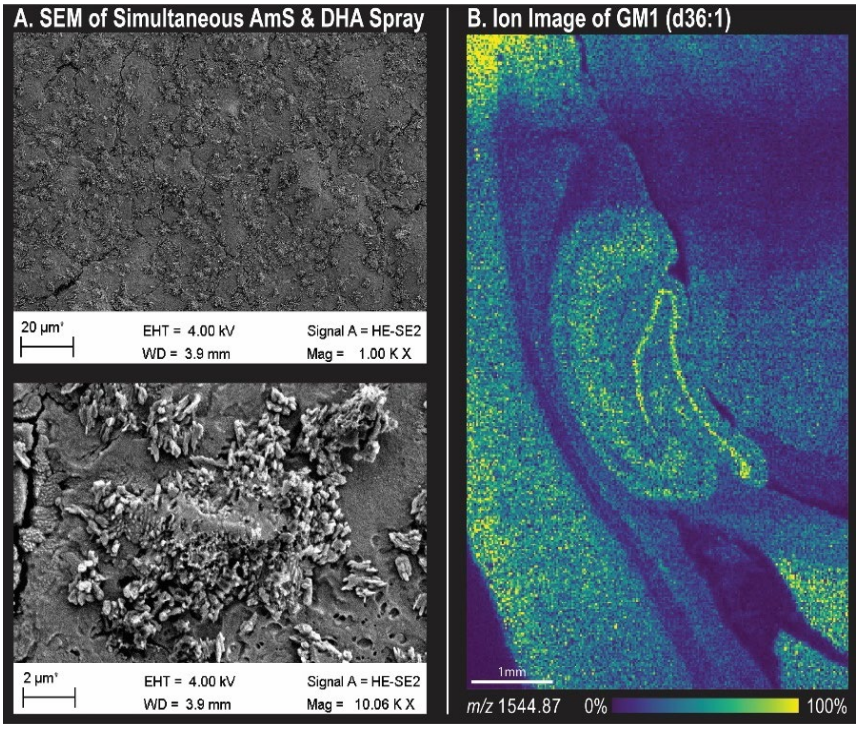

Figure 3.2. Scanning electron microscopy image of rat brain tissue surface following the simultaneous spray of AmS and DHA **(A)**; ion image of GM1(d36:1), *m/z* 1544.87 demonstrates hot spots in the ion image **(B)**.

The matrix and AmS have very different properties and require different solvent compositions for adequate deposition on the tissue surface. For this purpose, we aimed to decouple the AmS and matrix spray and optimize deposition parameters for each spray individually. Decoupling the AmS and matrix deposition allowed for AmS to be deposited in ethanol-water and DHA to be deposited in a pure organic solvent which favors the formation of smaller crystal size making it amenable to high spatial resolution MALDI IMS. As noted by Dufresne et. al.[140], using a matrix solvent in which salts are not soluble creates an environment akin to sublimation. Ultimately, the most suitable method of AmS deposition was 62.5mM AmS in 60% ethanol-water, for a theoretical on-tissue AmS density of 1.48 µg/mm^2 (**Methods, Table 3.1**). Spray considerations for AmS deposition of note include an increase of the nozzle pressure to 15 psi to

facilitate nebulization and the formation of smaller crystals. Additionally, the spray method was slower, 25 passes at a spray rate of 0.01 mL/min, allowing for lower solvent/nitrogen gas mixing, leading to drier spray conditions. This allowed for the formation of smaller crystal sizes and reduced delocalization typically observed with wetter deposition. Once the salt was deposited, the matrix application could be further optimized individually, as described in the following section.

Matrix Selection

Following an optimized ammonium sulfate deposition protocol, different MALDI matrices, including DAN, DHB, DHA, and ACA, were evaluated for ganglioside analysis on rat brain homogenates. In all cases, the matrices were deposited with an organic solvent to minimize matrix/salt interaction and crystal sizes. Furthermore, since the AmS is not dissolvable in organic solvent, no significant interactions of matrix and salt delocalization was expected following the matrix application. Average mass spectra of small regions of interest (ROIs) of rat brain homogenates were acquired and compared in terms of relative ganglioside signal intensities across ganglioside class, degree of in-source fragmentation, and spatial integrity. All of the highlighted matrices allowed for high spatial resolution (10 μm) ganglioside analysis but varied in terms of mass spectral and spatial integrity. DAN and DHB induced significant in-source fragmentation; DHB is a known "hot" matrix, which required relatively higher laser power (~70%, respectively) further contributing to in-source fragmentation. Both DHA and ACA required significantly lower energy power (~30 and 35%, respectively), where DHA induced a higher degree of sialic acid loss, as evidenced by the relative GM-GD-GT-GQ ratio: DHA: 46-40-13-1, as compared to ACA: 39-44-16-1 (**Figure 3.3A**). Finally, ion images of the gangliosides across the four classes for d36:1 were generated for a rat hippocampus region and compared in terms of spatial integrity (**Figure 3.3C**). Visually comparing the ion images, it can be seen that the DHA method had more hot spots in comparison to ACA, indicating that ACA facilitates higher quality MALDI imaging data. The lower levels of in-source fragmentation, higher spatial quality, and significantly higher vacuum stability achieved with ACA indicate that ACA is the preferred matrix for MALDI IMS of gangliosides.

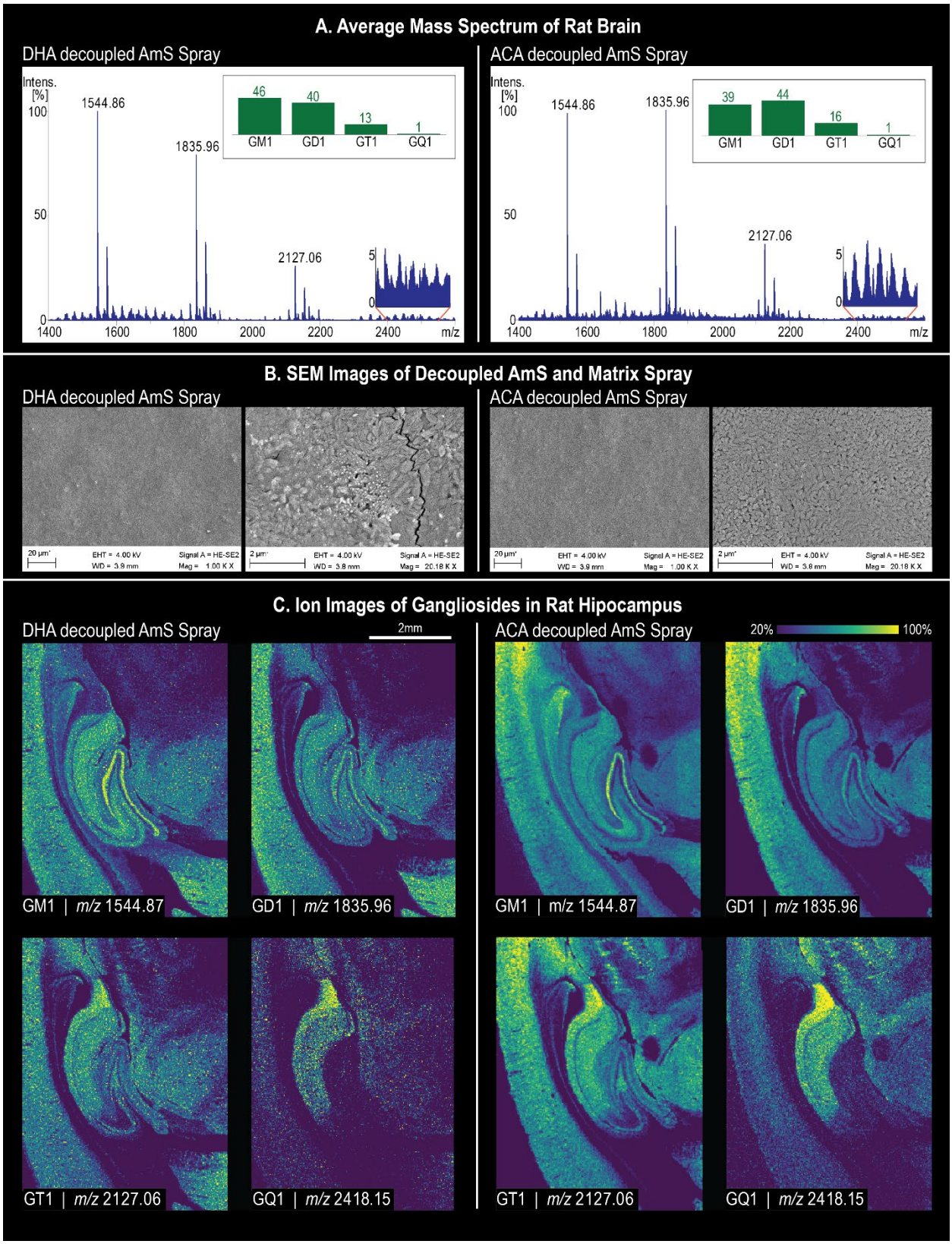

Figure 3.3. Comparisson of decoupled ammonium sulfate and DHA (left column) and ACA (right colum) in terms of mass spectral signal and relative intensity of ganglioside species by class **(A)**, SEM images of the matrix coverage of the tissue **(B)**; and ion images of d36:1 across four of the detected ganglioside classes – GM1, GD1, GT1, and GQ1 **(C)**.

MALDI TIMS IMS of Ganglioside Isomers GD1a/GD1b

GD1a/GD1b Isomer Analysis from Standard Extracts

Gangliosides GD1a and GD1b are disialogangliosides that differ in the location of a single sialic acid residue on the oligosaccharide chain. GD1a has a sialic acid on the internal, as well as on the terminal galactose unit, whereas the GD1b isomer has both sialic acids in a chain attached to the internal galactose. Differentiating the two isomers is important in the context of brain tissue, as they are two of the most abundant ganglioside species in the mammalian brain. Furthermore, both have been known to be differentially impacted by diseases, such as Alzheimer's disease.

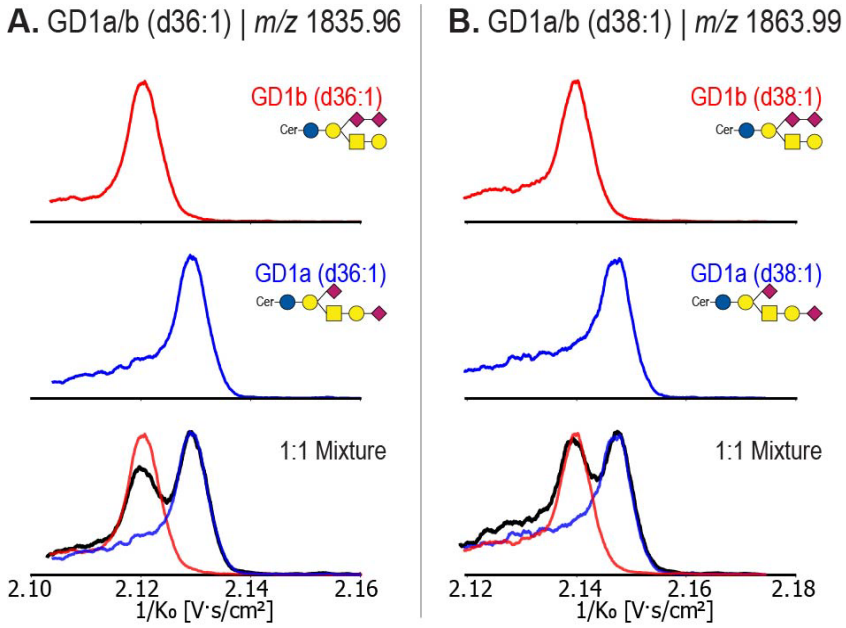

Figure 3.4. MALDI TIMS extracted ion mobilograms of deprotonated GD1(d36:1): GD1a- (blue) and GD1b- (red), were separated in a 1:1 mixture of both standards (black) **(A)**; and deprotonated GD1(d38:1): GD1a- (blue) and GD1b- (red), were separated in a 1:1 mixture of both (black) standards **(B)**

Ganglioside extracts were analyzed with high TIMS resolving power (scan rate < 0.01 V/ms, with a 1100 ms t_{ramp} time). Isomeric GD1a and GD1b were first analyzed individually to determine their respective mobilities under MALDI TIMS conditions. The two major GD1 species observed in both GD1a and GD1b standards have ceramide backbones of d36:1 and d38:1. Both species were detected as $[M-H]^-$, $[M-CO_2-H]^-$, $[M-H_2O-H]^-$, and $[M+Na-2H]^-$ adduct. Deprotonated GD1a/b(d36:1) and GD1a/b(d38:1), detected at *m/z* 1835.96 and *m/z* 1863.99 respectively, were analyzed to investigate the ability to separate GD1 isomers. Under these conditions, the individual $1/K_0$-values of deprotonated GD1b(d36:1) and GD1a(d36:1) were determined to be 2.12 and 2.13 V.s/cm^2, respectively (**Figure 3.4A**). From the extracted ion mobilogram of the mixture, a partial separation of the two isomers was observed. Using the same TIMS conditions, GD1b(d38:1) and GD1a(d38:1) isomers were partially resolved in a 1:1 mixture with $1/K_0$ values to be 2.14 and 2.15 V.s/cm^2, respectively (**Figure 3.4B**). Additionally, we analyzed a total ganglioside extract demonstrating the partial separation of GD1a/b for both (d36:1) and (d38:1) species (**Appendix 6.8**). Our findings indicate that GD1b and GD1a isomers can be partially resolved in a 1:1 mixture of standards and in a total ganglioside extract, where the b-series isomers have more compact structures leading to lower $1/K_0$ values. These findings are consistent with previous MALDI-ion mobility experiments by Jackson *et. al.* and SLIM MS experiments by Ekroos and coworkers[93].

MALDI TIMS IMS Separation and Localization of GD1a/GD1b in Murine Tissue

Rat Brain

GD1a and GD1b species are the most abundant ganglioside species in the mammalian brain. Both a- and b-series disialogangliosides have distinct localizations within the brain, previously characterized using IHC. MALDI TIMS IMS data was collected from a sagittal rat brain section (left hemisphere, lateral value ~ 0.8 - 0.9 mm) at 20 µm spatial resolution. A cresyl violet stain was used to highlight the regions of interest in the hippocampus that were analyzed by MALDI IMS (**Figure 3.5A**). Ion images of *m/z* 1835.96 (purple) and *m/z* 1863.99 (green) show the different distributions of GD1(d36:1) and GD1(d38:1), respectively, in the hippocampus (**Figure 3.5B**). Comparing the ion images with the annotated stain, we observed that GD1(d36:1) was more pronounced in the granular layer of the dentate gyrus, the pyramidal layer of the CA3 and CA2 regions, and along the fiber tracks. GD1(d38:1), on the other hand, was more pronounced in the molecular layer of the dentate gyrus, in the midbrain, and along the edges of the subiculum. The overlaid ion images represent a composite image of a- and b-series isomers for both 36:1 and 38:1. Further investigation using the TIMS mobility dimension reveled two partially resolved peaks for *m/z* 1835.96, corresponding to deprotonated GD1a(d36:1) and GD1b(d36:1). Individual standards, GD1a and GD1b, and on-tissue MS/MS were also acquired to aid in identification (**Appendix 6.9**). Ion images of each of the ion mobility peaks (**Figure 3.6A**) show the unique spatial distributions of both a-(blue) and b-(red) series isomers. GD1a and GD1b were expressed in all layers of the hippocampus but differed in their relative intensities in specific subregions. In the ion images, we observed that the a-isomer was more pronounced in the granular layer of the dentate gyrus, while the b-isomer was more abundant in the subiculum, as well as the midbrain, and thalamus, where the signal from the a-series was noticeably absent. Similarly, the extracted ion mobilogram of *m/z* 1863.99, highlighted two partially resolved ions, corresponding to a- and b-series GD1(d38:1) (**Figure 3.6B**). Although, the

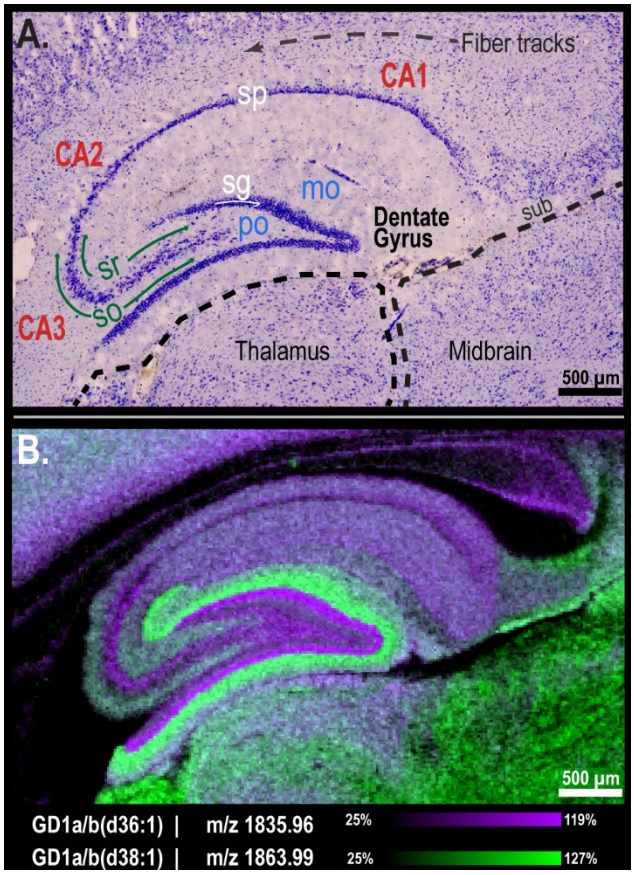

Figure 3.5. A cresyl violet stain of a sagittal rat brain section highlights features of interest in the hippocampus: Ammon's hors regions – CA1, CA2, and CA3 (in red), the dentate gyrus, the molecular layer (mo), polymorph layer (po), pyramidal layer (sp), granule cell layer (sg), stratum radiatum (sr), stratum oriens (so), and the subiculum (sub) **(A)**. Overlaid ion images of *m/z* 1835.96 (purple), and *m/z* 1863.99 (green), show the different distribution of GD1(d36:1), and GD1(d38:1), respectively, where both distributions are composite of both a- and b- series gangliosides **(B).**

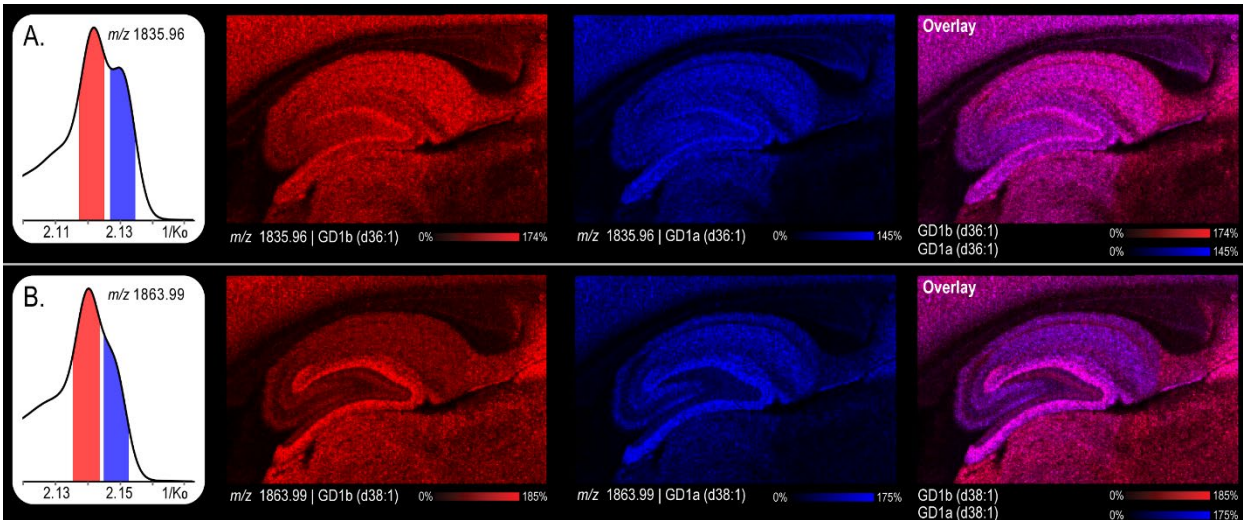

Figure 3.6. Extracted ion mobilograms of *m/z* 1835.96 **(A)** and m/z 1863.99 **(B)** demonstrate the partial separation of GD1b- (red) and GD1a (d36:1) (blue) in rat hippocampus tissue section. Ion images of GD1b (red), GD1a (blue) isomers, and an overlay of both ions can be seen for both GD1(d36:1) **(A)** and GD1(d38:1) **(B)**.

two ions were not as well resolved in the gas phase, their localizations within the rat brain tissues were very different. The a-isomer was observed in the granular layer of the dentate gyrus and was more pronounced in the striatum radiata and striatum oriens of the CA3 region. GD1b was also more pronounced in the granular layer of the CA1 and CA2 regions, where GD1a was below the limit of detection. GD1a was, however, present in the striatum radiata and the striatum oriens of CA1 and CA2. Similar to GD1a/b(d36:1), the most significant distinction between the two isomers was the detection of the a-series in the thalamus, but not the midbrain or the subiculum. These findings are consistent with previous IHC experiments of mouse and rat brains showing GD1a and GD1b localizations[129,130] and with previous IMS data highlighting the differences between GD1(d36:1) and GD1(d38:1). Woods and coworkers had previously reported mapping GD1b(d36:1) by imaging the water-loss at *m/z* 1817.95, which is more preferential for the b-series gangliosides. Here we highlight the subtle differences of GD1 subspecies that differ in both ceramide composition and sialic acid localizations. This work shows that with the combination of MALDI IMS and ion mobility separations the spatial distributions of GD1a(d36:1), GD1b (d36:1), GD1a(d38:1), GD1b(d38:1) and any combination thereof can be visualized directly within the rat brain tissue sections (**Figure 3.7A-D**). In addition to the two overlaid ion images in **Figure 3.6**, there are four additional ion overlay combinations possible, highlighted in **Figure 3.7**. As ganglioside function is influenced by the ceramide moieties and the carbohydrate chains, this level of structural specificity in an imaging context is important to further understand the role of gangliosides in biology and disease.

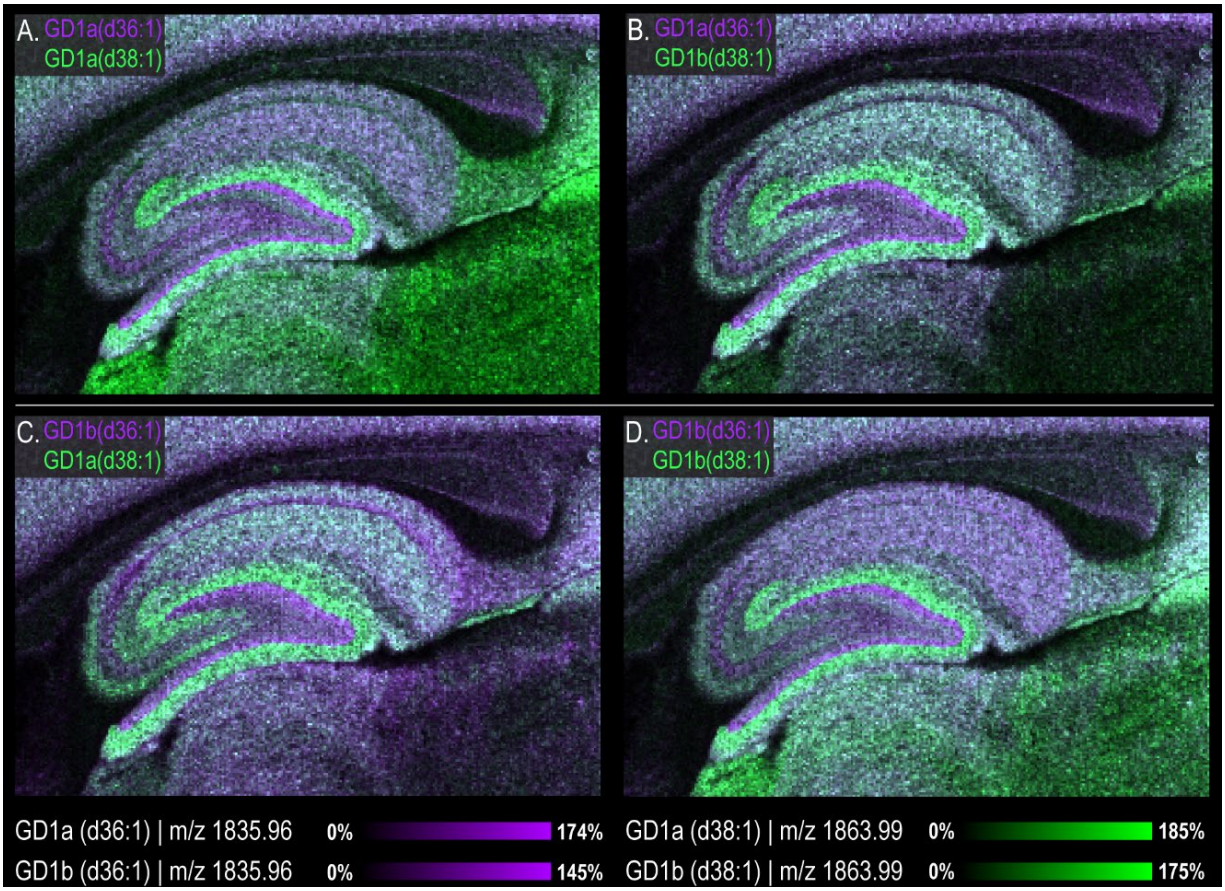

Figure 3.7. Overlay ion images of a and b-series isomers for GD1(d36:1) and GD1(d38:1): GD1a(d36:1) and GD1a(d38:1) **(A)**, GD1a(d36:1) and GD1b (d38:1) **(B)**, GD1b(d36:1) and GD1a(d38:1) **(C)**, and GD1b(d36:1) and GD1b(d38:1) **(D)**.

Spinal Cord

To further highlight the unique distributions of GD1a and GD1b isomers in murine nervous tissue, rat spinal cord tissue was also analyzed. A transverse section of the sympathetic intermediolateral horn (roughly T6 – T11 region) was selected, as the a- and b-series GD1 localizations have been previously highlighted in literature by IHC.[130] A cresyl violet microscopy image was annotated to show the regions of interest (**Appendix 6.9**). Considering the relatively small size of the tissue section, MALDI TIMS parameters were optimized to maximize the separations and demonstrate the highest resolution separation of GD1a/b isomers *in situ*.

The extracted ion mobilograms of the GD1(d36:1) and GD1(d38:1) revealed two isomeric species (**Figure 3.8A** & **3.8B**, respectively). From the ion images of *m/z* 1835.96 (**Figure 3.8A**) we can see that the isomer corresponding to the b-series was found throughout the gray matter with higher intensity in the rexed laminae 1 and 2 of the dorsal horn. The a-series isomer, on the other hand, was only present in the rexed laminae. The ion images of *m/z* 1863.99 (**Figure 3.8B**) revealed that GD1b was detected throughout the gray matter. The a-series isomer was more pronounced in the rexed laminae, but could also be detected in the gray matter, specifically around the central anal **(Figure 3.8B).** An overlay of GD1b(d36:1) and GD1b(d38:1) (**Figure 3.8C**)

revealed that the signal in the rexed laminae was mostly due to the d36:1, where the d38:1 was more pronounced in the gray matter. The overlay of GD1a(d36:1) and GD1a(d38:1) (**Figure 3.8D**) shows that GD1a(d36:1) was more intense in the lamiae than the d38:1, which was detected throughout the gray matter.

These findings are consistent with previous IHC studies that show GD1a and GD1b, and with MALDI IMS studies that show the spatial distribution of GD1(d36:1) vs GD1(d38:1) localization within murine spinal cord tissue. Neither IHC nor MALDI IMS can resolve the nuanced differences in ceramide composition and carbohydrate chain simultaneously - GD1a(d36:1) versus GD1a(d38:1). Similarly, mapping the localization of GD1a(d36:1) and GD1b(d38:1), as well as GD1b(d36:1) and GD1a(d38:1), could not be achieved with either technique alone. These examples highlight the utility of MALDI TIMS IMS for the gas-phase separation of GD1a- and b-series isomers *in situ*.

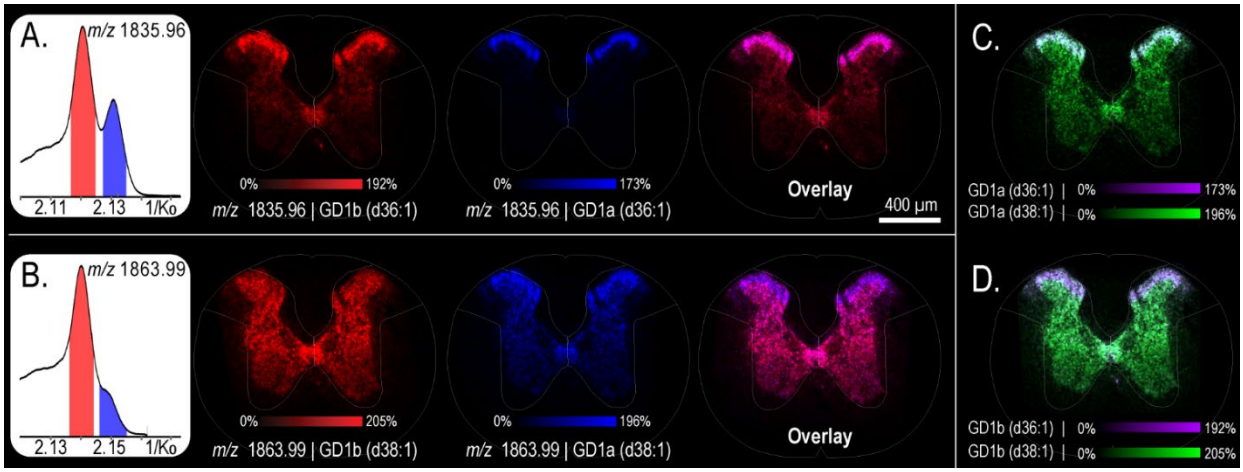

Figure 3.8. Extracted ion mobilograms of *m/z* 1835.96 **(A)** and m/z 1863.99 **(B)** demonstrate the partial separation of GD1b- (red) and GD1a (d36:1) (blue) in rat spinal cord section. Ion images of GD1b (red), GD1a (blue) isomers, and an overlay of both ions can be seen for both GD1(d36:1) **(A)** and GD1(d38:1) **(B)**. Overlay ion images of GD1a (d36:1) and (d38:1), as well as GD1b (d36:1) and (d38:1) are highlighted in **(C)** and **(D)**, respectively

CONCLUSIONS

This work highlights the importance of optimized sample preparation techniques for MALDI IMS of gangliosides. Here, sample preparation strategies, including salt and matrix deposition strategies, were compared to maximize ganglioside coverage and signal without inducing significant in-source fragmentation or analyte delocalization. Ultimately, a decoupled ammonium sulfate and ACA spray was determined to be most suitable for high spatial resolution MALDI IMS of intact gangliosides. Following sample preparation optimization, the TIMS dimension was incorporated to resolve isomeric polysialylated gangliosides – GD1a and GD1b. The spatial distributions of isomeric GD1a/b (36:1) and GD1a/b (38:1) were elucidated for rat brain and spinal cord samples. This level of structural specificity in a spatially resolved context cannot be achieved through standard IHC experiments, nor typical MALDI IMS workflows. The ability to both structurally characterize and spatially map gangliosides with high specificity *in situ* using integrated TIMS separation will enable new biomedical studies that may reveal the role of this important class of molecules in health and disease.

METHODS

Materials

DHA, DAN, DHB, ACA, ammonium formate, and ammonium sulfate were purchased from Sigma-Aldrich (St. Louis, MO, USA). HPLC-grade acetonitrile, methanol, ethanol, tetrahydrofuran, and chloroform were purchased from Fisher Scientific (Pittsburgh, PA, USA). Ganglioside extracts were purchased from Avanti Polar Lipids (Alabaster, AL, USA), normal rat brain was purchased from BioIVT (Westbury, NY, USA), and rat spinal cord was purchased from Pel-Freeze Biologicals (Rogers, AZ, USA).

Sample Preparation

Rat brain and spinal cord were cryosectioned to 10 µm thickness using a CM3050 S cryostat, and thaw-mounted onto conductive ITO-coated glass slides (Delta Technologies, Loveland, CO, USA). Matrix was applied using a robotic sprayer – M5 Sprayer equipped with a sample heating tray (HTX Technologies, LLC, Chapel Hill, NC, USA). Specific matrix and salt deposition parameters for sample preparation experiments are listed in **Table 3.1**. For ganglioside standard analysis, GD1a and GD1b ganglioside extracts (powder) were dissolved in chloroform, aliquoted in vials, dried down with nitrogen, and re-dissolved in 80% methanol for a final extract concentration of 2 mg/mL. The total porcine ganglioside extract had a final concentration of 10 mg/mL. The mixtures were spotted on an ITO-coated glass slides and sprayed with matrix.

Table 3.1. Matrix Deposition Parameters

	Concentration (mg/mL), Solvent	**Nozzle temperature**	**Velocity (m/min)**	**Passes (#)**	**Spray Speed (mL/min), Pressure (psi)**	**Matrix density (µg/mm^2)**
DHA	5.0, 60% Ethanol	60 ºC	1350	5	0.05, 10 psi	1.48
DHB	40, 100% THF	40 ºC	1350	4	0.1, 8 psi	3.95
9AA	15, 100% THF	40 ºC	4050	4	0.15,	7.65
DAN	15, 100% THF	30 ºC	4050	4	0.15,	7.65
ACA	15, 95% THF, 5% DMF	50 ºC	4050	4	0.15, 8 psi	7.65
AmF	62.5 mM, 60% Ethanol	65 ºC	1350	25	0.01, 15 psi	1.48
AmS	62.5 mM, 60% Ethanol	65 ºC	1350	25	0.01, 15 psi	1.48

Nozzle height (40 mm), spacing (1.5 mm), gas flow rate (2 L/min), drying time (2 sec), and stage temperature (55ºC) were kept constants for all experiments. DHB was sprayed at 8 psi.

MALDI TIMS IMS

All experiments were carried out on a prototype MALDI timsTOF Pro mass spectrometer. The $1/K_0$ range, EFG scan time and rate, *m/z* range, and other specific imaging parameters are listed in **Table 3.2**. For standard analysis, data were acquired at 20 µm spatial resolution with ~60 % laser power at 10 kHz, 200 shots per pixel, and ~300 pixels per sample. MALDI TIMS IMS specific data are listed in **Tables 3.3**

Table 3.2. TIMS Parameters for Ganglioside Standards, Rat Brain, and Rat Spinal Cord Tissue Sections

Dataset	t_{ramp} (ms)	$1/K_0$ ($V \cdot s/cm^2$)	V_{ramp} (V)	Sr ($V \cdot ms^{-1}$)
Standard Analysis	1100	2.11 – 2.17	0.06	<0.01
Rat Brain	550	2.05 – 2.17	0.12	0.03
Rat Spinal Cord	1100	2.11 – 2.17	0.06	<0.01

The following parameters were kept constant across all imaging experiments: ESI dry gas temperature – 100ºC; Ion transfer time - 120 µs; pre-pulse storage time - 12 µs; collision RF - 3500 Vpp; TIMS funnel 1 RF - 450 Vpp; TIMS funnel 2 RF - 400 Vpp; multipole RF - 400 Vpp, collision cell entrance voltage - -200 V; MALDI deflection plate -90 V. The source pressure was set ~ 2.35 mBar, to access higher $1/K_0$ ranges.

Table 3.3. MALDI IMS Parameters of the Acquired Data Sets

Dataset	*m/z*	Beam Scan (µm)	Spatial resolution (Pitch)	Laser Power (%)	Shots per pixel (#)
Standards	1000-3000	45	50	80	250
Rat Brain	1000-3000	14	20	80	350
Rat Spinal Cord	1000-3000	15	20	35	250

Histology, Microscopy & Tissue Annotation

Following MALDI IMS experiments, matrix was removed from samples, and tissues were stained using a modified cresyl violet stain in the following sequence: 70% Ethanol (30 sec), 0.05% Cresyl violet (1.5 min), Water (30 sec), Hematoxylin (15 sec), 70% Ethanol (30 sec), 95% Ethanol (30 sec), Xylene (30 sec).[141] Brightfield microscopy of stained tissues was obtained using a Zeiss AxioScan Z1 slide scanner (Carl Zeiss Microscopy GmbH, Oberkochen, Germany). Annotations of anatomical regions were made with the help of *The Allen Mouse Brain Atlas*[142,143], *The Rat Brain in Stereotaxic Coordinates*[144], and *The Atlas of Rat Spinal Cord*[145]. Immunofluorescence was also performed to verify the localization of GD1a in rat brain and spinal cord tissue sections (data not shown).

Identifications & Data Processing

Serial tissue sections were analyzed for further structural investigation. To eliminate the possibility of isobaric interferences, a tissue section was analyzed using ultrahigh- mass-spectral resolution FT-ICR MS (resolving power ~200,000 at *m/z* 1544). MALDI TIMS MS/MS was used to show diagnostic and preferential a- and b-series fragments from standards, and to confirm ganglioside identification from serial tissue section. MALDI TIMS IMS data were analyzed using DataAnalysis and visualized using SCiLS and a custom in-house developed software.

CHAPTER IV

RESOLVING GANGLIOSIDE HETEROGENEITY WITHIN MURINE *STAPHYLOCOCCUS AUREUS* ABSCESSES

OVERVIEW

Gangliosides are known to have important roles in innate and adaptive immunity.[76] Their high degree of structural heterogeneity results in significant variability in ganglioside expression patterns and greatly complicates linking structure and function. Structural characterization at the site of infection is essential in elucidating host ganglioside function in response to invading pathogens such as *Staphylococcus aureus* (*S. aureus*). Here, ganglioside structural and spatial heterogeneity within a *S. aureus*-infected mouse kidney abscess was characterized using MALDI TIMS IMS. Differences in spatial distributions were observed for gangliosides of different classes as well as for gangliosides that differ in ceramide chain composition and oligosaccharide-bound sialic acid. Furthermore, integration of TIMS allowed for the gas-phase separation of monosialylated ganglioside isomers with different spatial distributions within the host-pathogen interface. A decrease in GM1b-GM1a isomer ratio from 4 to 10 days-post-infection was observed and ganglioside analysis within the abscess revealed new molecular layers, unidentified by traditional histology. This work shows that MALDI TIMS IMS can be used to survey the molecular diversity within the infected abscess and at the host-pathogen interface.

INTRODUCTION

S. aureus is a widespread commensal gram-positive bacterium and pathogen.[146–148] It is the leading cause of skin and soft tissue infections that can result in more serious infections, including bacteremia, pneumonia, and osteomyelitis.[149] Staphylococcal invasion typically involves soft-tissue abscess formation, where the bacteria organize into staphylococcal abscess communities, surrounded by severe inflammation of neighboring tissues.[97,98,149] The mature abscess, as described in Chapter I, is a highly heterogeneous environment with a diverse subset of host- and pathogen-derived molecules. Spatial investigation of the soft-tissue abscess is possible through traditional histological approaches to characterize the abscess and its anatomical subregions. Other techniques, including IHC, can be employed to expose the spatial distributions of specific targets within the tissues. However, molecular information cannot be gleaned from these techniques, and more advanced analytical approaches, such as MALDI IMS, are necessary to provide molecular and spatial context. Correlating histology and IMS can allow for thorough investigation of the molecular drivers behind the *S. aureus* infections. For example, gangliosides are known to be involved in host-pathogen interactions, however their structural differences, abundance, and spatial distributions within infection lesions remain to be explored. [76,78,150,151]

Gangliosides are known immune system modulators that can alter both innate and adaptive immune functions.[77,150] They reside primarily in the cellular plasma membrane, where the ceramide anchors the molecule to the membrane and the glycan protrudes outward from the cell. At the cell surface, gangliosides interact with other molecules, such as glycosphingolipids, via hydrogen bonds and van der Waal's forces to form lipid rafts.[78] Here, gangliosides can regulate the activity of proteins via protein-carbohydrate and carbohydrate-carbohydrate interactions.[150–152] Gangliosides can also be used as unintentional targets for microbial adhesion, where viruses,

bacteria, and bacterial toxins bind to the carbohydrate of gangliosides on host cell surfaces.[78,150] For example, epithelial cells expressing GM1 were found to bind Cholera toxin B and *Escherichia coli* enterotoxin, and recognize *Brucella suis* bacteria.[77,150] Elucidating the distinct functions of gangliosides in response to invading pathogens is particularly challenging due to their vast structural diversity.[150] Thus, comprehensive structural information at the site of infection is a critical first step in exploring ganglioside function in the immune system.

Structurally, the ganglioside molecule can be divided into two functional units – a hydrophilic oligosaccharide headgroup carrying sialic acid(s) and a hydrophobic ceramide moiety. (**Figure 4.1A**).[81,83] The ceramide moiety of the gangliosides is composed of a sphingosine and a fatty acyl chain (**Figure 4.1B**). The fatty acyls in gangliosides are generally long, ranging from 16 to 30 carbons, with varying degrees of unsaturation. The sphingoid base, also referred to as the long-chain base, can vary in carbon-chain length, number of double bonds, and number of hydroxyl groups. The most common sphingoid bases are d18:1 and d20:1, where 18 and 20 refer to the number of carbons in the chain, 1 to the presence of a single double bond, and *d* ('di' - two)

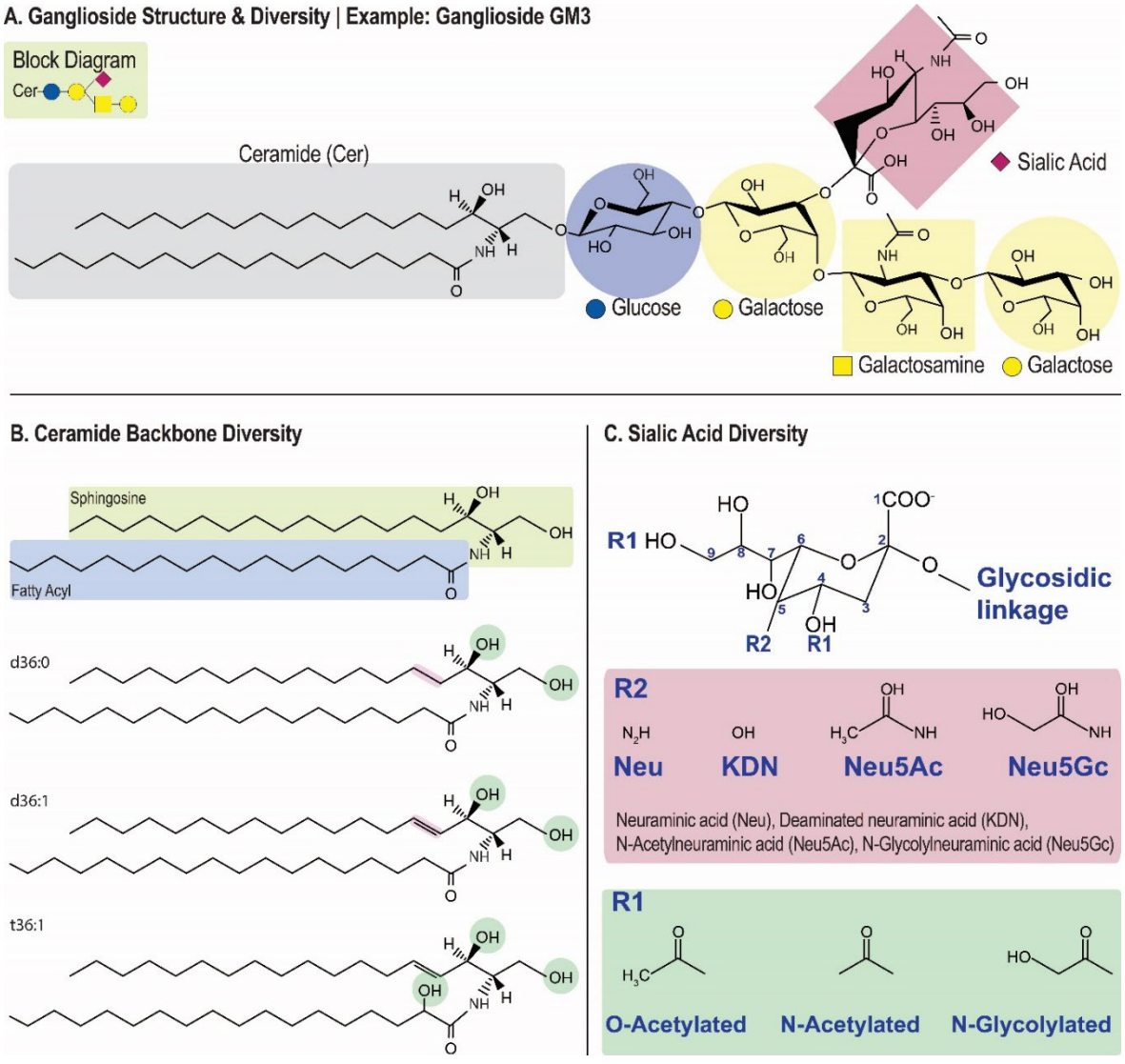

Figure 4.1. Ganglioside Molecular structure – GM3 example **(A)** highlights common diversities in the Ceramide backbone **(B)** and common sialic acids and their alterations **(C)**.

to number of hydroxyl groups on the sphingoid base. Other sphingoid bases present in eukaryotes include d18:0, d20:0, d16:0, and t18:1 (*'tri'*). Both hydrocarbon length and number of double bonds of the ceramide can dictate biological relevance. Diversity in both the ceramide and the glycan can greatly influence membrane fluidity, as well as the cell-cell interactions that take place in the extracellular space. Membrane fluidity can determine the three-dimensional environment of lipid rafts, ultimately influencing protein-protein interactions.[77]

The hydrophilic oligosaccharide headgroup is comprised of multiple saccharide units, including glucose (Glc), galactose (Gal), galactosamine (GalNac), and sialic acids (**Chapter I, Figure 1.5**).[81] Gangliosides are synthesized by the stepwise addition of monosaccharides to the glucose-ceramide (GlcCer) unit. After the addition of Gal, the LacCer serves as a building block for all remaining gangliosides and is a branching point in the synthesis. From there, the oligosaccharide chain can be elongated by the addition of monosaccharides, creating o-series gangliosides (GA2, GA1, GM1b). On the other hand, the sequential addition of sialic acids to LacCer by sialyltransferases form gangliosides GM3, GD3, GT3, etc. Each of these serve as a precursor for more complex gangliosides, belonging to the a-, b-, and c-series, respectively. The letter refers to the number of sialic acids bound to the internal galactose unit, resulting in o-(zero), a-(one), b-(two), c-(three) series gangliosides. The differences in the oligosaccharide chain and the number/position of sialic acids greatly increase the number of possible structures and their biological roles.

Lastly, negatively charged sialic acids are essential components of the ganglioside molecule. They alone can influence ganglioside function, particularly in pathogen recognition and cell infiltration.[153,154] While all sialic acids share the same 9-carbon carboxylated sugar, there are numerous structural differences and modifications that can be present. The most common ganglioside-bound sialic acids are *N*-acetylneuraminic acid (Neu5Ac) and *N*-glycolyneuraminic acid (Neu5Gc) (**Figure 4.1C**).[133] Although Neu5Gc is abundant in many mammals, a human-specific genetic mutation eliminated our capacity to produce it. Despite this, Neu5Gc has been detected in human carcinomas and fetal tissues.[89] Common modifications of gangliosides include O-acetylation, N-acetylation, and N-glycolylation, and are highlighted in **Figure 4.1C**. Thus, the diversity of sialic acid structures at various sialylation sites increases the possible structures. For example, considering known diversity of the ceramide and the glycan headgroup, it is hypothesized that over 3000 unique gangliosides can exist. [121]

Due to the significant differences in physiochemical properties of the glycan and lipid moieties, analysis of these molecules is challenging, as methods are optimized for each portion and seldom work well for intact analysis. Although not without its limitations, MALDI IMS has been at the forefront of ganglioside analysis. Advances in sample preparation strategies described herein (**Chapter III**) improve in-tact ganglioside analysis by increasing analyte sensitivity and reducing in-source fragmentation of the polysialylated species. Furthermore, the integration of an orthogonal separation technique, such as TIMS, can effectively address ganglioside heterogeneity and isomerism prevalent in this molecular class.

Here, MALDI TIMS IMS of *S. aureus*-infected mouse kidney was used for in-depth structural characterization of gangliosides within the inflammatory lesion. The structural heterogeneity of gangliosides including species with different ceramide composition, oligosaccharide chain, as well as sialic-acid position were detected. Furthermore, ganglioside isomers were resolved by TIMS-separations and their distinct localization to different abscess subregions were determined. The increased specificity allowed for spatial investigation of ganglioside isomers over the course of infection.

RESULTS AND DISCUSSION

Ganglioside Ceramide, Glycan, and Sialic Acid Diversity within a Murine Kidney *S. aureus*- soft tissue abscesses

To investigate ganglioside heterogeneity at the host-pathogen interface, a 10 day-post-infection (dpi) mouse kidney tissue section was analyzed using MALDI TIMS IMS. An H&E microscopy image of the infected tissue (**Figure 4.2**) was annotated to highlight observable, known abscess subregions. Histopathological assessment of the tissue revealed features of the intra-abscess morphology. The bacterial SACs were identified at the center of the abscess (red arrows). The primary immune cells observed in the abscess were neutrophils, with degranulated neutrophils (puss) found in closer proximity to the bacterial colonies, and a mixture of degenerate and viable immune cells found further from the abscess center (yellow arrow). The intensely eosinophilic material (blue boundary) was tentatively identified as the Splendore-Hoeppli phenomenon.[155–157] Lastly, the microscopy revealed a dark-stained fibrous capsule layer at the outer abscess region (green arrow) separating the abscess from the healthy host tissue. MALDI TIMS IMS of the tissue section revealed numerous ganglioside species whose heterogeneity was categorized based on ceramide and oligosaccharide chain composition, as well as sialic acid composition and position. Lastly, TIMS separation of o- and a-series ganglioside isomer species was demonstrated. Trends in the spatial distributions of the detected ganglioside were explored. **Table 4.1** lists all detected ganglioside species identified by high mass accuracy FT-ICR data and on-tissue MALDI TIMS MS/MS.

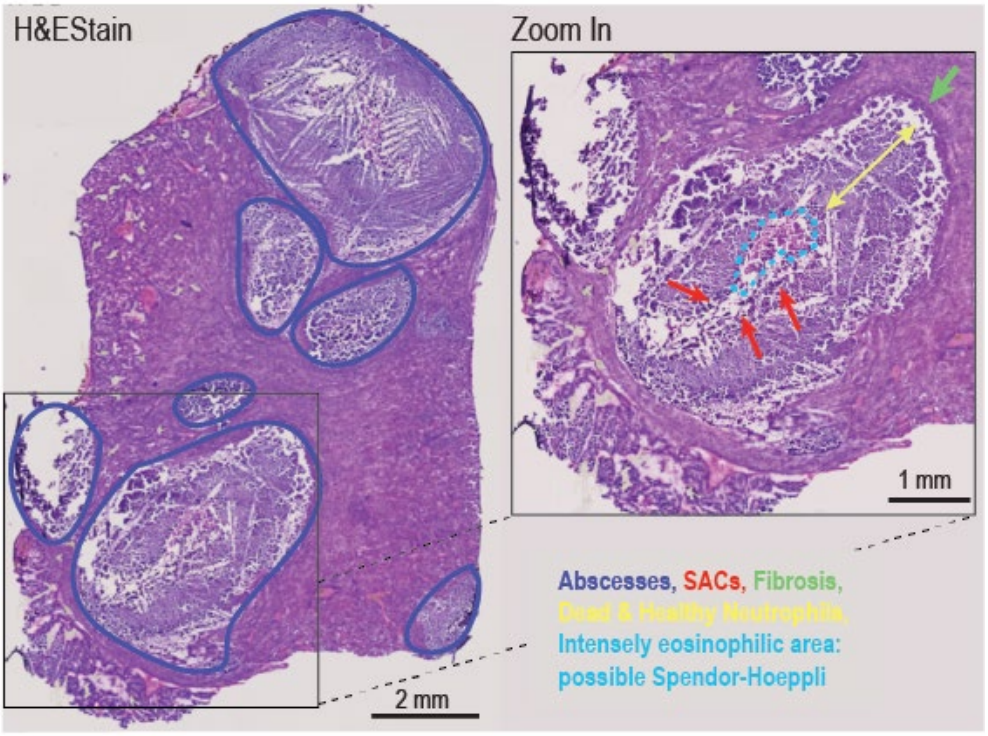

Figure 4.2. Hematoxylin & Eosin Stain of 10 dpi *S. aureus* infected mouse kidney section reveals several abscess lesions (blue boundaries) within the kidney section. A zoom in of the lesion reveals a dark stained fibrous capsule (green), bacterial staphylococcal abscess communities (red arrows), a zone of healthy/dead immune cells, as well as an intensely eosinophilic region, tentatively identified as Splendore-Hoeppi (bright blue).

Table 4.1. Ganglioside species identified by class. Sialic acid composition included in ganglioside name if known. *Denotes potential isomer that are not identified.

Table 4.1.1 GM3 Gangliosides Identified in a 10 Days Post Infection Mouse Kidney Section

Ganglioside	Full Name	*m/z*
GM3 	Neu5Ac GM3 (d34:1)	1151.706
	Neu5Gc GM3 (d34:1)	1167.701
	Neu5Gc GM3 (t34:1)	1183.696
	Neu5Gc GM3 (d38:1)	1223.763
	Neu5Ac GM3 (d40:1)	1235.800
	Neu5Gc GM3 (d40:1)	1251.795
	Neu5Ac GM3 (d42:2)	1261.815
	Neu5Ac GM3 (d42:1)	1263.831
	Neu5Gc GM3 (d42:3)	1275.795
	Neu5Gc GM3 (d42:2)	1277.810
	Neu5Gc GM3 (d42:1)	1279.826

Table 4.1.2 GM2 Gangliosides Identified in a 10 Days Post Infection Mouse Kidney Section

Ganglioside	Full Name	*m/z*
GM2 	Neu5Gc GM2 (d34:1)	1370.780
	Neu5Gc GM2 (d36:1)	1398.811
	Neu5Gc GM2 (d40:1)	1454.874
	Neu5Gc GM2 (d42:2)	1480.890
	Neu5Gc GM2 (d42:1)	1482.905

Table 4.1.3 GM1 Gangliosides Identified in a 10 Days Post Infection Mouse Kidney Section

Ganglioside	Full Name	*m/z*
GM1 	Neu5Ac GM1 (d34:1)	1516.838
	Neu5Ac GM1 (d34:0)	1518.854
	Neu5Gc GM1 (d34:1)	1532.833
	Neu5Ac GM1 (t34:1)	1532.833
	Neu5Ac GM1 (d36:1)	1544.864
	Neu5Gc GM1 (d36:1)	1560.864
	Neu5Ac GM1 (t36:1)	1560.864
	Neu5Ac GM1 (t38:1)	1588.896
	Neu5Gc GM1 (d38:1)	1588.896
	Neu5Ac GM1 (t38:0)	1590.911
	Neu5Ac GM1 (d40:1)	1600.932
	Neu5Ac GM1 (d40:0)	1602.948
	Neu5Gc GM1 (d40:1)	1616.927
	Neu5Ac GM1 (t40:1)	1616.927
	Neu5Ac GM1 (t40:0)	1618.943
	Neu5Ac GM1 (d42:3)	1624.932
	Neu5Ac GM1 (d42:2)	1626.948
	Neu5Ac GM1 (d42:1)	1628.963
	Neu5Gc GM1 (t42:3)	1640.927
	Neu5Gc GM1 (d42:2)	1642.943
	Neu5Ac GM1 (t42:2)	1642.943
	Neu5Gc GM1 (d42:1)	1644.958
	Neu5Ac GM1 (t42:1)	1644.958

Table 4.1.4 GalNAc-GM1b and extended series GM1b Gangliosides Identified in a 10 Days Post Infection Mouse Kidney Section

Ganglioside	Full Name	*m/z*
GalNAc-GM1b 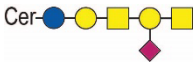	Neu5Ac GalNAc-GM1b (d34:1)	1719.917
	Neu5Ac GalNAc-GM1b (d34:0)	1721.933
	GalNAc-GM1b (34:1) *	1735.912
	GalNAc-GM1b (34:0)*	1737.928
	GalNAc-GM1b (36:1)*	1763.944
	Neu5Ac GalNAc-GM1b (d40:1)	1804.011
	Neu5Ac GalNAc-GM1b (d40:0)	1806.027
	GalNAc-GM1b (40:1)*	1820.006
	GalNAc-GM1b (40:0)*	1822.022
	Neu5Ac GalNAc-GM1b (d42:2)	1830.027
	Neu5Ac GalNAc-GM1b (d32:1)	1832.043
	GalNAc-GM1b (42:3)*	1844.006
	GalNAc-GM1b (42:2)*	1846.022
	GalNAc-GM1b (42:1)*	1848.038
	Neu5Gc GalNAc-GM1b (t42:2)	1862.017
	Neu5Gc GalNAc-GM1b (t42:1)	1864.032
Extended GM1b 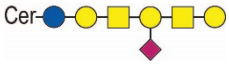	Ext. GM1b Neu5Ac (d42:1)	1994.0.95
	Ext. GM1b Neu5Gc (42:2)*	2010.090
	Ext. GM1b Neu5Ac (d42:2)	1992.080

Table 4.1.5 GD1 Gangliosides Identified in a 10 Days Post Infection Mouse Kidney Section

Ganglioside	Full Name	*m/z*
GD1 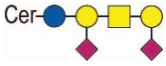	GD1 (Neu5Ac - Neu5Ac) (d34:1)	1807.933
	GD1 (34:1)*	1823.928
	GD1 (34:1)*	1839.923
	GD1 (38:1)*	1879.991
	GD1 (40:1)*	1908.022
	GD1 (Neu5Gc - Neu5Gc) (d40:1)	1924.017
	GD1 (42:3)*	1932.022
	GD1 (42:2)*	1934.038
	GD1 (42:1)*	1936.054
	GD1 (Neu5Gc - Neu5Gc) (t42:1)	1940.012
	GD1 (42:2)	1950.033
	GD1 (42:1)	1952.049

Six different classes of gangliosides, including monosialylated (GM1, GM2, and GM3) as well as disialylated (GD1) were detected within the *S. aureus*-infected mouse kidney section **(Figure 4.3)**. Rare GalNac-GM1b and extended series-GM1b ganglioside species were also observed in the infection model. These ganglioside species have only been observed in a few immune cell types, including T-cells, B-Cells, and Macrophages,[152,158,159] however, their abundance in other immune cells has not been demonstrated. Of the ganglioside classes, the most numerous and highest intensity gangliosides were GM1s.

GM3 species are the simplest a-series gangliosides, composed of two carbohydrate units and a single sialic acid. A total of 11 GM3 species were detected in the infected kidney, where the ceramide chains ranged from C34 to C42 in length (**Table 4.1.1** & **Figure 4.3A**). Mono-unsaturated di-dehydroxylated ceramide chains were most common, and no unsaturated species were detected. In terms of sialic acid diversity, both Neu5Ac and Neu5Gc sialic acids were detected. GM3 species were the only ganglioside species observed in both the control and infected tissue. For example, *m/z* 1151.71, identified as Neu5Ac GM3(d34:1), localized to the fibrous

capsule of the abscess and the glomeruli (kidney filtering units). This ion was also detected in the non-infected kidney glomeruli. Here, GM3s are highly abundant in the glomerular podocytes, where they aid in maintaining the functional integrity of the filtration barrier.[160] In the infected kidney, all GM3s localized to the fibrous capsule and were not detected in the intra-abscess region.

GM2s are synthesized from GM3s with the addition of GalNac to the oligosaccharide chain to form a tri-saccharide headgroup with a single sialic acid residue. A total of five GM2 species were detected in the infected tissues sample. (**Table 4.1.2** & **Figure 4.3B**) All GM2s had a di-hydroxylated ceramide backbone, and only Neu5Gc sialic acids were detected. All GM2s were localized to the outer abscess layer, and signals were also observed neighboring the center of the abscess – likely Splendore-Hoeppli phenomenon. The exact role of GM2s within infection processes are not completely understood. It has been noted, however, that in some infection models, GM2s serve as an adhesion molecule for bacterial infiltration.[76]

The most abundant ganglioside class detected in the infected mouse kidney sample was GM1, which contain a tetra-saccharide core and a single sialic acid. GM1s have high structural diversity resulting in several possible isomeric structures (discussed in detail in the following section). In this study, 17 different GM1s were differentiated by *m/z* alone, and additional 8 were revealed by TIMS separation (**Table 4.1.3 & Figure 4.3C**). The ceramide chains varied in length (C34 to C42) and in degree of saturation (unsaturated, di- and tri-unsaturated). Although di-hydroxylated ceramides were most common, several tri-hydroxylated chains were also detected. The GM1s were detected throughout the abscess but varied in their intra-abscess distributions. In addition to the intra-abscess regions, ganglioside signal was also detected in surrounding immune cell infiltrates. The differences in spatial distributions within this ganglioside class can also be attributed to the presence of isomers, as discussed in detail below.

Complex o-series gangliosides, such as GalNac-GM1b, and extended series GM1b species are synthesized from GM1b gangliosides by the sequential addition of GalNac, and Gal-GalNac,

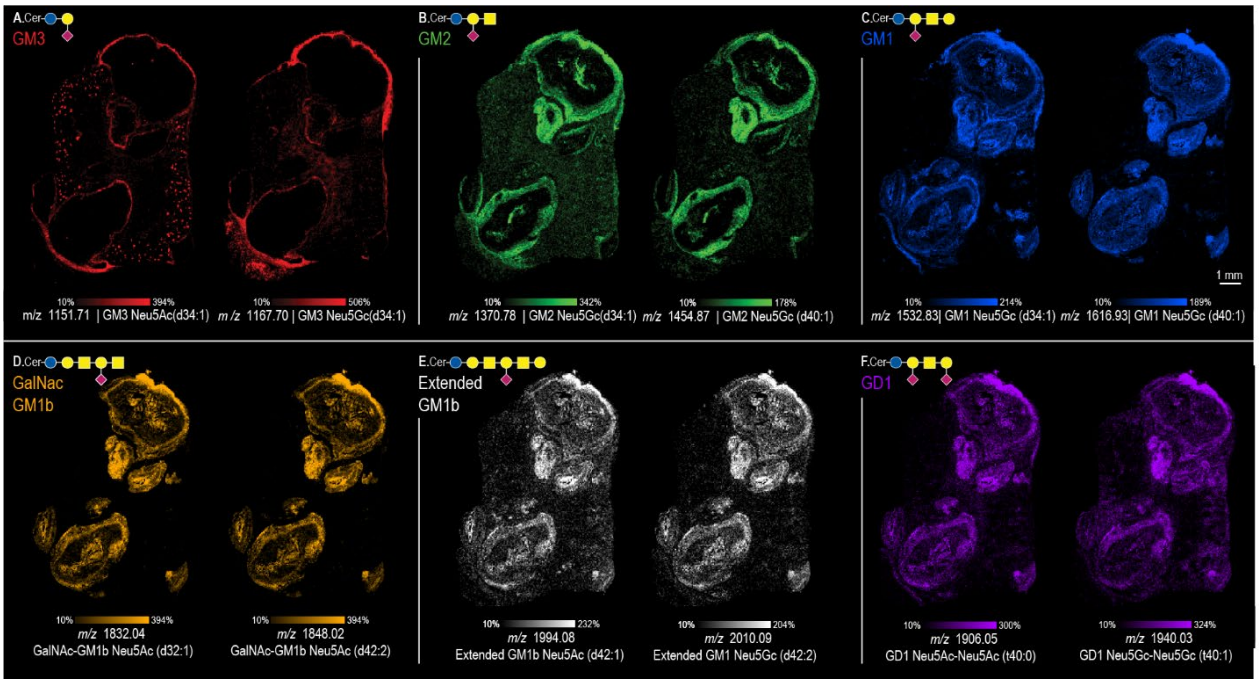

Figure 4.3. MALDI TIMS IMS shows structural and spatial diversity within a 10 days post infection *S.aureus*-infected mouse kidney section across ganglioside classes – GM3 (red), GM2 (green), GM1 (blue), GalNac-GM1b (orange), extended GM1b (white), and GD1 (purple).

respectively. These species may include diversity in sialic acid composition, but not in the position of the sialic acid. In the infected kidney section, 16 different GalNac-GM1b and three extended series GM1b gangliosides were detected (**Table 4.1.4**). Ion images of these molecules varied in intra-abscess spatial distributions, as seen in (**Figure 4.3D & 4.3E**). Little is known about the biological function of extended series gangliosides. They have been reported as part of T-cells, where they have been linked to T-cell differentiation and activation.[130,150,152] However, our results indicate that they may also be crucial components of other immune cells since infection would primarily activate innate immune cells like neutrophils and macrophages. More extended series and GalNac-GM1b gangliosides are likely present in the dataset, however, close isobaric overlap with GD1 species hinders confident identification with MALDI TIMS MS/MS.

GD1s are disialylated gangliosides comprised of a tetrasaccharide carbohydrate chain with two sialic acids. GD1s can be either a-, b-, or c-series ganglioside, and can have multiple variations on each sialic acid. Numerous GD1 species, as highlighted in **Table 4.1.5**, were detected in the *S. aureus*-infected mouse kidney (**Figure 4.3F**). However, polysialylated species, such as GD1, can be particularly challenging to analyze due to the significant in-source fragmentation of the labile sialic-acid bond, as well as the high number of possible isomeric structures. Although sample preparation strategies, discussed in Chapter III, aided *in situ* ganglioside analysis, confident identification of all high-mass GD1s could not be achieved.

Ganglioside Isomers

Monosialylated GM1 species can be synthesized through either a- or o- pathways, resulting in GM1s with different sialic acid binding positions. GM1a has a single sialic acid on the internal galactose unit, and GM1b (o-series) has a single sialic acid on the terminal galactose unit. Sialic acid diversity is also prevalent in GM1s, where both Neu5Ac and Neu5Gc are common in mammalian non-neuronal cells. This structural diversity can result in two types of ganglioside isomers – GM1a and GM1b, Neu5Ac-tCer and Neu5Gc-dCer, and a combination of both. Here, MALDI TIMS IMS was used to analyze GM1 isomers in the *S. aureus* infected tissue section. Identified GM1a and GM1b, and Neu5Ac-tCer and Neu5Gc-dCer ganglioside isomers are listed in **Table 4.2.1** and **Table 4.2.2**, respectively.

Table 4.2.1 GM1a and GM1b Ganglioside Isomers Identified in a 10 Days Post Infection Mouse Kidney Section

Ganglioside	Full Name	*m/z*
GM1a and GM1b 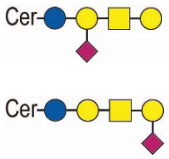	Neu5Ac GM1 (d34:1)	1516.838
	Neu5Ac GM1 (d36:1)	1544.864
	Neu5Ac GM1 (d40:1)	1600.932
	Neu5Ac GM1 (d40:0)	1602.948
	Neu5Ac GM1 (d42:3)	1624.932
	Neu5Ac GM1 (d42:2)	1626.948
	Neu5Ac GM1 (d42:1)	1628.963

Table 4.2.2 Neu5Ac-tCer and Neu5Gc-dCer Ganglioside Isomers Identified in a 10 Days Post Infection Mouse Kidney Section

Ganglioside	Full Name	*m/z*
GM1 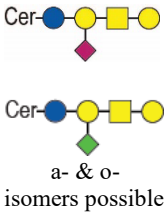 a- & o- isomers possible	Neu5Gc GM1 (d34:1) | Neu5Ac GM1 (t34:1)	1532.833
	Neu5Gc GM1 (d36:1) | Neu5Ac GM1 (t36:1)	1560.864
	Neu5Ac GM1 (t38:1) | Neu5Gc GM1 (d38:1)	1588.896
	Neu5Gc GM1 (d40:1) | Neu5Ac GM1 (t40:1)	1616.927
	Neu5Gc GM1 (d40:0) | Neu5Ac GM1 (t40:0)	1618.943
	Neu5Gc GM1 (d42:3) | Neu5Ac GM1 (t42:3)	1640.927
	Neu5Gc GM1 (d42:2) | Neu5Ac GM1 (t42:2)	1642.943
	Neu5Gc GM1 (d42:1) | Neu5Ac GM1 (t42:1)	1644.958

GM1 a and GM1b Isomers

MALDI TIMS revealed GM1 species with multiple conformations having a single *m/z* value (**Table 4.2.1)**, with examples shown in **Figure 4.4**. Here, the extracted ion mobilograms of *m/z* 1516.843 (Neu5Ac GM1 (d34:1)) and *m/z* 1626.948 (Neu5Ac GM1 (d42:2)) revealed two partially resolved ions (**Figure 4.4A and 4.4B)**. To illustrate the unique spatial distributions of each isomeric species, both the *m/z* and $1/K_0$ information were used to generate ion images. Each panel highlights the distinct spatial distributions of the lower mobility ion in red, the higher mobility ion in blue, and an overlay of both ion images. In both examples, the lower mobility ions localized to the internal regions of the abscess whereas the higher mobility ions localized to the external boundary of the abscess. Subsequent on-tissue MALDI TIMS MS/MS collected from a serial tissue section was used to identify the isomers. Example fragmentation data is shown for *m/z* 1626.948 (**Figure 4.5**). Here, the shared fragmentation pathway for both isomers confirmed the ganglioside class as GM1 and the ceramide chain as d42:2 (**Figure 4.5A**). GM1b and GM1a isomers were additionally confirmed by their preferential/unique fragments, highlighted in **Figure 4.5B** and **4.5C**, respectively. The extracted ion mobilograms of the fragment ions were used to link each isomer to its corresponding mobility range of the parent ion. It was concluded that the lower mobility ion was GM1b, and the higher - GM1a.

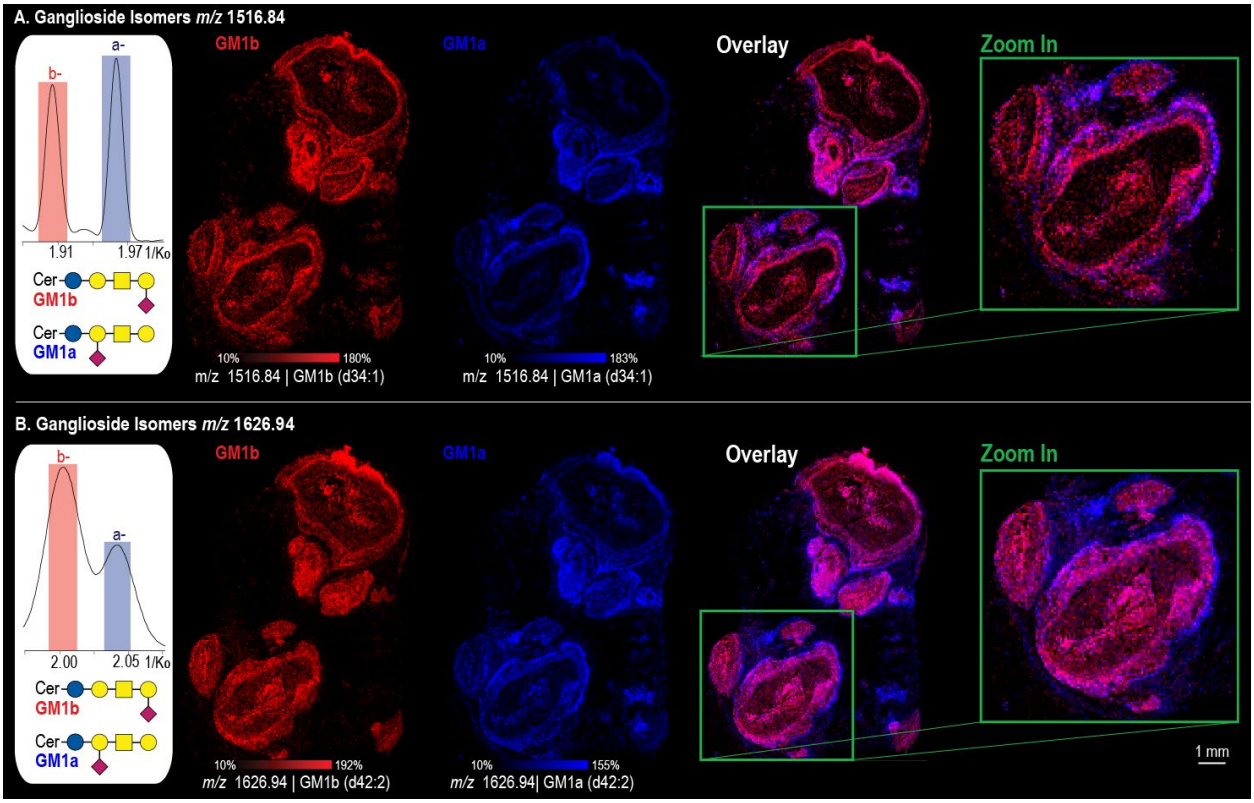

Figure 4.4. Extracted ion mobilograms of *m/z* 1516.84, GM1 (d34:1) **(A)** and *m/z* 1626.94, GM1 (d42:2) **(B)** revealed the TIMS separation of GM1b (red) and GM1a (blue) isomers in *S.aureus*-infected mouse kidney section.

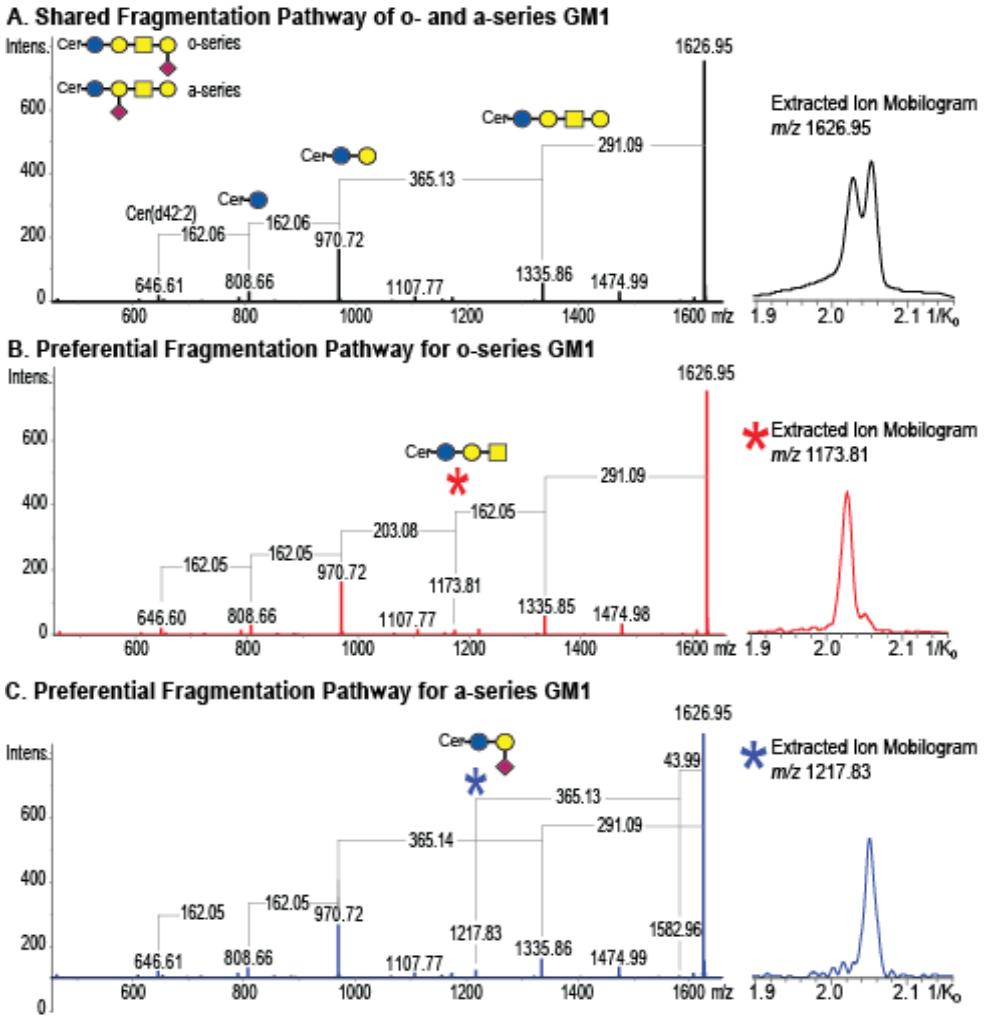

Figure 4.5. On-tissue MALDI TIMS MS/MS of *m/z* 1626.95 **(A)** revealed the presence of both GM1a **(B)** and GM1b **(C)** isomers within a 10 days post infection *S.aureus*-infected mouse kidney. The Extracted ion mobilograms of unique/preferential fragments (right panels) confirmed that GM1b (red) is more compact than GM1a (blue)

Neu5Ac-tCer and Neu5Gc-dCer Ganglioside Isomers

Neu5Ac-tCer and Neu5Gc-dCer GM1 isomers arise when a Neu5Gc-containing GM1 with a di-hydroxylated ceramide chain overlaps with a Neu5AC sialic acid with a tri-hydroxylated ceramide chain. **Table 4.2** summarizes the possible Neu5GC-dCer and Neu5Ac-tCer isomers within the dataset. **Figure 4.6** highlights GM1 Neu5Gc (d34:1) and GM1 Neu5Ac (t34:1) detected at *m/z* 1532.83. Additionally, both gangliosides can be either GM1a or GM1b resulting in at least four possible isomers having the same *m/z* value. The extracted ion mobilogram of *m/z* 1532.83 revealed several gas-phase conformers, although not all were baseline resolved. The extracted ion mobilogram of *m/z* 1532.83 revealed five ion mobility peaks – $1/K_0$ 1.91 (red), $1/K_0$ 1.93(1) (pink), $1/K_0$ 1.93(2) (blue), $1/K_0$ 1.97 (gray), and $1/K_0$ 2.00 (green). Each of the *m/z* + $1/K_0$ ion distributions can be seen in the ion images in **Figure 4.6B**. On-tissue MALDI TIMS MS/MS was performed to identify the conformers. The fragmentation spectrum revealed the presence Neu5Ac

GM1 (t34:1) and Neu5Gc GM1 (d34:1), show in **Figure 4.7A** and **4.7B**, respectively. The sialic acid structures were confirmed by the loss of Neu5Ac (- *m/z* 291) and Neu5Gc (- *m/z* 307). The ceramide compositions Cer(t34:1) and Cer(d34:1) were confirmed by fragments at *m/z* 536.49 and *m/z* 553.51, respectively (**Figure 4.7A & 4.7B**). To assign identities of the parent-peak resolved conformers, the extracted ion mobilograms of fragment ions were assessed where applicable. The extracted ion mobilograms of *m/z* 1225.74 and *m/z* 860.56 indicate that GM1 Neu5Gc (d34:1) is associated with peaks $1/K_0$ 1.93(1) (pink) and $1/K_0$ 2.00 (green). The presence of two peaks in the extracted fragment ion mobilogram also indicates the presence of both GM1a and GM1b Neu5Ac (t34:1) isomers. Similarly, the extracted ion mobilograms of *m/z* 1241.70 and *m/z* 876.56 reveal that the peaks at $1/K_0$ 1.91 (red) and $1/K_0$ 1.93(2) (blue) arise from Neu5Ac (t34:1) – both GM1a and GM1b isomers. Lastly, the extracted ion mobilogram of *m/z* 876.56 revealed two additional isomers, likely arising from ceramide chain diversity that could not be identified.

To confidently assign the fragment extracted ion mobilograms as a- and o-series isomers, extracted ion mobilograms of unique (or preferential) fragment ions were generated (**Figure 4.7C & 4.7D**). The fragment at *m/z* 1167.71 was found to be unique for GM1a – both Neu5Gc (d34:1) and Neu5AC (t34:1). This fragment arises from the loss of Gal-GalNAc from the headgroup, while the sialic acid remains intact on the internal Gal unit. The extracted ion mobilogram reveals that Neu5AC (t34:1) is likely the more intense ion. The preferential fragmentation of GM1b isomers include a stepwise loss of a sialic acid, and a Gal unit. For Neu5Ac (t34:1) and Neu5Gc (d34:1), this results in fragment ions *m/z* 1079.67, and *m/z* 1063.69, respectively. From the extracted ion mobilogram of each, two peaks can be seen. The lower mobility peaks are attributed to the b series isomers, however higher-mobility a-series fragmentation was also observed.

Lastly, the MALDI TIMS MS/MS information allowed for the extracted ion mobilogram of *m/z* 1532.83 to be partially annotated. Here, we were able to confirm the presence of four different isomers - Neu5Ac (t34:1) and Neu5Gc (d34:1), both a- and b- of each, and map their distinct spatial distributions (**Figure 4.6**). These findings indicate that the major isomer in the

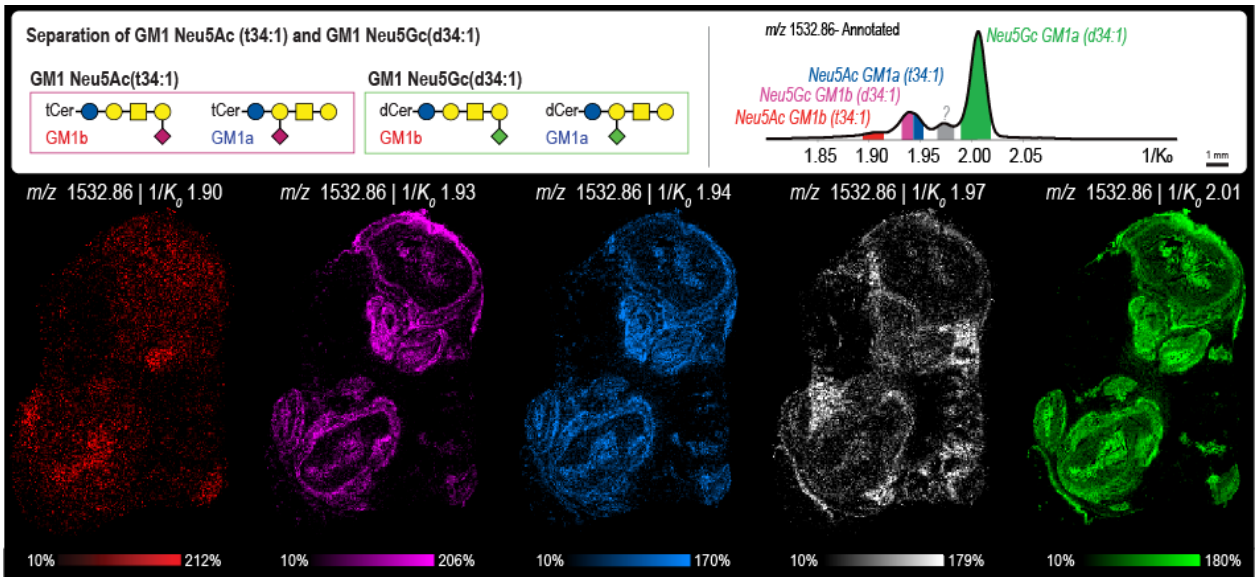

Figure 4.6. Extracted ion mobilogram of *m/z* 1532.86 reveals five partially resolved peaks –$1/K_0$ 1.91 (red), $1/K_0$ 1.93(1) (pink), $1/K_0$ 1.93(2) (blue), $1/K_0$ 1.96 (gray) $1/K_0$ 1.97 (gray), and $1/K_0$ 2.00 (green). Each of the *m/z* + $1/K_0$ ion distributions can be seen in the ion images in the bottom panel. Ions were identified with on-tissue MALDI TIMS MS/MS, as seen in **Figure 4.7**.

mixture is GM1a Neu5AC (t34:1) at $1/K_0$ 2.00. Because of this, the spatial distributions of the ion image without mobility separation would likely be dominated by this isomer.

This level of structural specificity for ganglioside analysis is very important in an imaging context of infections. Isomeric gangliosides are known to be involved in different biological functions.[79] Previous studies have demonstrated the importance of sialic acid position on ganglioside function. For example, gangliosides with a sialic acid on a terminal galactose unit (such as GM1b) have been found to have a much higher immunosuppressive activity.[77,83] Neu5Gc-contsining gangliosides have also been implicated in host-pathogen interactions, however, their functions are not well understood. It has also been postulated that ganglioside patters of immune cells vary significantly throughout the course of an infection.[78,81,161] MALDI TIMS IMS is an ideal tool to investigate the redistribution of gangliosides over time at the host-pathogen interface.

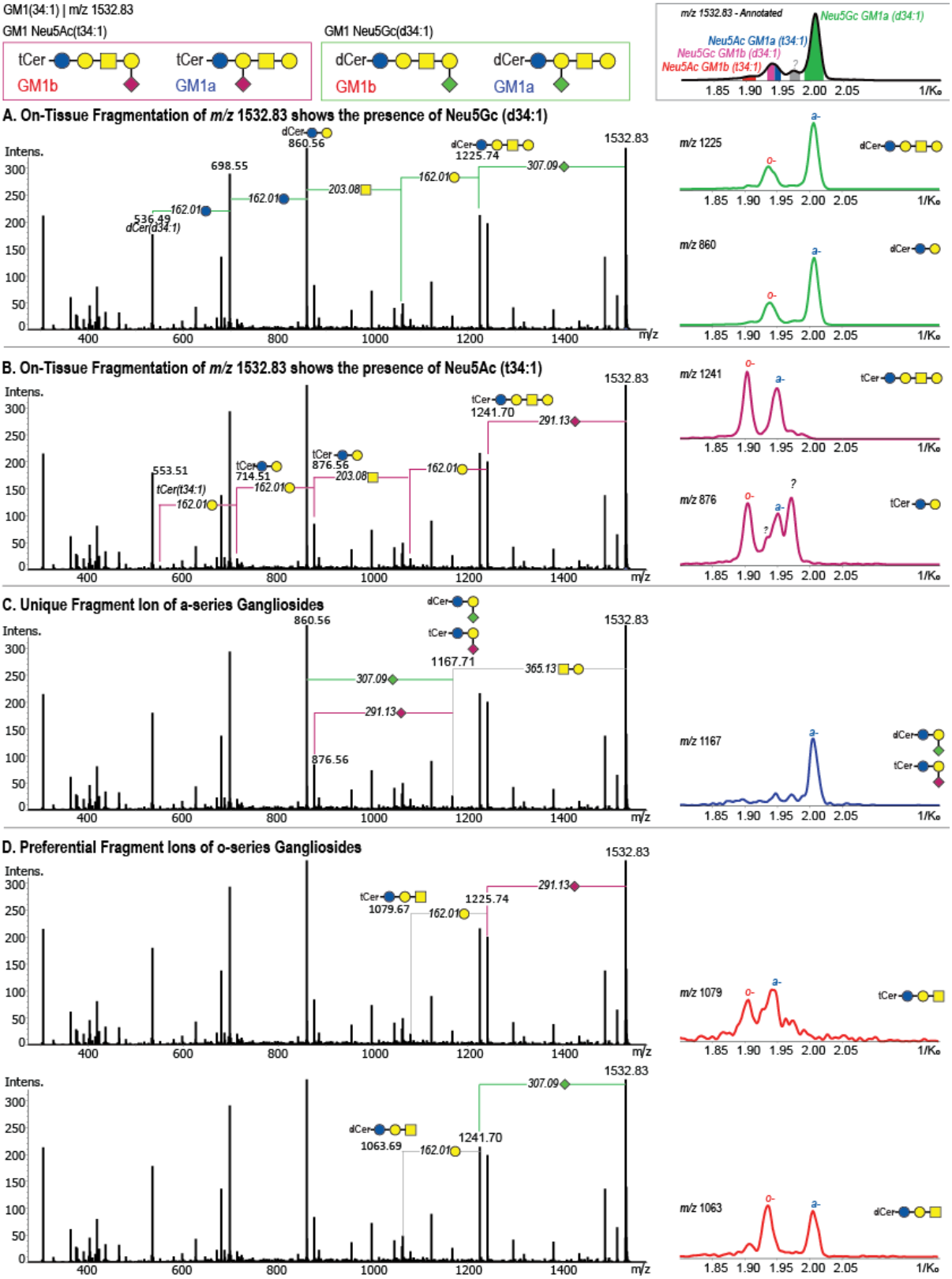

Figure 4.7. On-tissue MALDI TIMS MS/MS of *m/z* 1532.84 reveals the presence of both GM1 Neu5Gc (d34:1) **(A)** and GM1 Neu5Ac (t34:1) **(B)** within a 10 days post infection *S.aureus*-infected mouse kidney. For both GM1 Neu5Gc (d34:1) and GM1 Neu5Ac (t34:1), GM1a and GM1b isomers were also identified, as evidenced by panels **(C)** and **(D)**, respectively. The extracted ion mobilograms of unique/preferential fragments provide identification of the TIMS-resolved ions of the parent peaks.

Temporal alteration of ganglioside isomers – GM1a and GM1b in *S. aureus* soft tissue infection model

The temporal alterations of ganglioside isomers were analyzed throughout the course of the *S. aureus* infection. For this purpose, 4, 6, and 10 dpi mouse kidney tissue samples were analyzed. Data were collected in triplicate with the exception of 10 dpi, which reflects a single data point due to the low survival rate of the infected mice (most succumb to the infection within 6 days). The relative abundance of GM1b and GM1a isomers was tracked by calculating their relative ratio across four GM1 species: *m/z* 1516.84, *m/z* 1600.93, *m/z* 1616.94, and *m/z* 1628.96 (Figure 4.8.). For ions *m/z* 1516.84, *m/z* 1600.93, *m/z* 1616.94, a sharp decrease was observed between 4 and 6 dpi, whereas *m/z* 1628.96 remained unchanged in the initial time points but had a sharp decrease by 10 dpi. Overall, this preliminary case study indicates that the relative ratio of GM1b/GM1a decreases throughout the course of the infection, but future studies are needed to elucidate further.

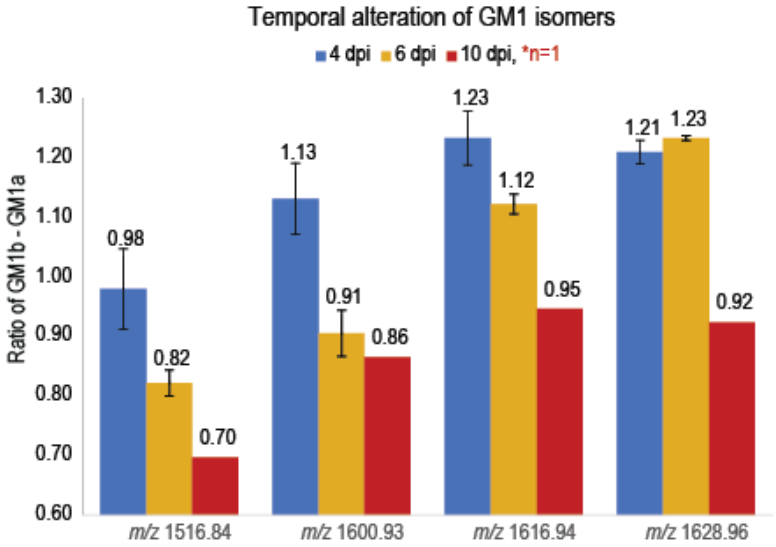

Figure 4.8. Temporal alteration of ganglioside GM1b/GM1a isomer ratio at 4 dpi (blue), 6dpi (orange), and 10 dpi (red) across four GM1 species: Neu5Ac GM1 (d34:1) (*m/z* 1516.84), Neu5Ac GM1 (d40:1) (*m/z* 1600.93), Neu5Gc GM1 (d40:1) (*m/z* 1616.94), and Neu5Ac GM1 (d42:1) (*m/z* 1628.96). dpi = days post infection

A possible explanation for this observation may be linked to macrophage activity. Previous studies have shown monosialylated gangliosides (GM1b in particular) to be major components of stimulated macrophages.[158,159] Their activation has been associated with increased activity of cell membrane sialidases that cleave sialic acids from membrane-bound ganglioside molecules. GM1b is more susceptible to sialidase activity, as the terminal sialic acid is exposed and easily cleaved in comparison to GM1a. As macrophages are activated, the GM1b gangliosides are de-sialylated at significantly higher rates than GM1a. It is postulated that the increased presence of de-sialylated GM1b (GA2) molecules may be responsible for triggering activated macrophages into operation. Although this process is not completely understood, it is clear that the de-sialylation event is critical in macrophage function.[159] The spatiotemporal investigation of ganglioside isomers highlighted herein, suggests that abundance and distribution of GM1b may be a driver of macrophage activation.

MALDI TIMS IMS of Gangliosides Reveal New Molecular Layers Unidentified by Traditional Histology

A stained microscopy image of the infected tissue (**Figure 4.9**) was annotated to highlight some of the subregions of interest, including the fibrous capsule surrounding the abscess (green), a zone of degenerate and healthy innate immune cells (yellow), as well as the bacteria at the center

of the abscess (red arrows). **Figure 4.9** highlights ion images with different localizations within the lesion, where some ions localized specifically to known abscess subregions. For example, bacterial cardiolipin CL (64:0) (pink) was detected at *m/z* 1351.98, revealing the spatial distributions of the bacteria within the abscess. Ion *m/z* 1151.71 (red) co-localized with the outer boundary of the abscess, which was identified by the microscopy as the fibrous capsule. These two ions correlate well with known anatomical features. However, additional ganglioside distributions reveal more intra-abscess heterogeneity than previously described with traditional microscopy. This is evident in the zone of healthy/necrotic immune cells (**Figure 4.9**), where histological assessment revealed a largely homogeneous layer, with no distinct anatomical sub-regions. Here, the ion images reveal several distinct, previously undescribed, distributions within that subregion. For example, *m/z* 1005.51 (yellow) has two distinct molecular layers within the abscess, and ions *m/z* 1370.78 (green) and *m/z* 1532.86 (blue) localize between the yellow subregions. The *m/z* 1532.86 ion also localizes to an extra-abscess region that can tentatively be characterized as immune cell infiltrates.

Lastly, the microscopy revealed an intensely eosinophilic feature near the bacterial colonies tentatively identified as the Splendore-Hoeppli phenomenon.[155] The ion image of *m/z* 1370.78 (green) co-localized to the intensely eosinophilic region, as well as the outer-most zone of necrotic/healthy immune cells. The Splendore-Hoeppli phenomenon can be found peripheral to

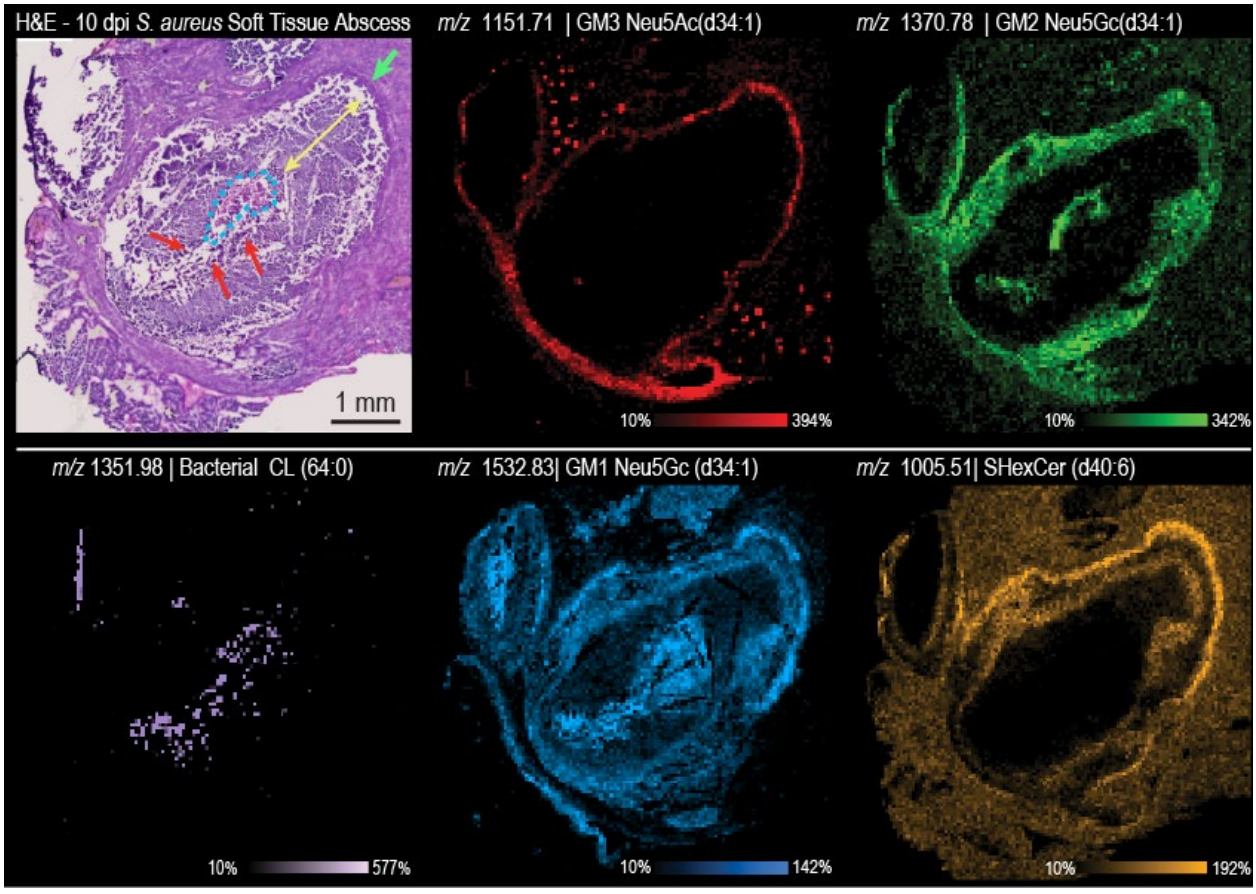

Figure 4.9. H&E stain of soft tissue abscess (10 days post infection *S. aureus* infected mouse kidney) revealing a fibrous capsule (green arrow), bacterial communities (red arrows), a zone of healthy/dead immune cells (yellow arrow), as well as an intensely eosinophilic region tentatively identified as Splendore-Hoeppli asteroid bodies (bright blue). Ion images of *m/z* 1151.71 (red), *m/z* 1370.78 (green), *m/z* 1351.98 (pink), *m/z* 1532.86 (blue), and *m/z* 1005.51 (yellow) highlight the intra-abscess heterogeneity revealed by MALDI TIMS IMS.

bacteria and among areas of degeneration and necrosis.[157] The exact mechanism and molecular makeup of Splendore-Hoeppli asteroid bodies is still unknown, however, it is thought to contain glycoproteins, lipid, and calcium derived from host leukocytes. MALDI TIMS IMS was able to uncover more detailed molecular and morphological information of this and similar phenomena of known anatomical features of the soft tissue abscess than with traditional methods. Furthermore, this type of analysis can reveal new molecular features that are critical to understanding the interplay between host and pathogen which remain unidentified by traditional histological assessments. Future studies combining molecular analysis with histopathological analysis can provide more information on molecular patterns of structures to investigate the biological implications of these newly discovered substructures of the *S. aureus* abscess.

CONCLUSIONS

Structural characterization at the site of infection is essential in elucidating host ganglioside function in response to invading pathogens such as *Staphylococcus aureus*. Differences in spatial distributions were observed for gangliosides of different classes, as well as for gangliosides that differ in ceramide chain composition and oligosaccharide-bound sialic acid. This work demonstrates that MALDI TIMS IMS can reveal new molecular layers within the abscess that cannot be discerned by pathohistological assessment and have previously gone undiscovered. Furthermore, integration of the TIMS-dimension allowed for the gas-phase separation of GM1b and GM1a, as well as Neu5Ac-tCer and Neu5Gc-dCer isomers within the soft tissue abscess. Spatial investigation of molecular distributions within infected tissues over 4, 6 and 10 dpi revealed alteration in relative GM1b/GM1a isomer abundance throughout the course of the infection. The work described herein provides an initial case study into studying ganglioside structural and spatial alterations throughout the course of infections. Here, MALDI TIMS IMS is shown to be an optimal technology for providing thorough characterization of complex lipid structures uncovering new molecular spatial localizations and abscess architecture, as well for providing molecular context for known anatomical substructures in infected tissue.

METHODS

Materials

DHA, ACA, hematoxylin, eosin, and ammonium sulfate were purchased from Sigma-Aldrich (St. Louis, MO, USA). HPLC-grade acetonitrile, methanol, ethanol, tetrahydrofuran, and chloroform were purchased from Fisher Scientific (Pittsburgh, PA, USA). ITO coated slides were purchased from Delta Technologies, Limited (Loveland, CO, USA).

Murine Model of *S. aureus* infection

Female BALB/cJ mice (6-8 week old) (Jackson Laboratory) were retro-orbitally infected with 1 x 10^7 colony forming units (CFU) in 100 µL of sterile phosphate-buffered saline as previously described.[162] Following infection, the mice were euthanized on 4, 6, or 10 dpi. The organs were removed, immediately frozen on a bed of dry ice, and stored at -80°C until further processing. All animal experimental protocols were reviewed and approved by the Vanderbilt University Institutional Animal Care and Use Committee and are in compliance with institutional

policies, NIH guidelines, the Animal Welfare Act, and the American Veterinary Medical Association guidelines on euthanasia.

Sample Preparation

Infected and control mouse kidney sections were cryosectioned to 10 µm thickness using a CM3050 S cryostat (Leica Biosystems, Wetzlar, Germany) and thaw-mounted onto conductive indium tin oxide-coated glass slides (Delta Technologies, Loveland, CO, USA). Matrix (2',5'-DHA with 62.5µM ammonium sulfate in 60% ethanol-water) was applied using a robotic M5 sprayer to a final matrix density of 1.23 µg/mm^2. Immediately following MALDI IMS, matrix was removed from the sample using 100% ethanol and rehydrated with graded ethanol and double distilled H_2O. Tissues were then stained using an H&E stain. Brightfield microscopy was obtained at 20x magnification using Zeis AxioScan Z1 slide scanner (Carl Zeiss Microscopy GmbH, Oberkochen, Germany).

Table 4.3. Matrix Deposition Parameters for Ganglioside Analysis within Murine Kidney Infection Model

	Concentration (mg/mL), Solvent	**Nozzle/Stage temperature (°C)**	**Velocity (m/min)**	**Passes (#)**	**Spray Speed (mL/min at pressure)**	**Matrix density (µg/mm^2)**
DHA-AmS	5.0, 60% Ethanol	60/50	1350	5	0.05, 10 psi	1.48
ACA	15, 95% THF, 5% DMF	50/55	4050	4	0.15, 8 psi	7.65
AmS	62.5 mM, 60% Ethanol	65/55	1350	25	0.01, 15 psi	1.48

MALDI TIMS MS

All experiments were carried out on a prototype MALDI timsTOF Pro mass spectrometer. Data were acquired in negative ionization mode (*m/z* 1000 – 3000) at 50 µm (45 µm beam scan) spatial resolution with ~50% laser power at 10 kHz, 400 shots per pixel, and 35680 (infected) and 19694 (control) pixels per sample. The following parameters were kept constant across all imaging experiments: ESI dry gas temperature – 100°C; Ion transfer time - 120 µs; pre-pulse storage time - 12 µs; collision RF - 3500 Vpp; TIMS funnel 1 RF - 450 Vpp; TIMS funnel 2 RF - 400 Vpp; multipole RF - 400 Vpp, collision cell entrance voltage - -200 V; MALDI deflection plate -90V. The source pressure was set to ~2.35 mBar to access higher $1/K_0$ ranges.

Identifications & Data Analysis

Serial tissue sections were analyzed for further structural investigation. To eliminate the possibility of isobaric interferences, a tissue section was analyzed using ultrahigh-spectra resolution FT-ICR MS (resolving power ~20,000 at *m/z* 1544). MALDI TIMS MS/MS experiments were used to show diagnostic and preferential a- / b-series fragments from standards and to confirm ganglioside identification from serial tissue section. MALDI TIMS IMS data were analyzed using DataAnalysis and visualized using SCiLS and a custom in-house developed software.

CHAPTER V

CONCLUSIONS AND FUTURE PERSPECTIVES

OVERVIEW

MALDI IMS is a well-established technology for untargeted *in situ* analysis of biomolecules. Here, integration of TIMS was demonstrated for the enhanced specificity of spatial lipidomics.[101,163] Specifically, TIMS separations greatly improved the peak capacity of lipid IMS experiments, where a threefold increase of detected features was observed.[1,2,99] This was achieved by resolving structurally distinct isobaric/isomeric species that overlap in the *m/z* dimension. Such common mass spectral ambiguities may hinder confident identification and spatial distribution assessment. Following this, MALDI TIMS separation of lipid isomer standards including *sn*-backbone isomers, acyl chain isomers, double-bond position isomers, and stereoisomers was demonstrated. MALDI TIMS was also used to resolve lipid isomers *in situ*, where their distinct spatial distributions were characterized in a whole-body mouse pup tissue sample.

Building on these initial experiments, more complex analytes, such as gangliosides were studied. This is a highly diverse class of molecules, with numerous biologically relevant isomeric structures. Their high structural heterogeneity and propensity for in-source fragmentation makes their intact analysis via MALDI IMS particularly challenging. Here, sample preparation conditions were optimized for MALDI TIMS IMS of gangliosides to enhance their detection at high spatial resolutions, with minimal analyte delocalization and in-source fragmentation. The developed methods were applied to rat brain and spinal cord tissue samples to reveal the spatial distributions of isomeric GD1a/b (d36:1) and GD1a/b (d38:1) species. This level of structural specificity in a spatially resolved context is not possible through standard IHC experiments nor through typical MALDI IMS workflows. This work suggests that MALDI TIMS IMS can be used for structurally informative spatial interrogation of this complex family of lipids in healthy and diseased tissues.

Optimized MALDI TIMS IMS methods were also applied to study ganglioside structural and spatial heterogeneity within an *S. aureus*-infected mouse kidney abscess. Differences in spatial distributions were observed for gangliosides of different classes, as well as for gangliosides that differ in ceramide chain composition and oligosaccharide-bound sialic acid. Gas-phase separations revealed the unique spatial distributions of monosialylated gangliosides isomers GM1a/GM1b and Neu5Ac-tCer /Neu5Gc-dCer GM1 within the host-pathogen interface. MALDI TIMS IMS is uniquely capable of tracking spatiotemporal alterations of ganglioside isomers. Imaging data collected at 4, 6, and 10 dpi revealed a decrease in the GM1b/GM1a ratio throughout the infection. These analyses also revealed molecular layers within the abscess that have not been previously identified by traditional histology. Collectively, this work shows that MALDI TIMS IMS can be used as a highly specific informative technique to survey the molecular diversity at the interface between host and pathogen.

Limitations of MALDI TIMS IMS of Gangliosides

The work described herein demonstrates MALDI TIMS IMS of gangliosides and the significant advances made in sample preparation procedures for their detection and isomer differentiation/visualization. Noteworthy limitations of this work include comprehensive profiling, quantification, and structural characterization for *in situ* ganglioside analysis. As discussed in **Chapter III**, heavily glycosylated glycosphingolipids suffer from low ionization efficiency and labile groups such as sialic acid or fucose readily undergo in-source fragmentation.[6] Although careful sample preparation strategies can significantly decrease these phenomena, intact ganglioside analysis over a wide mass range remains challenging. Consequently, comprehensive quantitative ganglioside analysis requires supplemental LC-MS. In addition to robust quantitation, LC-MS can provide additional insight into neutral glycosphingolipids such as globosides and cerebrosides that are undetected by MALDI without on-tissue derivatizations.[7,8]

On-tissue ganglioside isomers analysis was also demonstrated in this work (**Chapters III & IV**). Here, glycan positional isomers resulting from the varied position of sialic acids - GD1a and GD1b (**Chapter III**); GM1a and GM1b (**Chapter IV**) were differentiated by MALDI TIMS IMS. Although other structural differences are possible within the headgroup and the lipid tail, many isomers remained unresolved by TIMS separations. For example, the sialic acid link to the galactose unit can be either α2-3 or α2-6 (**Chapter IV**, **Figure 4.1**). Since this structural difference does not significantly alter the gas-phase conformation of the molecule, such isomers were not separated with TIMS. Similarly, isomers with subtle variations (double bond position/stereochemistry) in the ceramide unit also remained unresolved in the gas phase. Although TIMS can partially resolve double bond position/stereochemistry within glycerophospholipids, such as PCs (**Chapter II, Figure 2.4**), these differences were not revealed within gangliosides. Higher resolving power ion mobility systems, such as SLIM devices[9], may be employed to resolve such isomers. These analyses come at the expense of acquisition time and spatial information, as a SLIM MALDI platform is yet to be developed.[4] Alternatively, chemical derivatizations or modern fragmentation techniques can be used to differentiate these subtle structural differences. For example, sialic acid linkage-specific alkylamidation derivatization has been recently developed to distinguish different sialic linkages in glycosphingolipids, and photodissociation and ozone-induce dissociation are promising tools for double bond position/stereochemistry analysis.[6]

Lastly, although many studies have contributed to the current knowledge of ganglioside expression in immune cells, this information is incomplete and in many cases lacks structural details across immune cell subsets.[10] For example, although gangliosides have been comprehensively studied within T cells [11,12], not all immune cells have been thoroughly investigated. To date, hardly any studies on ganglioside expression from eosinophils, basophils, and natural killer cells exist.[13] Incomplete structural information poses a challenge in understanding the expression, regulation, and function of gangliosides in immune cells. Therefore, contextualizing alteration of ganglioside patterns within biological processes, such as in infections (**Chapter IV**) is uniquely challenging, as the basal ganglioside profiles of the present cell types are not defined. For this purpose, a systematic and comprehensive analysis of gangliosides in immune cells during their development, maturation, or activation is necessary to provide biological meaning. In general, optimization of global lipidomic methods to investigate a wide range of gangliosides in a quantitative manner, as well as highly specific derivatization/fragmentation techniques to elucidate subtle structural differences are necessary for comprehensive ganglioside analysis.

FUTURE PERSPECTIVES

Gangliosides exert diverse biological functions, including modulation of the immune system response.[76,78] However, information regarding their structural diversity within immune cell subsets is incomplete, largely due to the limitations of available analytical techniques. This poses a challenge in understanding the expression, regulation, and function of gangliosides in immune cells.[76] MALDI TIMS IMS can provide detailed structural and spatial information, making it an optimal analytical approach to study these molecules *in situ*. Here, ganglioside structural/spatial diversity was investigated within an *S. aureus* soft tissue abscess.

Abscess formation is the hallmark of *S. aureus* infections.[96,97] Past studies of the staphylococcal abscess architecture and its cellular contributors led to the development of a robust model of abscess formation (**Chapter I**).[98,148] Despite this, much remains unknown regarding the molecular drivers of the immune mechanisms involved in this process. While intra-abscess cellular heterogeneity can be studied through histochemical approaches, no molecular information can be provided. Conversely, untargeted molecular investigations, such as with MALDI IMS, can reveal new molecular layers without providing any information on the key cell types associated with observed molecular distributions. Future studies should integrate molecular imaging strategies with immunohistochemical approaches to correlate chemical signals with distinct immune cells. A suitable approach could incorporate multiplexed IHC which allows for the simultaneous detection of multiple biochemical markers within a single tissue section.[164] Supplemental molecular information can be provided by IMS for a more comprehensive understanding of cell composition, cellular function, and cell-cell interactions.

Soft tissue abscesses undergo dynamic changes throughout the course of an infection.[98] **Chapter IV** shows that MALDI TIMS IMS can be used to study spatiotemporal alterations of molecules in this environment. For example, the case study in **Chapter IV** revealed temporal alterations of ganglioside isomer abundances, where the overall ratio of GM1b to GM1a decreased throughout the infection. It was hypothesized that these alterations may be associated with macrophage stimulation and activation. However, changes in ganglioside patterns may involve multiple processes occurring simultaneously. For example, changes in ganglioside patterns may be a result of normal immune cell function, bacterial manipulation, and/or changes in cellular recruitment to the abscess.

As a first response to invading microorganisms, innate host immune cells, such as neutrophils, are rapidly recruited to the site of infection to remove pathogens. Host gangliosides are implicated in these interactions and aid in the differentiation/activation of immune cells, leading to alterations in their ganglioside repertoire. The direct interaction of immune cells with bacteria and bacterial toxins can also alter ganglioside patterns. Pathogens are known to circumvent the host innate immunity by altering immune cell gangliosides. Previous studies indicate that the glycan headgroup structure has a significant impact on pathogen-host interactions. For example, gangliosides with terminal sialic acid residues (such o-series GM1s) are more susceptible to bacterial adhesions[165] and have more immunosuppressive properties.[166] As infections progress, new immune cells with different ganglioside expression patterns are recruited to the site of infection. The introduction of new cells/molecules to the abscess further complicated assessment. Discerning if the observed changes in ganglioside patterns are a result of normal immune cell function or bacterial manipulation remains unclear. Future studies could investigate ganglioside significance in *S. aureus* infections by altering host ganglioside levels. In the context of *S. aureus* infections, inhibition/stimulation of host ganglioside synthesis may provide new

insight into their role in disease progression. Past studies have suggested that modulating host levels of glycosphingolipids could be a potential treatment strategy for infection control.[78] Although significant strides have been made towards understanding the role of gangliosides within infections, much of the knowledge remains descriptive with little translation to the clinical lab. Gaining fundamental insight into the metabolism of gangliosides, and glycosphingolipids as a whole is a promising avenue of research for potential treatment and/or prevention of infectious diseases.

VI. APPENDIX

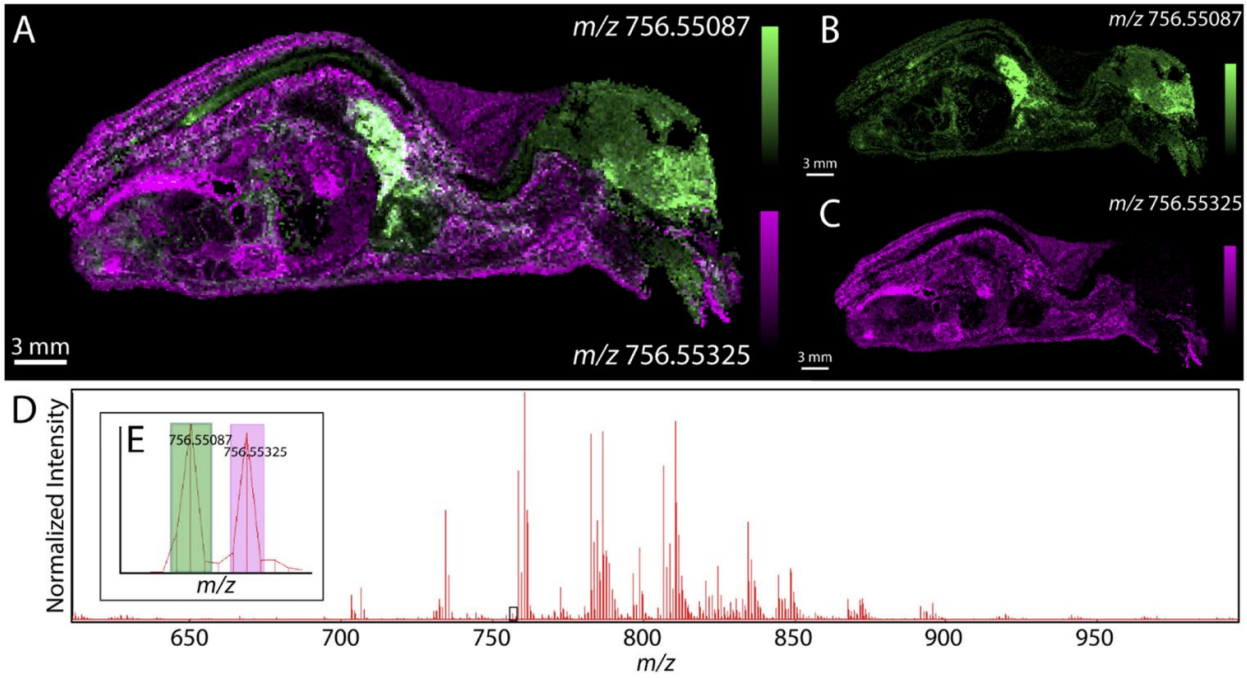

Figure 6.1. MALDI FT-ICR IMS data generated from whole body mouse pup tissue. **(A-C)** Ion images show unique spatial distributions for the nominally isobaric species detected at *m/z* 756.55087 and *m/z* 756.55325. These distributions were used to link this data to the mobility separated species detected by MALDI timsTOF IMS. **(D-E)** Spectral data show the ability of high mass-resolution MALDI FT-ICR MS to baseline resolve closely isobaric PC (32:0)Na^+ (*m/z* 756.55087) and PC(34:3)H^+ (*m/z* 756.55325). Reprinted with permission from Spraggins et. al.[1], Analytical Chemistry (2019) Copyright 2019 © American Chemical Society.

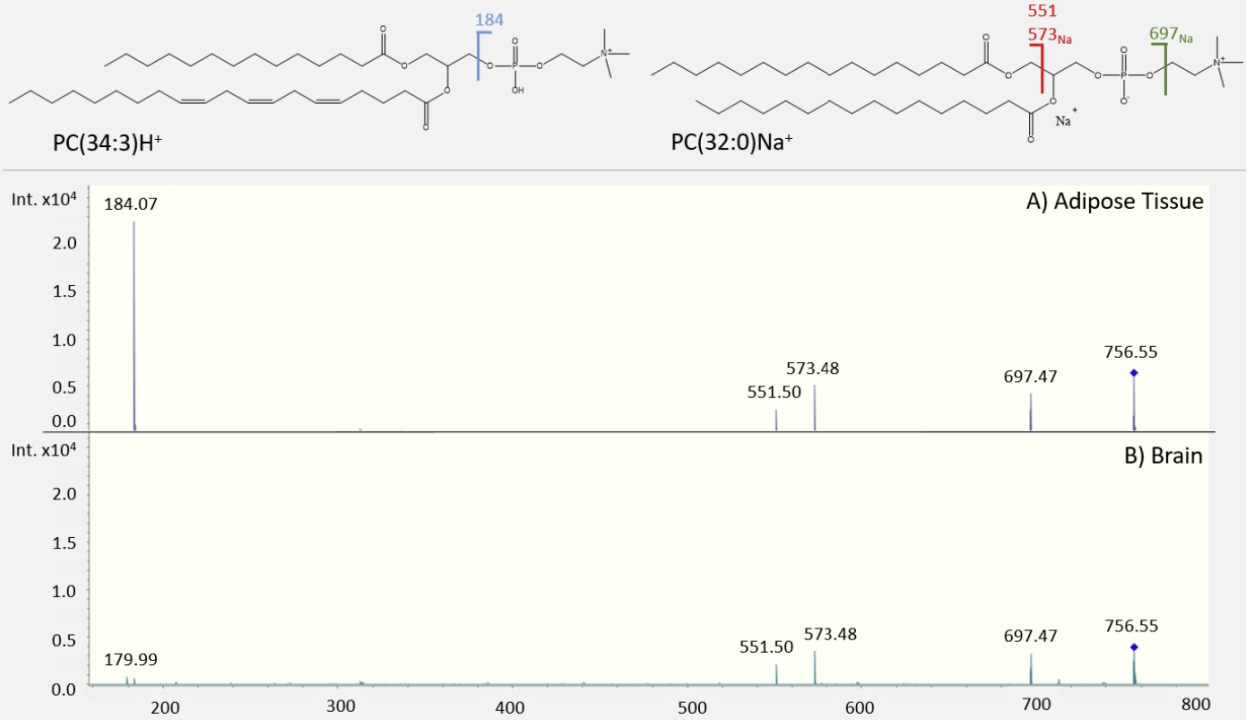

Figure 6.2. Collision induced dissociation (CID, 40 eV) data acquired on the prototype MALDI timsTOF platform to confirm the identity the isobaric lipid species as PC(34:3)H^+ and PC(32:0)Na^+. Spectra were acquired from both areas of adipose **(A)** and brain **(B)** tissue of a whole-body mouse pup. The spectra show distinct fragment ions indicating that the sodiated PC(32:0) is found predominantly in the brain and the protonated PC(34:3) is more abundant in the adipose tissue. The most significant difference between the two fragmentation experiments is the presence/absence of *m/z* 184 ion corresponding to the protonated phosphocholine head group. This ion, which is commonly observed as the base peak in CID spectra for protonated phosphocholines, is much less prominent when fragmenting sodiated species.[167] Reprinted with permission from Spraggins et. al.[1], Analytical Chemistry (2019) Copyright 2019 © American Chemical Society.

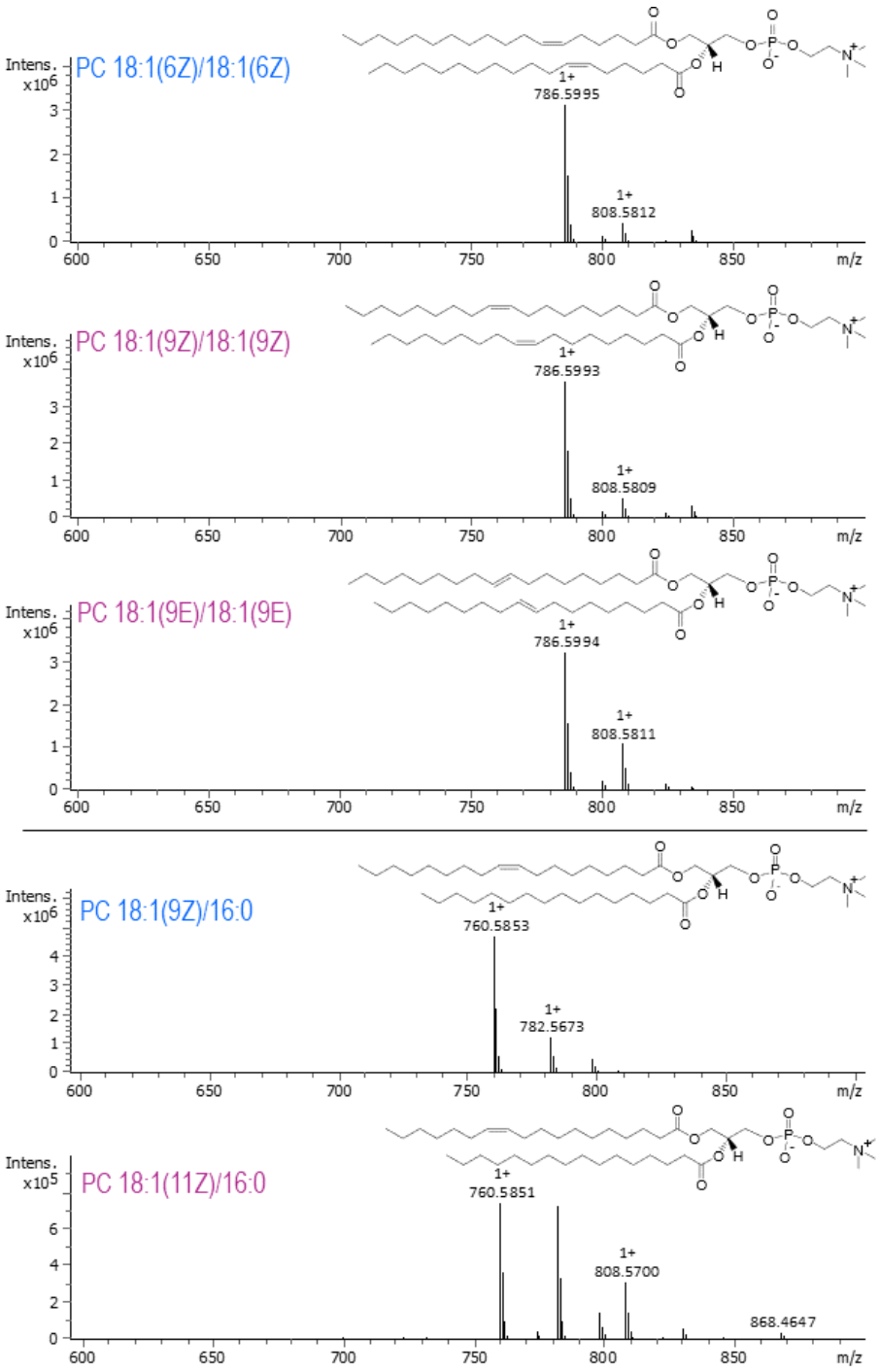

Figure 6.3. Negative ionization mode MALDI TIMS mass spectra of BMP(14:0/14:0) and PG(14:0/14:0) **(A)**; PG (18:0/18:2(9Z,12Z)), PG (18:1(9E)/18:1(9E)), and PG(18:1(9Z)/18:1(9Z)) **(B)**.

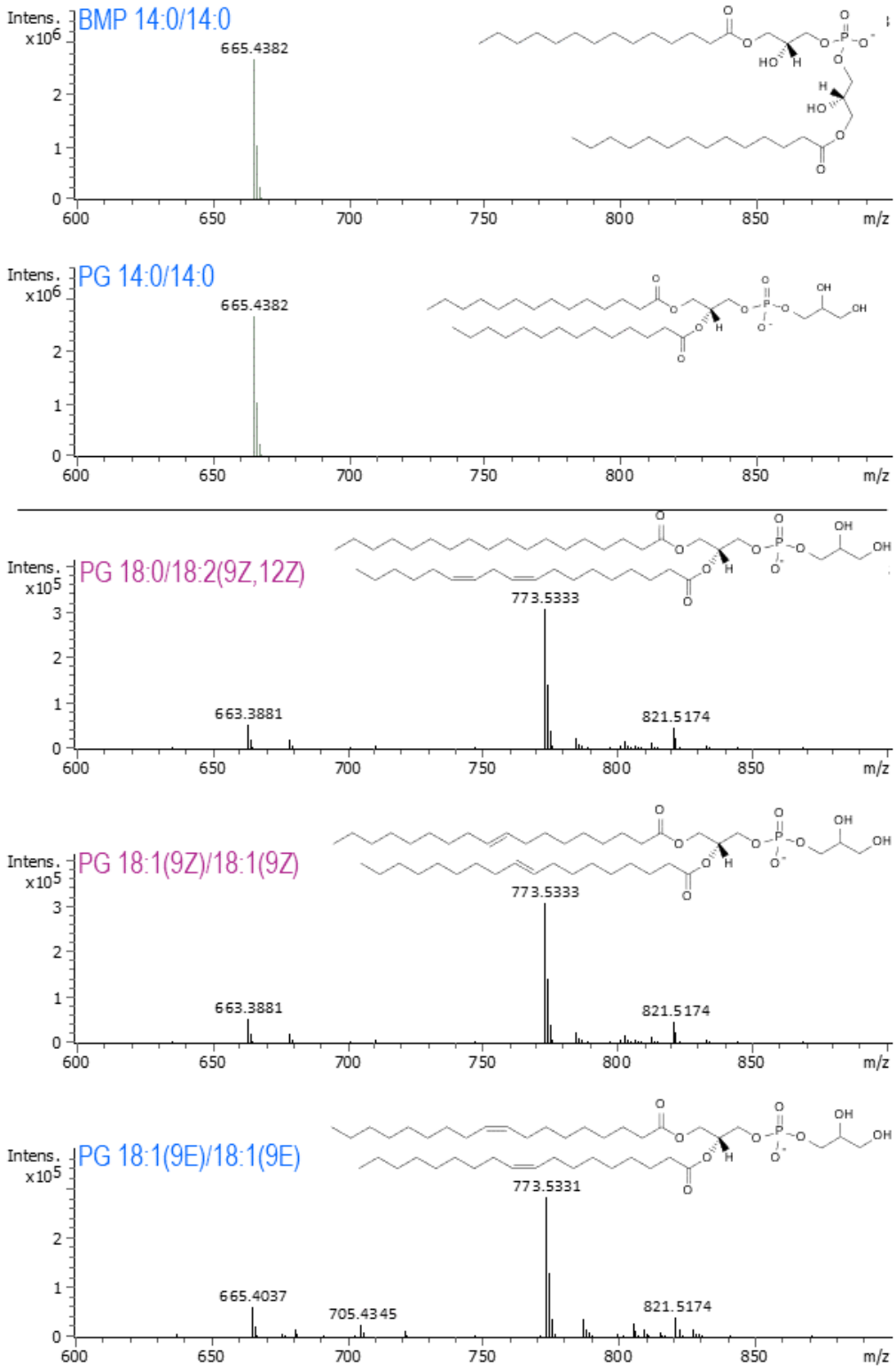

Figure 6.4. Positive ionization mode MALDI TIMS mass spectra of PC(18:1(6Z)/18:1(6Z)), PC(18:1(9Z)/18:1(9Z)), and PC(18:1(9E)/18:1(9E)) **(A)**; PC(18:1(9Z)/16:0) and PC(18:1(11Z)/16:0) **(B)**. Reprinted with permission from Djambazova et. al.[99], Analytical Chemistry (2020) Copyright 2020 © American Chemical Society.

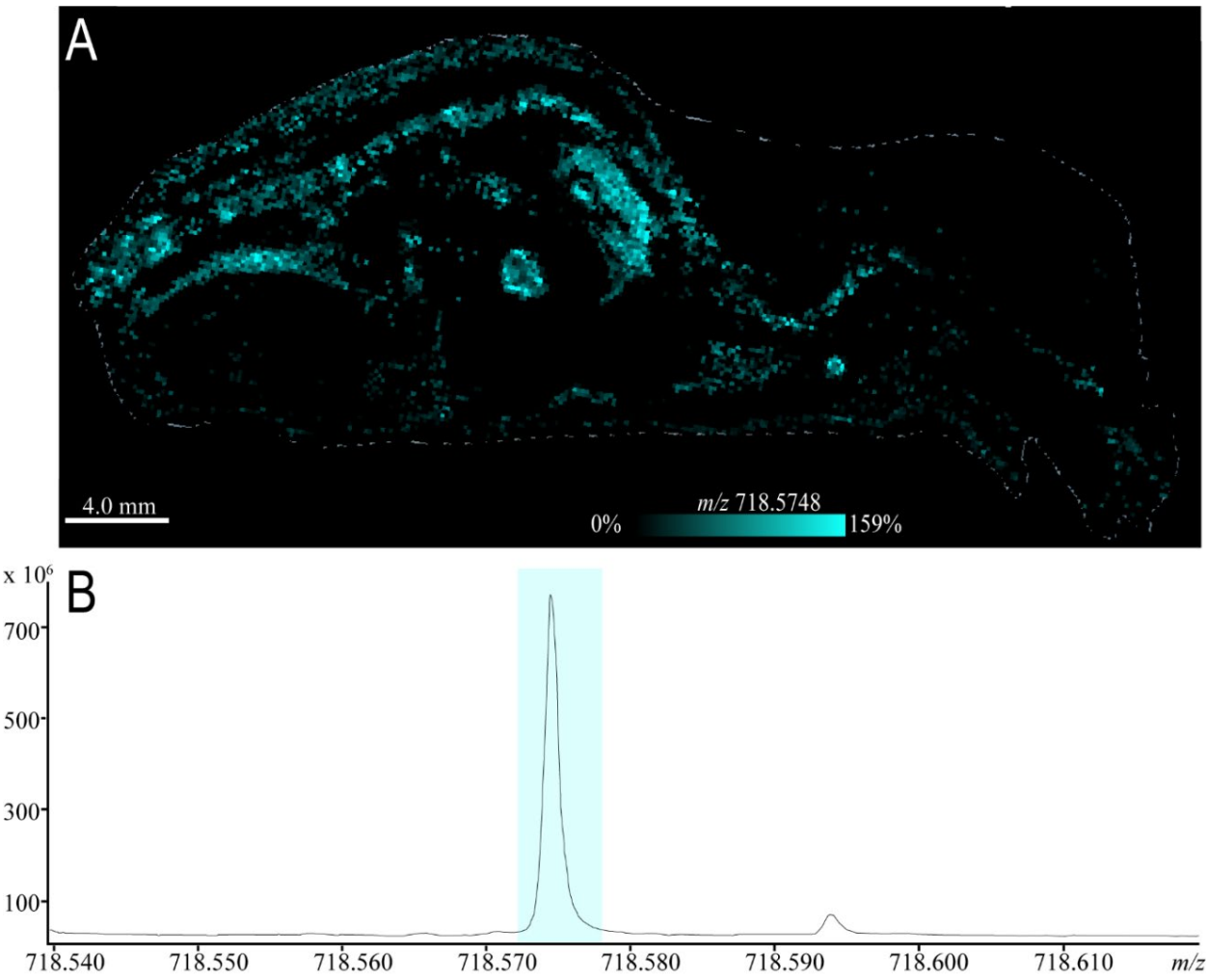

Figure 6.5 MALDI FT-ICR data generated for whole-body mouse pup. Ion image of *m/z* 718.5748 **(A)** shows spatial localizations that mimic those available from the composite image in **Figure 2.5A**. The mass spectrum **(B)** highlights a single peak at *m/z* 718.5748, suggesting there are no interfering peaks from to isobaric species. The lipid isomers with *m/z* 718.5748 were identified as $[CerP(t40:1) + H]^+$, $[PC(O\text{-}32:1) + H]^+$ and $[PC(P\text{-}32:0) + H]^+$. Reprinted with permission from Djambazova et. al.[99], Analytical Chemistry (2020) Copyright 2020 © American Chemical Society.

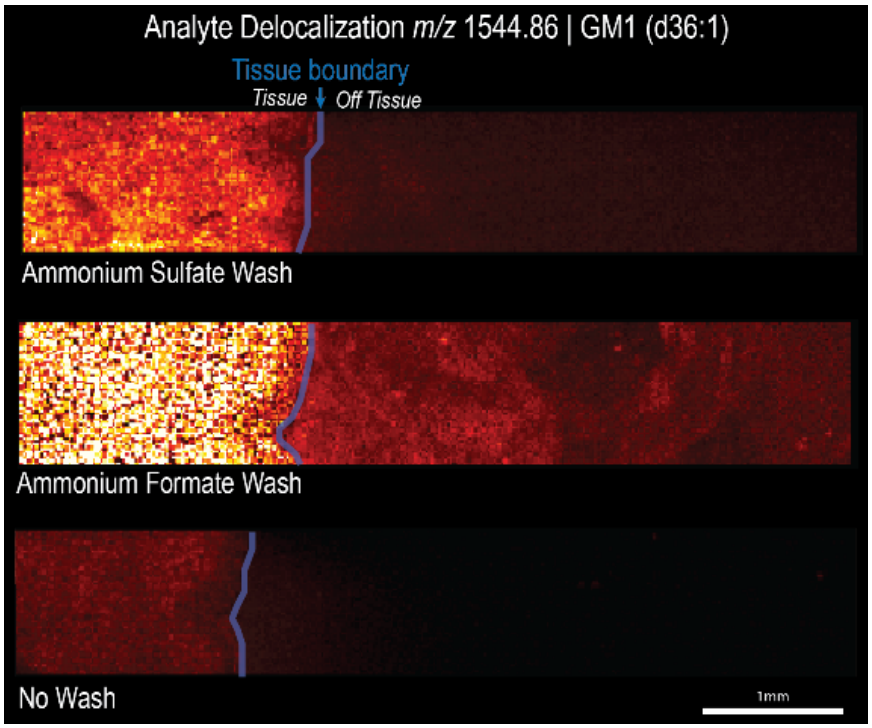

Figure 6.6. Analyte delocalization beyond the tissue boundary following an ammonium sulfate and ammonium formate wash as compared to no wash.

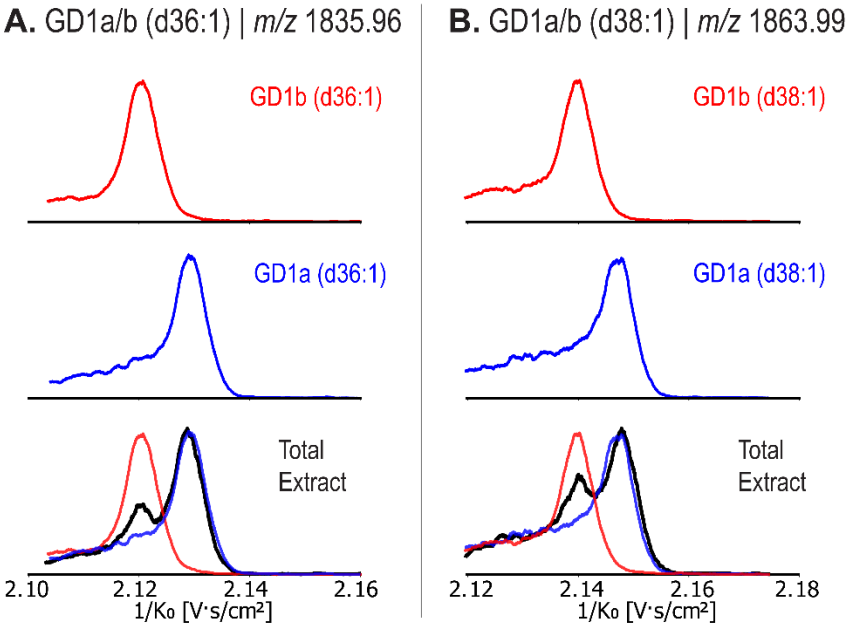

Figure 6.7. Extracted ion mobilograms for GD1b (red) and GD1a (blue) for GD1(d36:1) **(A)**, and GD1b (red) and GD1a (blue) for GD1(d38:1) **(B)**, aligned with the extracted ion mobilogram of *m/z* 1835. 96 and *m/z* 1863.99 from a total ganglioside extract of porcine brain.

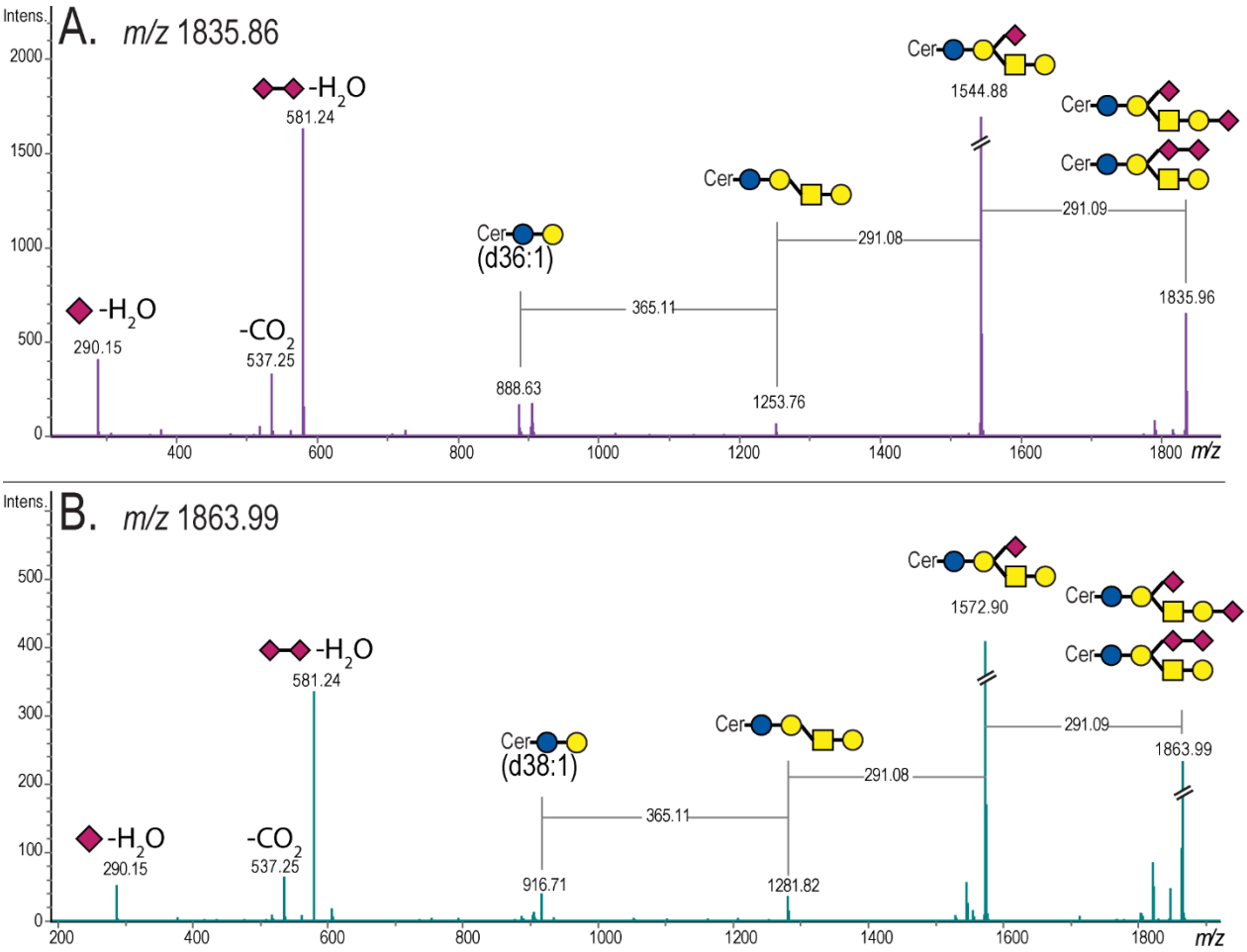

Figure 6.8. On-tissue MALDI fragmentation data collected from rat brain hippocampus (~1000 pixels) for *m/z* 1835.96 **(A)** and *m/z* 1864.99 **(B)** (CID: 75.0 eV, isolation window: ± *m/z* 1.5). The relative ratio of *m/z* 1544.88 and *m/z* 1572.90 to *m/z* 581.24 provide strong evidence that both a- and b- series isomers are present in the rat brain hippocampus. Fragment ions *m/z* 888.63 **(A)** and *m/z* 916.71 **(B)** corresponding to LacCer(d36:1) and LacCer(d38:1), respectively, provide information regarding the composition of the ceramide moiety. The intensities of peaks *m/z* 1544.88 **(A)**, *m/z* 1572.90 **(B)**, and *m/z* 1863.99 are 5067, 4077, and 1163, respectively.

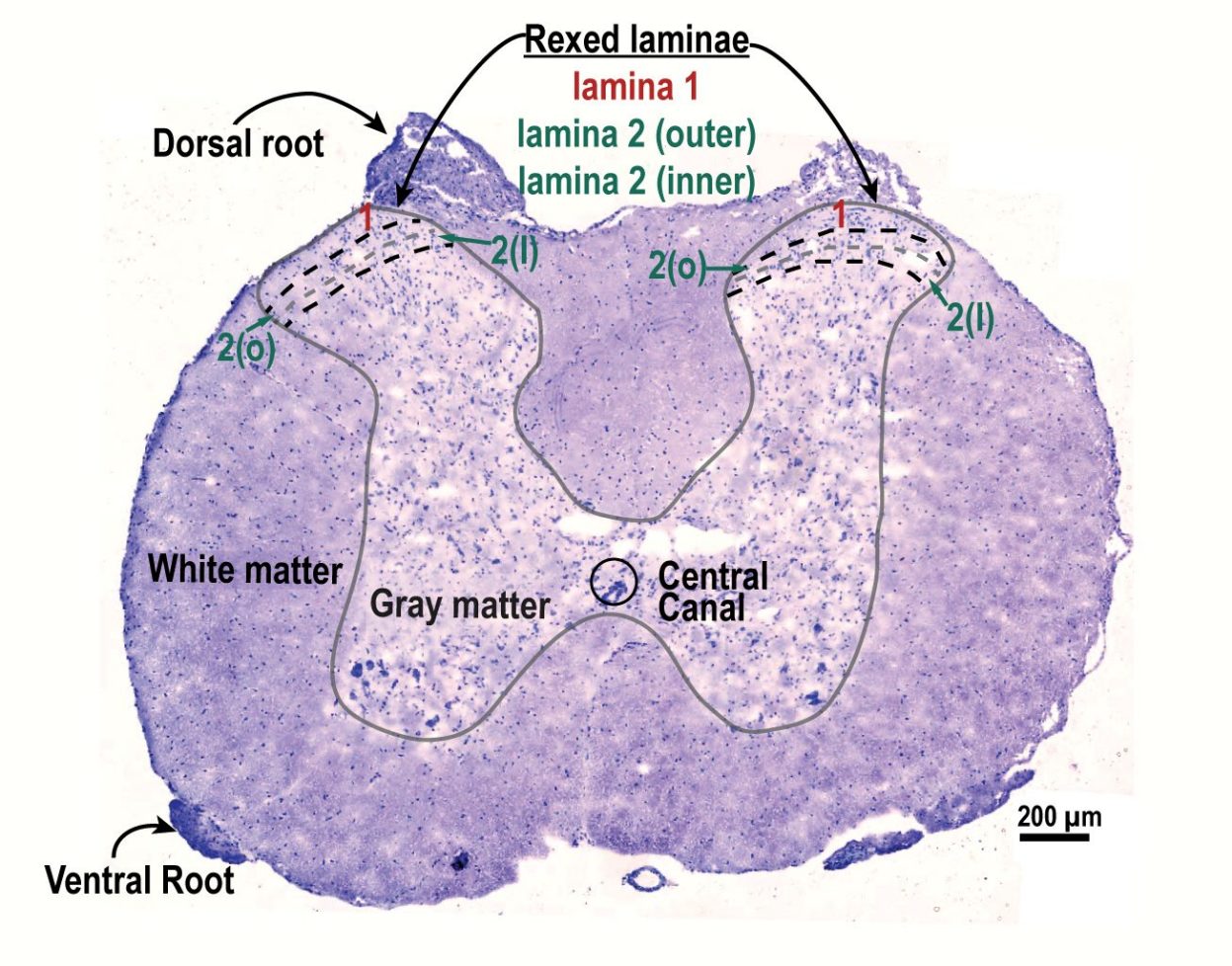

Figure 6.9. Annotated serial transverse section of a rat spinal cord in the sympathetic intermediolateral horn region, roughly between; T9 – T12. The cresyl-violet stain highlights the boundaries of the white/gray matter and roughly shows the location of the rexed lamiae of the dorsal horn, specifically laminae 1 and 2. Annotations were based on *The Atlas of Rat Spinal Cord.*[145]

REFERENCES

(1) Spraggins, J. M.; Djambazova, K. V.; Rivera, E. S.; Migas, L. G.; Neumann, E. K.; Fuetterer, A.; Suetering, J.; Goedecke, N.; Ly, A.; Van De Plas, R.; Caprioli, R. M. High-Performance Molecular Imaging with MALDI Trapped Ion-Mobility Time-of-Flight (TimsTOF) Mass Spectrometry. *Anal. Chem.* **2019**, *91* (22), 14552–14560. https://doi.org/10.1021/acs.analchem.9b03612.

(2) Rivera, E. S.; Djambazova, K. V.; Neumann, E. K.; Caprioli, R. M.; Spraggins, J. M. Integrating Ion Mobility and Imaging Mass Spectrometry for Comprehensive Analysis of Biological Tissues: A Brief Review and Perspective. *J. Mass Spectrom.* **2020**, *55* (12), e4614. https://doi.org/10.1002/JMS.4614.

(3) Seeley, E. H.; Schwamborn, K.; Caprioli, R. M. Imaging of Intact Tissue Sections: Moving beyond the Microscope. *J. Biol. Chem.* **2011**, *286* (29), 25459–25466. https://doi.org/10.1074/jbc.R111.225854.

(4) Caprioli, R. M.; Farmer, T. B.; Gile, J. Molecular Imaging of Biological Samples: Localization of Peptides and Proteins Using MALDI-TOF MS. *Anal. Chem.* **1997**, *69* (23), 4751–4760. https://doi.org/10.1021/AC970888I.

(5) Bodzon-Kulakowska, A.; Suder, P. Imaging Mass Spectrometry: Instrumentation, Applications, and Combination with Other Visualization Techniques. *Mass Spectrom. Rev.* **2016**, *35* (1), 147–169. https://doi.org/10.1002/MAS.21468.

(6) Buchberger, A. R.; DeLaney, K.; Johnson, J.; Li, L. Mass Spectrometry Imaging: A Review of Emerging Advancements and Future Insights. *Anal. Chem.* **2017**, *90* (1), 240–265. https://doi.org/10.1021/acs.analchem.7b04733.

(7) Mulder, I. A.; Esteve, C.; Wermer, M. J. H.; Hoehn, M.; Tolner, E. A.; van den Maagdenberg, A. M. J. M.; McDonnell, L. A. Funnel-Freezing versus Heat-Stabilization for the Visualization of Metabolites by Mass Spectrometry Imaging in a Mouse Stroke Model. *Proteomics* **2016**, *16* (11–12), 1652–1659. https://doi.org/10.1002/PMIC.201500402.

(8) Holthuis, J. C. M.; Menon, A. K. *Lipid Landscapes and Pipelines in Membrane Homeostasis*; Nature Publishing Group, 2014; Vol. 510, pp 48–57. https://doi.org/10.1038/nature13474.

(9) Signor, L.; Varesio, E.; Staack, R. F.; Starke, V.; Richter, W. F.; Hopfgartner, G. Analysis of Erlotinib and Its Metabolites in Rat Tissue Sections by MALDI Quadrupole Time-of-Flight Mass Spectrometry. *J. Mass Spectrom.* **2007**, *42* (7), 900–909. https://doi.org/10.1002/JMS.1225.

(10) Schober, Y.; Guenther, S.; Spengler, B.; Römpp, A. High-Resolution Matrix-Assisted Laser Desorption/Ionization Imaging of Tryptic Peptides from Tissue. *Rapid Commun. Mass Spectrom.* **2012**, *26* (9), 1141–1146. https://doi.org/10.1002/rcm.6192.

(11) Powers, T. W.; Neely, B. A.; Shao, Y.; Tang, H.; Troyer, D. A.; Mehta, A. S.; Haab, B. B.; Drake, R. R. MALDI Imaging Mass Spectrometry Profiling of N-Glycans in Formalin-Fixed Paraffin Embedded Clinical Tissue Blocks and Tissue Microarrays. *PLoS One* **2014**, *9* (9), e106255. https://doi.org/10.1371/journal.pone.0106255.

(12) Drake, R. R.; Powers, T. W.; Norris-Caneda, K.; Mehta, A. S.; Angel, P. M. In Situ Imaging of N-Glycans by MALDI Imaging Mass Spectrometry of Fresh or Formalin-Fixed Paraffin-Embedded Tissue. *Curr. Protoc. Protein Sci.* **2018**, *94* (1), e68. https://doi.org/10.1002/cpps.68.

(13) Prentice, B. M.; Ryan, D. J.; Van De Plas, R.; Caprioli, R. M.; Spraggins, J. M. Enhanced Ion Transmission Efficiency up to m / z 24 000 for MALDI Protein Imaging Mass Spectrometry. *Anal. Chem.* **2018**, *90* (8), 5090–5099. https://doi.org/10.1021/acs.analchem.7b05105.

(14) El-Aneed, A.; Cohen, A.; Banoub, J. Mass Spectrometry, Review of the Basics: Electrospray, MALDI, and Commonly Used Mass Analyzers. *Appl. Spectrosc. Rev.* **2009**, *44* (3), 210–230. https://doi.org/10.1080/05704920902717872.

(15) Angeletti, S.; Ciccozzi, M. Matrix-Assisted Laser Desorption Ionization Time-of-Flight Mass Spectrometry in Clinical Microbiology: An Updating Review. *Infect. Genet. Evol.* **2019**, *76*, 104063. https://doi.org/10.1016/J.MEEGID.2019.104063.

(16) Gyngard, F.; Steinhauser, M. L. Biological Explorations with Nanoscale Secondary Ion Mass Spectrometry. *J. Anal. At. Spectrom.* **2019**, *34* (8), 1534–1545. https://doi.org/10.1039/C9JA00171A.

(17) Gao, D.; Huang, X.; Tao, Y. A Critical Review of NanoSIMS in Analysis of Microbial Metabolic Activities at Single-Cell Level. *Crit. Rev. Biotechnol.* **2015**, *36* (5), 884–890. https://doi.org/10.3109/07388551.2015.1057550.

(18) Bowman, A. P.; Heeren, R. M. A.; Ellis, S. R. Advances in Mass Spectrometry Imaging Enabling Observation

of Localised Lipid Biochemistry within Tissues. *TrAC Trends Anal. Chem.* **2018**. https://doi.org/10.1016/J.TRAC.2018.07.012.

(19) Amstalden van Hove, E. R.; Smith, D. F.; Heeren, R. M. A. A Concise Review of Mass Spectrometry Imaging. *J. Chromatogr. A* **2010**, *1217* (25), 3946–3954. https://doi.org/10.1016/j.chroma.2010.01.033.

(20) Balluff, B.; Schöne, C.; Höfler, H.; Walch, A. MALDI Imaging Mass Spectrometry for Direct Tissue Analysis: Technological Advancements and Recent Applications. *Histochem. Cell Biol. 2011 1363* **2011**, *136* (3), 227–244. https://doi.org/10.1007/S00418-011-0843-X.

(21) Strupat, K.; Karas, M.; Hillenkamp, F. 2,5-Dihyroxybenzoic Acid - a New Matrix for Laser Desorption Ionization Mass Spectrometry. *Int. J. Mass Spectrom. Ion Process.* **1991**, *111*, 89–102. https://doi.org/10.1016/0168-1176(91)85050-v.

(22) Vermillion-Salsbury, R. L.; Hercules, D. M. 9-Aminoacridine as a Matrix for Negative Mode Matrix-Assisted Laser Desorption/Ionization. *Rapid Commun. Mass Spectrom.* **2002**, *16* (16), 1575–1581. https://doi.org/10.1002/rcm.750.

(23) Korte, A. R.; Lee, Y. J. MALDI-MS Analysis and Imaging of Small Molecule Metabolites with 1,5-Diaminonaphthalene (DAN). *J. Mass Spectrom.* **2014**, *49* (8), 737–741. https://doi.org/10.1002/JMS.3400.

(24) Trim, P. J.; Snel, M. F. Small Molecule MALDI MS Imaging: Current Technologies and Future Challenges. *Methods* **2016**, *104*, 127–141. https://doi.org/10.1016/J.YMETH.2016.01.011.

(25) Dinaiz, B. A. B.; Daniel, T.; Antony, S.; Roessner, B. U.; Boughton, B. A.; Thinagaran, D.; Sarabia, Á. D.; Bacic, Á. A.; Roessner, Á. U.; Bacic, A. Mass Spectrometry Imaging for Plant Biology: A Review. *Phytochem. Rev. 2015 153* **2015**, *15* (3), 445–488. https://doi.org/10.1007/S11101-015-9440-2.

(26) Murray, K. K.; Seneviratne, C. A.; Ghorai, S. High Resolution Laser Mass Spectrometry Bioimaging. *Methods* **2016**, *104*, 118–126. https://doi.org/10.1016/J.YMETH.2016.03.002.

(27) Kettling, H.; Vens-Cappell, S.; Soltwisch, J.; Pirkl, A.; Rg Haier, J.; Mü, J.; Dreisewerd, K. MALDI Mass Spectrometry Imaging of Bioactive Lipids in Mouse Brain with a Synapt G2-S Mass Spectrometer Operated at Elevated Pressure: Improving the Analytical Sensitivity and the Lateral Resolution to Ten Micrometers. *Anal. Chem.* **2014**, *86*, 3. https://doi.org/10.1021/ac5017248.

(28) Gessel, M. M.; Norris, J. L.; Caprioli, R. M. MALDI Imaging Mass Spectrometry: Spatial Molecular Analysis to Enable a New Age of Discovery. *J. Proteomics.* **2014**, *107*, 71–82. https://doi.org/10.1016/J.JPROT.2014.03.021.

(29) Wiley, W. C.; McLaren, I. H. Time-of-Flight Mass Spectrometer with Improved Resolution. *Rev. Sci. Instrum.* **2004**, *26* (12), 1150. https://doi.org/10.1063/1.1715212.

(30) Vestal, M. L.; Juhasz, P.; Martin, S. A. Delayed Extraction Matrix-Assisted Laser Desorption Time-of-Flight Mass Spectrometry. *Rapid Commun. Mass Spectrom.* **1995**, *9* (11), 1044–1050. https://doi.org/10.1002/RCM.1290091115.

(31) Mamyrin, B. A.; Karataev, V. I.; Shmikk, D. V; Zagulin, V. A. The Mass-Reflectron, a New Nonmagnetic Time-of-Flight Mass Spectrometer with High Resolution. **1973**.

(32) Marshall, A. G.; Hendrickson, C. L.; Jackson, G. S. FOURIER TRANSFORM ION CYCLOTRON RESONANCE MASS SPECTROMETRY: A PRIMER. *Mass Spectrom. Rev.* **1998**, *17*, 1–35. https://doi.org/10.1002/(SICI)1098-2787(1998)17:1.

(33) Porta Siegel, T.; Ekroos, K.; Ellis, S. R. Reshaping Lipid Biochemistry by Pushing Barriers in Structural Lipidomics. *Angew. Chem. Int. Ed.* **2019**, *58* (20), 6492–6501. https://doi.org/10.1002/anie.201812698.

(34) Damen, C. W. N.; Isaac, G.; Langridge, J.; Hankemeier, T.; Vreeken, R. J. Enhanced Lipid Isomer Separation in Human Plasma Using Reversed-Phase UPLC with Ion-Mobility/High-Resolution MS Detection. *J. Lipid Res.* **2014**, *55* (8), 1772–1783. https://doi.org/10.1194/jlr.D047795.

(35) Lamont, L.; Baumert, M.; Ogrinc Potočnik, N.; Allen, M.; Vreeken, R.; Heeren, R. M. A.; Porta, T. Integration of Ion Mobility MSE after Fully Automated, Online, High-Resolution Liquid Extraction Surface Analysis Micro-Liquid Chromatography. *Anal. Chem.* **2017**, *89* (20), 11143–11150. https://doi.org/10.1021/acs.analchem.7b03512.

(36) Sans, M.; Feider, C. L.; Eberlin, L. S. Advances in Mass Spectrometry Imaging Coupled to Ion Mobility Spectrometry for Enhanced Imaging of Biological Tissues. *Curr. Opin. Chem. Biol.* **2018**, *42*, 138–146. https://doi.org/10.1016/j.cbpa.2017.12.005.

(37) Eiceman, G. A.; Karpas, Z. Ion Mobility Spectrometry. *Ion Mobil. Spectrom.* **2005**. https://doi.org/10.1201/9781420038972.

(38) Gabelica, V.; Marklund, E. Fundamentals of Ion Mobility Spectrometry. *Curr. Opin. Chem. Biol.* **2018**, *42*, 51–59. https://doi.org/10.1016/J.CBPA.2017.10.022.

(39) Tu, J.; Zhou, Z.; Li, T.; Zhu, Z.-J. The Emerging Role of Ion Mobility-Mass Spectrometry in Lipidomics to

Facilitate Lipid Separation and Identification. *TrAC Trends Anal. Chem.* **2019**, *116*, 332–339. https://doi.org/10.1016/J.TRAC.2019.03.017.

(40) Gabelica, V.; Shvartsburg, A. A.; Afonso, C.; Barran, P.; Benesch, J. L. P.; Bleiholder, C.; Bowers, M. T.; Bilbao, A.; Bush, M. F.; Campbell, J. L.; Campuzano, I. D. G.; Causon, T.; Clowers, B. H.; Creaser, C. S.; De Pauw, E.; Far, J.; Fernandez-Lima, F.; Fjeldsted, J. C.; Giles, K.; Groessl, M.; Hogan, C. J.; Hann, S.; Kim, H. I.; Kurulugama, R. T.; May, J. C.; McLean, J. A.; Pagel, K.; Richardson, K.; Ridgeway, M. E.; Rosu, F.; Sobott, F.; Thalassinos, K.; Valentine, S. J.; Wyttenbach, T. Recommendations for Reporting Ion Mobility Mass Spectrometry Measurements. *Mass Spectrom. Rev.* **2019**, *38* (3), 291–320. https://doi.org/10.1002/mas.21585.

(41) Dodds, J. N.; Baker, E. S. Ion Mobility Spectrometry: Fundamental Concepts, Instrumentation, Applications, and the Road Ahead. *J. Am. Soc. Mass Spectrom.* **2019**, *30* (11), 2185–2195. https://doi.org/10.1007/S13361-019-02288-2/ASSET/IMAGES/LARGE/JS8B06240_0004.JPEG.

(42) May, J. C.; Goodwin, C. R.; Lareau, N. M.; Leaptrot, K. L.; Morris, C. B.; Kurulugama, R. T.; Mordehai, A.; Klein, C.; Barry, W.; Darland, E.; Overney, G.; Imatani, K.; Stafford, G. C.; Fjeldsted, J. C.; McLean, J. A. Conformational Ordering of Biomolecules in the Gas Phase: Nitrogen Collision Cross Sections Measured on a Prototype High Resolution Drift Tube Ion Mobility-Mass Spectrometer. *Anal. Chem.* **2014**, *86* (4), 2107–2116. https://doi.org/10.1021/ac4038448.

(43) Valentine, S. J.; Koeniger, S. L.; Clemmer, D. E. A Split-Field Drift Tube for Separation and Efficient Fragmentation of Biomolecular Ions. *Anal. Chem.* **2003**, *75* (22), 6202–6208. https://doi.org/10.1021/ac030111r.

(44) Giles, K.; Pringle, S. D.; Worthington, K. R.; Little, D.; Wildgoose, J. L.; Bateman, R. H. Applications of a Travelling Wave-Based Radio-Frequency-Only Stacked Ring Ion Guide. *Rapid Commun. Mass Spectrom.* **2004**, *18* (20), 2401–2414. https://doi.org/10.1002/RCM.1641.

(45) Purves, R. W.; Guevremont, R. Electrospray Ionization High-Field Asymmetric Waveform Ion Mobility Spectrometry-Mass Spectrometry. *Int. J. Mass Spectrom. Ion Process.* **1970**, *52* (3), 2346–2357. https://doi.org/10.1021/ac981380y.

(46) Kolakowski, B. M.; Mester, Z. Review of Applications of High-Field Asymmetric Waveform Ion Mobility Spectrometry (FAIMS) and Differential Mobility Spectrometry (DMS). *Analyst* **2007**, *132* (9), 842. https://doi.org/10.1039/b706039d.

(47) Guevremont, R. High-Field Asymmetric Waveform Ion Mobility Spectrometry: A New Tool for Mass Spectrometry. *J. Chromatogr. A.* **2004**, *1058* (1–2), 3–19. https://doi.org/10.1016/j.chroma.2004.08.119.

(48) Fernandez-Lima, F.; Kaplan, D. A.; Suetering, J.; Park, M. A. Gas-Phase Separation Using a Trapped Ion Mobility Spectrometer. *Int. J. Ion Mobil. Spectrom.* **2011**, *14* (2–3). https://doi.org/10.1007/s12127-011-0067-8.

(49) Michelmann, K.; Silveira, J. A.; Ridgeway, M. E.; Park, M. A. Fundamentals of Trapped Ion Mobility Spectrometry. *J. Am. Soc. Mass Spectrom.* **2015**, *26* (1), 14–24. https://doi.org/10.1007/s13361-014-0999-4.

(50) Silveira, J. A.; Michelmann, K.; Ridgeway, M. E.; Park, M. A. Fundamentals of Trapped Ion Mobility Spectrometry Part II: Fluid Dynamics. *J. Am. Soc. Mass Spectrom.* **2016**, *27* (4), 585–595. https://doi.org/10.1007/s13361-015-1310-z.

(51) Dodds, J. N.; May, J. C.; McLean, J. A. Correlating Resolving Power, Resolution, and Collision Cross Section: Unifying Cross-Platform Assessment of Separation Efficiency in Ion Mobility Spectrometry. *Anal. Chem.* **2017**, *89* (22), 12176–12184. https://doi.org/10.1021/acs.analchem.7b02827.

(52) Deng, L.; Ibrahim, Y. M.; Baker, E. S.; Aly, N. A.; Hamid, A. M.; Zhang, X.; Zheng, X.; Garimella, S. V. B.; Webb, I. K.; Prost, S. A.; Sandoval, J. A.; Norheim, R. V.; Anderson, G. A.; Tolmachev, A. V.; Smith, R. D. Ion Mobility Separations of Isomers Based upon Long Path Length Structures for Lossless Ion Manipulations Combined with Mass Spectrometry. *ChemistrySelect* **2016**, *1* (10), 2396–2399. https://doi.org/10.1002/slct.201600460.

(53) Ibrahim, Y. M.; Hamid, A. M.; Deng, L.; Garimella, S. V. B.; Webb, I. K.; Baker, E. S.; Smith, R. D. New Frontiers for Mass Spectrometry Based upon Structures for Lossless Ion Manipulations. *Analyst.* **2017**, *142* (7), 1010–1021. https://doi.org/10.1039/c7an00031f.

(54) Ridgeway, M. E.; Lubeck, M.; Jordens, J.; Mann, M.; Park, M. A. Trapped Ion Mobility Spectrometry: A Short Review. *Int. J. Mass Spectrom.* **2018**, *425*, 22–35. https://doi.org/10.1016/J.IJMS.2018.01.006.

(55) Fernandez-Lima, F. A.; Kaplan, D. A.; Park, M. A. Note: Integration of Trapped Ion Mobility Spectrometry with Mass Spectrometry. *Rev. Sci. Instrum.* **2011**, *82* (12), 126106. https://doi.org/10.1063/1.3665933.

(56) Shevchenko, A.; Simons, K. Lipidomics: Coming to Grips with Lipid Diversity. *Nat. Rev. Mol. Cell. Biol.* **2010**, *11* (8), 593–598. https://doi.org/10.1038/nrm2934.

(57) O'Donnell, V. B.; Ekroos, K.; Liebisch, G.; Wakelam, M. Lipidomics: Current State of the Art in a Fast Moving Field. *Syst. Biol. Med.* **2020**, *12* (1), e1466. https://doi.org/10.1002/wsbm.1466.
(58) Yang, K.; Han, X. Lipidomics: Techniques, Applications, and Outcomes Related to Biomedical Sciences. *Trends Biochem. Sci.* **2016**, *41* (11), 954–969. https://doi.org/10.1016/j.tibs.2016.08.010.
(59) Hu, T.; Zhang, J. L. Mass-Spectrometry-Based Lipidomics. *Journal of Separation Science*. Wiley-VCH Verlag January 1, 2018, pp 351–372. https://doi.org/10.1002/jssc.201700709.
(60) Gode, D.; Volmer, D. A. Lipid Imaging by Mass Spectrometry-a Review. *Analyst.* **2013**, *138* (5), 1289–1315. https://doi.org/10.1039/c2an36337b.
(61) Berry, K. A. Z.; Hankin, J. A.; Barkley, R. M.; Spraggins, J. M.; Caprioli, R. M.; Murphy, R. C. MALDI Imaging of Lipid Biochemistry in Tissues by Mass Spectrometry. *Chem. Rev.* **2011**, *111* (10), 6491. https://doi.org/10.1021/CR200280P.
(62) Köfeler, H. C.; Fauland, A.; Rechberger, G. N.; Trötzmüller, M. Mass Spectrometry Based Lipidomics: An Overview of Technological Platforms. *Metabolites* **2012**, *2* (1), 19–38. https://doi.org/10.3390/metabo2010019.
(63) Paine, M. R. L. L.; Poad, B. L. J. J.; Eijkel, G. B.; Marshall, D. L.; Blanksby, S. J.; Heeren, R. M. A. A.; Ellis, S. R. Mass Spectrometry Imaging with Isomeric Resolution Enabled by Ozone-Induced Dissociation. *Angew. Chem. Int. Ed.* **2018**, *57* (33), 10530–10534. https://doi.org/10.1002/anie.201802937.
(64) Sandra, K.; Sandra, P. Lipidomics from an Analytical Perspective. *Curr. Opin. Chem. Biol.* **2013**, *17* (5), 847–853. https://doi.org/10.1016/j.cbpa.2013.06.010.
(65) Rustam, Y. H.; Reid, G. E. Analytical Challenges and Recent Advances in Mass Spectrometry Based Lipidomics. *Anal. Chem.* American Chemical Society January 2, 2018, pp 374–397. https://doi.org/10.1021/acs.analchem.7b04836.
(66) Murphy, R. C.; Hankin, J. A.; Barkley, R. M. Imaging of Lipid Species by MALDI Mass Spectrometry. *Journal of Lipid Research*. American Society for Biochemistry and Molecular Biology April 1, 2009, pp S317–S322. https://doi.org/10.1194/jlr.R800051-JLR200.
(67) Tang, F.; Guo, C.; Ma, X.; Zhang, J.; Su, Y.; Tian, R.; Shi, R.; Xia, Y.; Wang, X.; Ouyang, Z. Rapid in Situ Profiling of Lipid C=C Location Isomers in Tissue Using Ambient Mass Spectrometry with Photochemical Reactions. *Anal. Chem.* **2018**, *90* (9), 5612–5619. https://doi.org/10.1021/acs.analchem.7b04675.
(68) Kozlowski, R. L.; Mitchell, T. W.; Blanksby, S. J. A Rapid Ambient Ionization-Mass Spectrometry Approach to Monitoring the Relative Abundance of Isomeric Glycerophospholipids. *Sci. Rep.* **2015**, *5* (1), 1–9. https://doi.org/10.1038/srep09243.
(69) Klein, D. R.; Feider, C. L.; Garza, K. Y.; Lin, J. Q.; Eberlin, L. S.; Brodbelt, J. S. Desorption Electrospray Ionization Coupled with Ultraviolet Photodissociation for Characterization of Phospholipid Isomers in Tissue Sections. *Anal. Chem.* **2018**, *90*, 10. https://doi.org/10.1021/acs.analchem.8b03026.
(70) Zheng, X.; Smith, R. D.; Baker, E. S. Recent Advances in Lipid Separations and Structural Elucidation Using Mass Spectrometry Combined with Ion Mobility Spectrometry, Ion-Molecule Reactions and Fragmentation Approaches. *Curr. Opin. Chem. Biol.* Elsevier Ltd February 1, 2018, pp 111–118. https://doi.org/10.1016/j.cbpa.2017.11.009.
(71) Zhong, Y.; Hyung, S.-J.; Ruotolo, B. T. Characterizing the Resolution and Accuracy of a Second-Generation Traveling-Wave Ion Mobility Separator for Biomolecular Ions. *Analyst* **2011**, *136* (17), 3534. https://doi.org/10.1039/c0an00987c.
(72) Wu, Q.; Wang, J. Y.; Han, D. Q.; Yao, Z. P. Recent Advances in Differentiation of Isomers by Ion Mobility Mass Spectrometry. *TrAC - Trends Anal. Chem.* **2020**, *124*, 115801. https://doi.org/10.1016/j.trac.2019.115801.
(73) Svennerholm, L. The Gangliosides. *J. Lipid Res.* **1964**, *5* (2), 145–155. https://doi.org/10.1016/s0022-2275(20)40231-7.
(74) Ando, S.; Svennerholm, L.; Rahmann, H. Gangliosides in the Nervous System. *Tanpakushitsu Kakusan Koso.* **1984**, *29* (12 Suppl), 1146–1159. https://doi.org/10.1016/B978-0-08-031994-0.50031-1.
(75) Rajanayake, K. K.; Markus, K.; Isailovic, D. Determination of the Origin of Doubly-Cationized Monosialylated Fragments in MS/MS Spectra of Singly-Cationized LSTb and GM1 Using Ion Mobility Spectrometry-Mass Spectrometry. *Int. J. Mass. Spectrom.* **2017**, *422*, 1–12. https://doi.org/10.1016/j.ijms.2017.07.007.
(76) Zhang, T.; De Waard, A. A.; Wuhrer, M.; Spaapen, R. M. The Role of Glycosphingolipids in Immune Cell Functions. *Front. Immunol.* **2019**, *10* (JAN), 90. https://doi.org/10.3389/FIMMU.2019.00090/BIBTEX.
(77) Gangliosides as Immunomodulators.
(78) Aerts, J. M. F. G.; Artola, M.; van Eijk, M.; Ferraz, M. J.; Boot, R. G. Glycosphingolipids and Infection.

Potential New Therapeutic Avenues. *Front. Cell Dev. Biol. Cell Dev. Biol.* **2019**, *7*, 324. https://doi.org/10.3389/FCELL.2019.00324/BIBTEX.

(79) Barrientos, R. C.; Zhang, Q. Recent Advances in the Mass Spectrometric Analysis of Glycosphingolipidome – A Review. *Anal. Chim. Acta.* **2020**, *1132*, 134–155. https://doi.org/10.1016/J.ACA.2020.05.051.

(80) AWASTHI, Y. C.; SRIVASTAVA, S. K. STRUCTURE, FUNCTION AND METABOLISM OF GLYCOSPHINGOLIPIDS. *Biochem. Brain* **1980**, 1–20. https://doi.org/10.1016/B978-0-08-021345-3.50004-6.

(81) Yu, R. K.; Tsai, Y. T.; Ariga, T.; Yanagisawa, M. Structures, Biosynthesis, and Functions of Gangliosides-an Overview. *J. Oleo Sci.* NIH Public Access 2011, pp 537–544. https://doi.org/10.5650/jos.60.537.

(82) Futerman, A. H.; Riezman, H. The Ins and Outs of Sphingolipid Synthesis. *Trends Cell. Biol.* Elsevier Current Trends June 1, 2005, pp 312–318. https://doi.org/10.1016/j.tcb.2005.04.006.

(83) Muggli, T.; Bühr, C.; Schürch, S. Challenges in the Analysis of Gangliosides by LC-MS. *Chimia (Aarau).* **2022**, *76* (1–2), 109. https://doi.org/10.2533/chimia.2022.109.

(84) Škrášková, K.; Claude, E.; Jones, E. A.; Towers, M.; Ellis, S. R.; Heeren, R. M. A. Enhanced Capabilities for Imaging Gangliosides in Murine Brain with Matrix-Assisted Laser Desorption/Ionization and Desorption Electrospray Ionization Mass Spectrometry Coupled to Ion Mobility Separation. *Methods* **2016**, *104*, 69–78. https://doi.org/10.1016/J.YMETH.2016.02.014.

(85) Colsch, B.; Jackson, S. N.; Dutta, S.; Woods, A. S. Molecular Microscopy of Brain Gangliosides: Illustrating Their Distribution in Hippocampal Cell Layers. *ACS Chem. Neurosci.* **2011**, *2* (4), 213–222. https://doi.org/10.1021/cn100096h.

(86) Jackson, S. N.; Muller, L.; Roux, A.; Oktem, B.; Moskovets, E.; Doroshenko, V. M.; Woods, A. S. AP-MALDI Mass Spectrometry Imaging of Gangliosides Using 2,6-Dihydroxyacetophenone. *J. Am. Soc. Mass Spectrom* **2018**, *29*, 1463–1472. https://doi.org/10.1007/s13361-018-1928-8.

(87) Li, Z.; Zhang, Q. Ganglioside Isomer Analysis Using Ion Polarity Switching Liquid Chromatography-Tandem Mass Spectrometry. *Anal. Bioanal. Chem.* **2021**, *413* (12), 3269–3279. https://doi.org/10.1007/S00216-021-03262-2.

(88) Park, J. Y.; Shrestha, S. A.; Cha, S. Isomer Separation and Analysis of Amphiphilic Polysialogangliosides Using Reversed-Phase Liquid Chromatography-Mass Spectrometry. *J. Sep. Sci.* **2021**, *44* (9), 1824–1832. https://doi.org/10.1002/JSSC.202001248.

(89) Sarbu, M.; Petrica, L.; Clemmer, D. E.; Vukelić, Ž.; Zamfir, A. D. Gangliosides of Human Glioblastoma Multiforme: A Comprehensive Mapping and Structural Analysis by Ion Mobility Tandem Mass Spectrometry. *J. Am. Soc. Mass Spectrom.* **2021**, *32* (5), 1249–1257. https://doi.org/10.1021/jasms.1c00088.

(90) Ariga, T.; McDonald, M. P.; Yu, R. K. Role of Ganglioside Metabolism in the Pathogenesis of Alzheimer's Disease - A Review. *J. Lipid Res.* **2008**, *49* (6), 1157–1175. https://doi.org/10.1194/jlr.R800007-JLR200.

(91) Oikawa, N.; Matsubara, T.; Fukuda, R.; Yasumori, H.; Hatsuta, H.; Murayama, S.; Sato, T.; Suzuki, A.; Yanagisawa, K. Imbalance in Fatty-Acid-Chain Length of Gangliosides Triggers Alzheimer Amyloid Deposition in the Precuneus. **2015**, *10* (3), e0121356.

(92) Zhang, Y.; Wang, J.; Liu, J.; Han, J.; Xiong, S.; Yong, W.; Zhao, Z. Combination of ESI and MALDI Mass Spectrometry for Qualitative, Semi-Quantitative and in Situ Analysis of Gangliosides in Brain. *Sci. Rep.* **2016**, *6* (1), 1–11. https://doi.org/10.1038/srep25289.

(93) Wormwood Moser, K. L.; Van Aken, G.; DeBord, D.; Hatcher, N. G.; Maxon, L.; Sherman, M.; Yao, L.; Ekroos, K. High-Defined Quantitative Snapshots of the Ganglioside Lipidome Using High Resolution Ion Mobility SLIM Assisted Shotgun Lipidomics. *Anal. Chim. Acta.* **2021**, *1146*, 77–87. https://doi.org/10.1016/j.aca.2020.12.022.

(94) Jackson, S. N.; Ugarov, M.; Egan, T.; Post, J. D.; Langlais, D.; Schultz, J. A.; Woods, A. S. MALDI-Ion Mohility-TOFMS Imaging of Lipids in Rat Brain Tissue. *J. Mass Spectrom.* **2007**, *42* (8), 1093–1098. https://doi.org/10.1002/jms.1245.

(95) Rolando, M.; Buchrieser, C. A Comprehensive Review on the Manipulation of the Sphingolipid Pathway by Pathogenic Bacteria. *Front. Cell Dev. Biol.* Frontiers Media S.A. August 21, 2019, p 168. https://doi.org/10.3389/fcell.2019.00168.

(96) Cheng, A. G.; Hwan, K. K.; Burts, M. L.; Krausz, T.; Schneewind, O.; Missiakas, D. M. Genetic Requirements for Staphylococcus Aureus Abscess Formation and Persistence in Host Tissues. *FASEB J.* **2009**, *23* (10), 3393–3404. https://doi.org/10.1096/FJ.09-135467.

(97) Cheng, A. G.; DeDent, A. C.; Schneewind, O.; Missiakas, D. A Play in Four Acts: Staphylococcus Aureus Abscess Formation. *Trends Microbiol.* **2011**, *19* (5), 225. https://doi.org/10.1016/J.TIM.2011.01.007.

(98) Brandt, S. L.; Putnam, N. E.; Cassat, J. E.; Serezani, C. H. Innate Immunity to Staphylococcus Aureus:

Evolving Paradigms in Soft Tissue and Invasive Infections. *J. Immunol.* **2018**, *200* (12), 3871–3880. https://doi.org/10.4049/JIMMUNOL.1701574.

(99) Djambazova, K.; Klein, D. R.; Migas, L. G.; Neumann, E. K.; Rivera, E. S.; Van de Plas, R.; Caprioli, R. M.; Spraggins, J. M. Resolving the Complexity of Spatial Lipidomics Using MALDI TIMS Imaging Mass Spectrometry. *Anal. Chem.* **2020**, *92* (19), 13290–13297. https://doi.org/10.1021/acs.analchem.0c02520.

(100) Liebisch, G.; Vizcaíno, J. A.; Köfeler, H.; Trötzmüller, M.; Griffiths, W. J.; Schmitz, G.; Spener, F.; Wakelam, M. J. O. Shorthand Notation for Lipid Structures Derived from Mass Spectrometry. *J. Lipid Res.* **2013**, *54* (6), 1523–1530. https://doi.org/10.1194/jlr.M033506.

(101) Stoeckli, M.; Chaurand, P.; Hallahan, D. E.; Caprioli, R. M. Imaging Mass Spectrometry: A New Technology for the Analysis of Protein Expression in Mammalian Tissues. *Nat. Med.* **2001**, *7* (4), 493–496. https://doi.org/10.1038/86573.

(102) Klein, D. R.; Brodbelt, J. S. Structural Characterization of Phosphatidylcholines Using 193 Nm Ultraviolet Photodissociation Mass Spectrometry. *Anal. Chem.* **2017**, *89* (3), 1516–1522. https://doi.org/10.1021/acs.analchem.6b03353.

(103) Mitchell, T. W.; Pham, H.; Thomas, M. C.; Blanksby, S. J. Identification of Double Bond Position in Lipids: From GC to OzID. *J. Chromatogr. B.* **2009**, *877* (26), 2722–2735. https://doi.org/10.1016/j.jchromb.2009.01.017.

(104) Hinz, C.; Liggi, S.; Griffin, J. L. The Potential of Ion Mobility Mass Spectrometry for High-Throughput and High-Resolution Lipidomics. *Curr. Opin. Chem. Biol.* 2018. https://doi.org/10.1016/j.cbpa.2017.10.018.

(105) Jeanne Dit Fouque, K.; Ramirez, C. E.; Lewis, R. L.; Koelmel, J. P.; Garrett, T. J.; Yost, R. A.; Fernandez-Lima, F. Effective Liquid Chromatography–Trapped Ion Mobility Spectrometry–Mass Spectrometry Separation of Isomeric Lipid Species. *Anal. Chem.* **2019**, *91* (8), 5021–5027. https://doi.org/10.1021/acs.analchem.8b04979.

(106) Fu, T.; Oetjen, J.; Chapelle, M.; Verdu, A.; Szesny, M.; Chaumot, A.; Degli-Esposti, D.; Geffard, O.; Clément, Y.; Salvador, A.; Ayciriex, S. In Situ Isobaric Lipid Mapping by MALDI-Ion Mobility Separation-Mass Spectrometry Imaging. *J. Mass Spectrom.* **2020**, e4531. https://doi.org/10.1002/jms.4531.

(107) Wang, M.; Huang, Y.; Han, X. Accurate Mass Searching of Individual Lipid Species Candidates from High-Resolution Mass Spectra for Shotgun Lipidomics. *Rapid Commun. Mass Spectrom.* **2014**, *28* (20), 2201–2210. https://doi.org/10.1002/rcm.7015.

(108) Bielow, C.; Mastrobuoni, G.; Orioli, M.; Kempa, S. On Mass Ambiguities in High-Resolution Shotgun Lipidomics. *Anal. Chem.* **2017**, *89* (5), 2986–2994. https://doi.org/10.1021/acs.analchem.6b04456.

(109) Kyle, J. E.; Zhang, X.; Weitz, K. K.; Monroe, M. E.; Ibrahim, Y. M.; Moore, R. J.; Cha, J.; Sun, X.; Lovelace, E. S.; Wagoner, J.; Polyak, S. J.; Metz, T. O.; Dey, S. K.; Smith, R. D.; Burnum-Johnson, K. E.; Baker, E. S. Uncovering Biologically Significant Lipid Isomers with Liquid Chromatography, Ion Mobility Spectrometry and Mass Spectrometry. *Analyst* **2016**, *141* (5), 1649–1659. https://doi.org/10.1039/c5an02062j.

(110) Hankin, J. A.; Murphy, R. C.; Barkley, R. M.; Gijón, M. A. Ion Mobility and Tandem Mass Spectrometry of Phosphatidylglycerol and Bis(Monoacylglycerol) Phosphate (BMP). *Int. J. Mass Spectrom.* **2015**, *378*, 255–263. https://doi.org/10.1016/j.ijms.2014.08.026.

(111) Fouque, K. J. D.; Ramirez, C. E.; Lewis, R. L.; Koelmel, J. P.; Garrett, T. J.; Yost, R. A.; Fernandez-Lima, F. Effective Liquid Chromatography-Trapped Ion Mobility Spectrometry-Mass Spectrometry Separation of Isomeric Lipid Species. *Anal. Chem.* **2019**, *91* (8), 5021–5027. https://doi.org/10.1021/acs.analchem.8b04979.

(112) Anderson, D. M. G.; Ablonczy, Z.; Koutalos, Y.; Hanneken, A. M.; Spraggins, J. M.; Calcutt, M. W.; Crouch, R. K.; Caprioli, R. M.; Schey, K. L. Bis(Monoacylglycero)Phosphate Lipids in the Retinal Pigment Epithelium Implicate Lysosomal/Endosomal Dysfunction in a Model of Stargardt Disease and Human Retinas. *Sci. Rep.* **2017**, *7* (1), 17352. https://doi.org/10.1038/s41598-017-17402-1.

(113) Akgoc, Z.; Sena-Esteves, M.; Martin, D. R.; Han, X.; D'Azzo, A.; Seyfried, T. N. Bis(Monoacylglycero)Phosphate: A Secondary Storage Lipid in the Gangliosidoses. *J. Lipid Res.* **2015**, *56* (5), 1006–1013. https://doi.org/10.1194/jlr.M057851.

(114) Numata, M.; Chu, H. W.; Dakhama, A.; Voelker, D. R. Pulmonary Surfactant Phosphatidylglycerol Inhibits Respiratory Syncytial Virus-Induced Inflammation and Infection. *Proc. Nat. Acad. Sci.* **2010**, *107* (1), 320–325. https://doi.org/10.1073/pnas.0909361107.

(115) Janmey, P. A.; Kinnunen, P. K. J. Biophysical Properties of Lipids and Dynamic Membranes. *Trends Cell. Biol.* **2006**, *16* (10), 538–546. https://doi.org/10.1016/j.tcb.2006.08.009.

(116) Groessl, M.; Graf, S.; Knochenmuss, R. High Resolution Ion Mobility-Mass Spectrometry for Separation and Identification of Isomeric Lipids. *Analyst.* **2015**, *140* (20), 6904–6911. https://doi.org/10.1039/C5AN00838G.

(117) Lewis, B. A.; Engelman, D. M. Lipid Bilayer Thickness Varies Linearly with Acyl Chain Length in Fluid

Phosphatidylcholine Vesicles. *J. Mol. Biol.* **1983**, *166* (2), 211–217. https://doi.org/10.1016/S0022-2836(83)80007-2.

(118) Brown, S. H. J.; Mitchell, T. W.; Oakley, A. J.; Pham, H. T.; Blanksby, S. J. Time to Face the Fats: What Can Mass Spectrometry Reveal about the Structure of Lipids and Their Interactions with Proteins? Lipid-Protein Interactions. *J. Am. Soc. Mass Spectrom.* **2012**, *23*, 1441–1449. https://doi.org/10.1007/s13361-012-0410-2.

(119) Fahy, E.; Sud, M.; Cotter, D.; Subramaniam, S. LIPID MAPS Online Tools for Lipid Research. *Nucleic Acids Res.* **2007**, *35*. https://doi.org/10.1093/nar/gkm324.

(120) Sonnino, S.; Mauri, L.; Chigorno, V.; Prinetti, A. Gangliosides as Components of Lipid Membrane Domains. *Glycobiology* **2007**, *17* (1), 1R-13R. https://doi.org/10.1093/GLYCOB/CWL052.

(121) Lunghi, G.; Fazzari, M.; Biase, E. Di; Mauri, L.; Chiricozzi, E.; Sonnino, S. The Structure of Gangliosides Hides a Code for Determining Neuronal Functions. *FEBS Open Biol.* **2021**. https://doi.org/10.1002/2211-5463.13197.

(122) Benady, A.; Freidin, D.; Pick, C. G.; Rubovitch, V. GM1 Ganglioside Prevents Axonal Regeneration Inhibition and Cognitive Deficits in a Mouse Model of Traumatic Brain Injury. *Sci. Rep.* **2018**, *8* (1), 1–10. https://doi.org/10.1038/s41598-018-31623-y.

(123) Kaida, K.; Ariga, T.; Yu, R. K. Antiganglioside Antibodies and Their Pathophysiological Effects on Guillain–Barré Syndrome and Related Disorders—A Review. *Glycobiology* **2009**, *19* (7), 676–692. https://doi.org/10.1093/GLYCOB/CWP027.

(124) Kaida, K.; Kusunoki, S. Antibodies to Gangliosides and Ganglioside Complexes in Guillain–Barré Syndrome and Fisher Syndrome: Mini-Review. *J. Neuroimmunol.* **2010**, *223* (1–2), 5–12. https://doi.org/10.1016/J.JNEUROIM.2010.02.001.

(125) Yuki, N.; Suzuki, K. Review Guillain-Barré Syndrome and Anti-Ganglioside Antibodies: A Clinician-Scientist's Journey. *Proc. Jpn. Acad., Ser B Phys . Biol. Sci.* **2012**, *88* (7), 299–326. https://doi.org/10.2183/pjab.88.299.

(126) Ariga, T.; McDonald, M. P.; Yu, R. K. Thematic Review Series: Sphingolipids. Role of Ganglioside Metabolism in the Pathogenesis of Alzheimer's Disease—a Review. *J. Lipid Res.* **2008**, *49* (6), 1157–1175. https://doi.org/10.1194/JLR.R800007-JLR200.

(127) M, A.; D, G.; J, F.; LC, M.; SW, L.; P, K.; A, D. P.; A, H.; BJ, K.; KG, T.; GB, B.; K, F.; S, S. Disease-Modifying Effects of Ganglioside GM1 in Huntington's Disease Models. *EMBO Mol. Med.* **2017**, *9* (11), 1537–1557. https://doi.org/10.15252/EMMM.201707763.

(128) Metelmann, W.; Vukelić, Ž.; Peter-Katalinić, J. Nano-Electrospray Ionization Time-of-Flight Mass Spectrometry of Gangliosides from Human Brain Tissue. *J. Mass Spectrom.* **2001**, *36* (1), 21–29. https://doi.org/10.1002/JMS.100.

(129) Kotani, M.; Kawashima, D.; Ozawa, H.; Terashima, T.; Tai, T. *Differential Distribution of Major Gangliosides in Rat Central Nervous System Detected by Specific Monoclonal Antibodies*; 1993; Vol. 3.

(130) K, V.; B, V.; IV, D.; RL, S.; M, H. Differential Distribution of Major Brain Gangliosides in the Adult Mouse Central Nervous System. *PLoS ONEne* **2013**, *8* (9). https://doi.org/10.1371/JOURNAL.PONE.0075720.

(131) Hájek, R.; Jirásko, R.; Lísa, M.; Cífková, E.; Holčapek, M. Hydrophilic Interaction Liquid Chromatography-Mass Spectrometry Characterization of Gangliosides in Biological Samples. *Anal. Chem.* **2017**, *89* (22), 12425–12432. https://doi.org/10.1021/acs.analchem.7b03523.

(132) Hájek, R.; Lísa, M.; Khalikova, M.; Jirásko, R.; Cífková, E.; Študent, V.; Vrána, D.; Opálka, L.; Vávrová, K.; Matzenauer, M.; Melichar, B.; Holčapek, M. HILIC/ESI-MS Determination of Gangliosides and Other Polar Lipid Classes in Renal Cell Carcinoma and Surrounding Normal Tissues. https://doi.org/10.1007/s00216-018-1263-8.

(133) Ito, E.; Tominaga, A.; Waki, H.; Miseki, K.; Tomioka, A.; Nakajima, K.; Kakehi, K.; Suzuki, M.; Taniguchi, N.; Suzuki, A. Structural Characterization of Monosialo-, Disialo- and Trisialo-Gangliosides by Negative Ion AP-MALDI-QIT-TOF Mass Spectrometry with MSn Switching. *Neurochem. Res.* **2012**, *37* (6), 1315–1324. https://doi.org/10.1007/S11064-012-0735-Z.

(134) Weishaupt, N.; Caughlin, S.; Yeung, K. K.-C.; Whitehead, S. N.; Mikula, S.; Elston, G.; Biswavas Misra, B.; Whitehead, S. N.; Weishaupt, N.; Caughlin, S.; K-C Yeung, K. Differential Anatomical Expression of Ganglioside GM1 Species Containing D18:1 or D20:1 Sphingosine Detected by MALDI Imaging Mass Spectrometry in Mature Rat Brain. *Front. Neuroanat.* **2015**, *9*, 155.

(135) Tobias, F.; Pathmasiri, K. C.; Cologna, S. M. Mass Spectrometry Imaging Reveals Ganglioside and Ceramide Localization Patterns during Cerebellar Degeneration in the Npc1−/− Mouse Model. *Anal. Bioanal. Chem.* **2019**, *411* (22), 5659–5668. https://doi.org/10.1007/S00216-019-01989-7.

(136) O'connor, P. B.; Mirgorodskaya, E.; Costello, C. E. High Pressure Matrix-Assisted Laser

Desorption/Ionization Fourier Transform Mass Spectrometry for Minimization of Ganglioside Fragmentation. *J. Am. Soc. Mass Spectrom.* **2002**, *13* (4), 402–407.
(137) Yang, E.; Dufresne, M.; Chaurand, P. Enhancing Ganglioside Species Detection for MALDI-TOF Imaging Mass Spectrometry in Negative Reflectron Mode. *Int. J. Mass Spectrom.* **2019**, *437*, 3–9. https://doi.org/10.1016/j.ijms.2017.09.011.
(138) N. Jackson, S.; Benoit Colsch; Thomas Egan; K. Lewis, E.; Albert Schultz, J.; S. Woods, A. Gangliosides' Analysis by MALDI-Ion Mobility MS. *Analyst* **2011**, *136* (3), 463–466. https://doi.org/10.1039/C0AN00732C.
(139) Yang, J.; Norris, J. L.; Caprioli, R. Novel Vacuum Stable Ketone-Based Matrices for High Spatial Resolution MALDI Imaging Mass Spectrometry. *J. Mass Spectrom.* **2018**, *0* (0), 1005–1012. https://doi.org/doi:10.1002/jms.4277.
(140) Dufresne, M.; Patterson, N. H.; Norris, J. L.; Caprioli, R. M. Combining Salt Doping and Matrix Sublimation for High Spatial Resolution MALDI Imaging Mass Spectrometry of Neutral Lipids. *Anal. Chem.* **2019**, *91* (20), 12928–12934.
(141) Palmer-Toy, D. E.; Sarracino, D. A.; Sgroi, D.; Levangie, R.; Leopold, P. E.; Xu, B. J.; Caprioli, R. M.; Sanders, M. E.; Jensen, R. A.; Bhattacharya, S. H.; Gal, A. A.; Murray, K. K. Integrating Histology and Imaging Mass Spectrometry. *J. Am. Soc. Mass Spectrom* **2003**, *3* (10), 1145. https://doi.org/10.1021/ac0351264.
(142) Lein, E. S.; Hawrylycz, M. J.; Ao, N.; Ayres, M.; Bensinger, A.; Bernard, A.; Boe, A. F.; Boguski, M. S.; Brockway, K. S.; Byrnes, E. J.; Chen, L.; Chen, L.; Chen, T.-M.; Chi Chin, M.; Chong, J.; Crook, B. E.; Czaplinska, A.; Dang, C. N.; Datta, S.; Dee, N. R.; Desaki, A. L.; Desta, T.; Diep, E.; Dolbeare, T. A.; Donelan, M. J.; Dong, H.-W.; Dougherty, J. G.; Duncan, B. J.; Ebbert, A. J.; Eichele, G.; Estin, L. K.; Faber, C.; Facer, B. A.; Fields, R.; Fischer, S. R.; Fliss, T. P.; Frensley, C.; Gates, S. N.; Glattfelder, K. J.; Halverson, K. R.; Hart, M. R.; Hohmann, J. G.; Howell, M. P.; Jeung, D. P.; Johnson, R. A.; Karr, P. T.; Kawal, R.; Kidney, J. M.; Knapik, R. H.; Kuan, C. L.; Lake, J. H.; Laramee, A. R.; Larsen, K. D.; Lau, C.; Lemon, T. A.; Liang, A. J.; Liu, Y.; Luong, L. T.; Michaels, J.; Morgan, J. J.; Morgan, R. J.; Mortrud, M. T.; Mosqueda, N. F.; Ng, L. L.; Ng, R.; Orta, G. J.; Overly, C. C.; Pak, T. H.; Parry, S. E.; Pathak, S. D.; Pearson, O. C.; Puchalski, R. B.; Riley, Z. L.; Rockett, H. R.; Rowland, S. A.; Royall, J. J.; Ruiz, M. J.; Sarno, N. R.; Schaffnit, K.; Shapovalova, N. V.; Sivisay, T.; Slaughterbeck, C. R.; Smith, S. C.; Smith, K. A.; Smith, B. I.; Sodt, A. J.; Stewart, N. N.; Stumpf, K.-R.; Sunkin, S. M.; Sutram, M.; Tam, A.; Teemer, C. D.; Thaller, C.; Thompson, C. L.; Varnam, L. R.; Visel, A.; Whitlock, R. M.; Wohnoutka, P. E.; Wolkey, C. K.; Wong, V. Y.; Wood, M.; Yaylaoglu, M. B.; Young, R. C.; Youngstrom, B. L.; Feng Yuan, X.; Zhang, B.; Zwingman, T. A.; Jones, A. R. Genome-Wide Atlas of Gene Expression in the Adult Mouse Brain. *Nature* **2006**, *445* (7124), 168–176. https://doi.org/10.1038/nature05453.
(143) Ng, L.; Bernard, A.; Lau, C.; Overly, C. C.; Dong, H.-W.; Kuan, C.; Pathak, S.; Sunkin, S. M.; Dang, C.; Bohland, J. W.; Bokil, H.; Mitra, P. P.; Puelles, L.; Hohmann, J.; Anderson, D. J.; Lein, E. S.; Jones, A. R.; Hawrylycz, M. An Anatomic Gene Expression Atlas of the Adult Mouse Brain. *Nat. Neurosci.* **2009**, *12* (3), 356–362. https://doi.org/10.1038/nn.2281.
(144) Spraggins, J. M.; Rizzo, D. G.; Moore, J. L.; Rose, K. L.; Hammer, N. D.; Skaar, E. P.; Caprioli, R. M. MALDI FTICR IMS of Intact Proteins: Using Mass Accuracy to Link Protein Images with Proteomics Data. *J. Am. Soc. Mass Spectrom* **2015**, *26* (6), 947–985. https://doi.org/10.1007/s13361-015-1147-5.
(145) Watson, C.; Paxinos, G.; Kayalioglu, G.; Heise, C. Chapter 15 - Atlas of the Rat Spinal Cord. In *The Spinal Cord*; Academic Press, 2008; pp 238–306. https://doi.org/10.1016/B978-0-12-374247-6.50019-5.
(146) JFOSTER, T. Staphylococcus Aureus. *Mol. Med. Microbiol.* **2002**, 839–888. https://doi.org/10.1016/B978-012677530-3/50258-0.
(147) Bergdoll, M. S. Staphylococcus Aureus. *J. AOAC Int.* **1991**, *74* (4), 706–710. https://doi.org/10.1093/JAOAC/74.4.706.
(148) Serezani, C. H.; Brandt, S. L.; Putnam, N. E.; Cassat, J. E. Invasive Infections Evolving Paradigms in Soft Tissue and : Staphylococcus Aureus Innate Immunity To. *J Immunol Ref.* **2022**, *200*, 3871–3880. https://doi.org/10.4049/jimmunol.1701574.
(149) Kobayashi, S. D.; Malachowa, N.; Deleo, F. R. Pathogenesis of Staphylococcus Aureus Abscesses. *Am. J. Pathol.* **2015**, *185* (6), 1518–1527. https://doi.org/10.1016/J.AJPATH.2014.11.030.
(150) Nakayama, H.; Nagafuku, M.; Suzuki, A.; Iwabuchi, K.; Inokuchi, J.-I.; Inokuchi, J. I. The Regulatory Roles of Glycosphingolipid-Enriched Lipid Rafts in Immune Systems. *FEBS Lett.* **2018**, *592*, 3921–3942. https://doi.org/10.1002/1873-3468.13275.
(151) Lopez, P. H.; Schnaar, R. L. Gangliosides in Cell Recognition and Membrane Protein Regulation. *Curr. Opin.*

Struct. Biol. **2009**, *19* (5), 549–557. https://doi.org/10.1016/J.SBI.2009.06.001.
(152) Inokuchi, J. I.; Nagafuku, M.; Ohno, I.; Suzuki, A. Heterogeneity of Gangliosides among T Cell Subsets. *Cell. Mol. Life Sci.* **2013**, *70* (17), 3067–3075. https://doi.org/10.1007/S00018-012-1208-X.
(153) Ghosh, S. Sialic Acid and Biology of Life: An Introduction. *Sialic Acids Sialoglycoconjugates Biol. Life, Heal. Dis.* **2020**, 1. https://doi.org/10.1016/B978-0-12-816126-5.00001-9.
(154) Varki, N. M.; Varki, A. Diversity in Cell Surface Sialic Acid Presentations: Implications for Biology and Disease. *Pathobiol. Focus*. https://doi.org/10.1038/labinvest.3700656.
(155) Parente de Carvalho, T.; Eckstein, C.; Layara de Moura, L.; Von Ruckert Heleno, N.; Alves da Silva, L.; Oliveira dos Santos, D.; dos Reis de Souza, L.; Rodrigues Oliveira, A.; Gariglio Clark Xavier, R.; Thompson, M.; Otavio Silveira Silva, R.; Lima Santos, R. Staphylococcus Aureus-Induced Pyogranulomatous Dermatitis, Osteomyelitis, and Meningitis with Splendore-Hoeppli Reaction in a Cat Coinfected with the Feline Leukemia Virus and Leishmania Sp. *Braz J Vet Pathol 2022* (1), 31–37. https://doi.org/10.24070/bjvp.1983-0246.v15i1p31-37.
(156) Hussein, M. R. Mucocutaneous Splendore-Hoeppli Phenomenon. *J. Cutan. Pathol.* **2008**, *35* (11), 979–988. https://doi.org/10.1111/J.1600-0560.2008.01045.X.
(157) Martínez-Girón, R.; Pantanowitz, L. "Splendore-Hoeppli" Phenomenon. *Diagn. Cytopathol.* **2020**, *48* (12), 1316–1317. https://doi.org/10.1002/DC.24512.
(158) Yohe, H. C.; Macala, L. J.; Giordano, G.; McMurray, W. J. GM1b and GM1b-GalNAc: Major Gangliosides of Murine-Derived Macrophage-like WEHI-3 Cells. *Biochim. Biophys. Acta - Biomembr.* **1992**, *1109* (2), 210–217. https://doi.org/10.1016/0005-2736(92)90085-Z.
(159) Ryan, J. L.; Yohe, H. C.; Cuny, C. L.; Macala, L. J.; Saito, M.; Mcmurray, W. J. The Presence of Sialidase-Sensitive Sialosylgangliotetraosyl Ceramide (GM1b) in Stimulated Murine Macrophages. Deficiency of GM1b in Escherichia Coli-Activated Macrophages from the C3H/HeJ Mouse. *J. Immunol.* **1991**, *146* (6), 1900–1908.
(160) Savas, B.; Astarita, G.; Aureli, M.; Sahali, D.; Ollero, M. Gangliosides in Podocyte Biology and Disease. *Int. J. Mol. Sci.* **2020**, *21* (24), 1–17. https://doi.org/10.3390/IJMS21249645.
(161) Kurir, T. T.; Vukovic, I.; Bozic, J.; Markotic, A.; Ljubicic, S. The Missing Link-Likely Pathogenetic Role of GM3 and Other Gangliosides in the Development of Diabetic Nephropathy. *Kidney Blood Press Res* **2015**, *40*, 306–314. https://doi.org/10.1159/000368506.
(162) Corbin, B. D.; Seeley, E. H.; Raab, A.; Feldmann, J.; Miller, M. R.; Torres, V. J.; Anderson, K. L.; Dattilo, B. M.; Dunman, P. M.; Gerads, R.; Caprioli, R. M.; Nacken, W.; Chazin, W. J.; Skaar, E. P. Metal Chelation and Inhibition of Bacterial Growth in Tissue Abscesses. *Science (80-.).* **2008**, *319* (5865), 962–965. https://doi.org/10.1126/SCIENCE.1152449/SUPPL_FILE/CORBIN.SOM.PDF.
(163) Seeley, E. H.; Caprioli, R. M. 3D Imaging by Mass Spectrometry: A New Frontier Imaging. *Anal. Chem.* **2012**, *84* (5), 2105–2110. https://doi.org/10.1021/ac2032707.
(164) Tan, W. C. C.; Nerurkar, S. N.; Cai, H. Y.; Ng, H. H. M.; Wu, D.; Wee, Y. T. F.; Lim, J. C. T.; Yeong, J.; Lim, T. K. H. Overview of Multiplex Immunohistochemistry/Immunofluorescence Techniques in the Era of Cancer Immunotherapy. *Cancer Commun.* **2020**, *40* (4), 135. https://doi.org/10.1002/CAC2.12023.
(165) Imberty, A.; Varrot, A. Microbial Recognition of Human Cell Surface Glycoconjugates. *Curr. Opin. Struct. Biol.* **2008**, *18* (5), 567–576. https://doi.org/10.1016/J.SBI.2008.08.001.
(166) Ladisch, S.; Becker, H.; Ulsh, L. Immunosuppression by Human Gangliosides: I. Relationship of Carbohydrate Structure to the Inhibition of T Cell Responses. *Biochim. Biophys. Acta - Lipids Lipid Metab.* **1992**, *1125* (2), 180–188. https://doi.org/10.1016/0005-2760(92)90043-U.
(167) Hsu, F.-F.; Turk, J. Electrospray Ionization with Low-Energy Collisionally Activated Dissociation Tandem Mass Spectrometry of Glycerophospholipids: Mechanisms of Fragmentation and Structural Characterization. *J. Chromatogr. B* **2009**, *877* (26), 2673–2695. https://doi.org/10.1016/J.JCHROMB.2009.02.033.